Combination of Searches for gauge-mediated Supersymmetry in Events with Photons at CMS

Master Thesis

von

Danilo Meuser

vorgelegt der

Fakultät für Mathematik, Informatik und Naturwissenschaften der RWTH Aachen

im Oktober 2018

erstellt im

I. Physikalischen Institut B

bei

Prüfer: Prof. Dr. Lutz Feld

Zweitprüfer: Prof. Dr. Thomas Hebbeker

Abstract

In this thesis, a combination of searches for gauge-mediated supersymmetry in events with at least one photon is presented. The combination is based on proton-proton collision data recorded by CMS in 2016, which corresponds to a center-of-mass energy of 13 TeV and an integrated luminosity of 35.9 fb^{-1}. Four individual analyses, which all focus on signatures with isolated photons and a significant amount of missing transverse momentum, are combined to cover a wide range of different signal scenarios. These signatures are complemented by additional charged leptons, a second photon, or additional requirements on the hadronic activity. Within the combination, the signal regions of the contributing analyses are studied concerning possible overlaps, which are removed by an optimized veto strategy. The combination of searches probes the phase space of two general gauge-mediated scenarios. For these scenarios, the combination sets the first observed lower limits on neutralino and chargino masses, which reach up to 475 GeV and 850 GeV, respectively. In addition, the results of the combination are interpreted with respect to strong gluino pair production and with respect to electroweak scenarios, which feature a variable gaugino decay. Within these scenarios, gluino masses up to 2100 GeV and neutralino masses up to 1200 GeV can be excluded.

Contents

1 Introduction

For ages, humans have been trying to understand the principles and constitution of the matter surrounding us. Starting with the ancient Greeks, who described the matter as the composition of atoms, named by the old Greek word for indivisibility *átomos*. Followed by scientists like J.J. Thompson, who discovered the electron in 1897 [1], or Ernest Rutherford, who showed in 1911 that atoms contain a small and dense nucleus [2]. This research was brought to a new level by the use of particle colliders beginning in the middle of the last century [3].
With the use of this new kind of experiments, multiple new particles including their properties and interactions have been observed and studied at particle colliders like the Large Electron-Positron Collider (LEP) [4] or the Tevatron [5]. So far, all observations and measurements made in this field of research, namely the elementary particle physics, can be explained by the standard model of particle physics (SM) leading to confidence in the validity of this theory. Nevertheless, there are indications that the SM is not complete and has to be extended by theories, which describe physics beyond the standard model. Shortcomings of the SM are for example based on the origin of dark matter [6], the unification of the fundamental forces, or the scale of the Higgs mass [7]. One possible extension of the SM, which accounts for these shortcomings, is the theory of supersymmetry (SUSY) [7]. Here, a new symmetry between fermions and bosons is introduced resulting in an extended particle content, which can be described by the minimal supersymmetric standard model (MSSM). With this extended particle content, several shortcomings of the SM can be solved while maintaining the successful predictions made by the SM itself.
Finding evidence for physics beyond the standard model, such as SUSY, is one of the primary goals of the currently largest and most powerful particle collider, the Large Hadron Collider (LHC) [8], which is operated by the European Organization of Nuclear Research (CERN) near Geneva. Among other detectors, two multi-purpose detectors, namely ATLAS (A Toroidal LHC Apparatus) [9] and CMS (Compact Muon Solenoid) [10], are used to study proton-proton collisions, which feature a center-of-mass energy of currently 13 TeV.

In this thesis, a combination of four individual searches for gauge-mediated supersymmetry in events with photons is performed. All four contributing searches are based on the data recorded by CMS in 2016, which corresponds to proton-proton collisions at a center-of-mass energy of 13 TeV and an integrated luminosity of 35.9 fb^{-1} [11]. The searches in events with photons are motivated by the gauge-mediated SUSY scenarios considered in the individual analyses. In those scenarios, the next-to-lightest supersymmetric particle (NLSP) is given by the lightest neutralino $\widetilde{\chi}_1^0$. Depending on the composition of the NLSP its decay to the lightest supersymmetric particle (LSP), given by the gravitino $\widetilde{\mathrm{G}}$, and a photon γ can be enhanced. This decay results in events with at least one photon and a large amount of missing transverse momentum $p_{\mathrm{T}}^{\mathrm{miss}}$ caused by the undetected gravitino.
Each of the four searches used in the combination is based on this kind of signature, but they differ with respect to additional requirements. Two of the four analyses, namely Photon+S_{T}^{γ} [12] and Photon+H_{T}^{γ} [13], cover a wider phase space since their event selection does not include any requirements on further reconstructed particles. While the Photon+H_{T}^{γ} search uses an additional requirement on the hadronic activity of an event to gain sensitivity for strongly produced SUSY, the Photon+S_{T}^{γ} event selection avoids such a requirement to focus on electroweak scenarios. The event selections of the two remaining searches, in contrast, feature additional particles. In the case of the Photon+Lepton [14] search, a charged lepton, given by an electron or muon, is required in addition to the photon, while the event selection of the Diphoton analysis [15] requires at least two photons.

Mainly two different aspects motivate the combination of these four searches. On the one hand, a combination would lead to a consistent picture of searches for SUSY in events with photons performed on the CMS data set recorded in 2016 at 13 TeV. On the other hand, a statistical combination should increase the sensitivity to several SUSY scenarios and can be used to set the first exclusion limits on two new gauge-mediated SUSY scenarios, which include a wide range of possible final states.

This thesis is structured as follows. The standard model of particle physics as well as the theory of supersymmetry including the framework and signal scenarios used for the interpretation of the combination, are introduced in Sec. 2. In Sec. 3 the procedure of limit setting, which is widely used not only in the final interpretation but also for the development of a robust combination strategy, is illustrated. The experiment itself, namely LHC and CMS, and the different data sets including SM background simulations and object definitions are covered by Sec. 4 and 5, respectively. The combination is interpreted in two different types of signal scenarios, which are discussed in detail in Sec. 6. For the first type different simplified models, which were already used in the individual analyses, are merged to achieve variable gaugino decay branching fractions. The second type corresponds to two new general-gauge mediated models, which are especially produced for the combination. For these models, a detailed discussion on the mass spectra and sparticle decays as well as on the performed cross section calculation is given. In Sec. 7 the event selections and the background estimation methods used by the four individual analyses are briefly discussed. This discussion is followed by a study of phase space overlaps between the signal regions of the contributing searches in Sec. 8. Within this study possible overlaps, which would not allow for a statistical combination, are removed, and a robust combination strategy is developed by adding additional vetoes to the individual event selections. To ensure a reliable background prediction for searches, which are affected by the additional vetoes, further validations of the background prediction methods are performed. In a last step towards the final combination, uncertainty correlations between the individual searches are studied in Sec. 9. The results of the combination are presented in Sec. 10. An overview of the agreement between background prediction and observed data is given for each search bin used in the combination. Furthermore, the results are interpreted with respect to different scenarios and the resulting exclusion contours are discussed in detail. Finally, the thesis is concluded by a summary and a brief outlook in Sec. 11.

2 Theory

The main theory used to describe the different aspects of high energy physics is the standard model of particle physics (SM). This model classifies all known elementary particles and describes their interactions with each other. It has been tested for example at particle colliders such as the Large Electron-Positron Collider (LEP) [4] and the Tevatron [5]. Its predictive power was just recently again confirmed by the discovery of the Higgs boson in July 2012 by CMS [16] and ATLAS [17] at the LHC.
One possible extension to this model, which is needed due to several shortcomings, is the theory of supersymmetry (SUSY). This extension can solve multiple problems, which are based on experimental results as well as theoretical aspects that cannot be explained by the SM. Finding evidence for this new theory is the main motivation of the different contributing analyses.
The following sections aim to give an introduction into the theoretical aspects relevant to the combination. The commonly used unit system and notations will shortly be explained, as well as the central features of the SM and its shortcomings. The primary goal, however, is to introduce the concept of SUSY including a possible SUSY breaking scenario and the framework applied to interpret the results of the combination.

2.1 Units and Notations

The commonly used unit system in particle physics is the natural unit system, where the speed of light c as well as the reduced Planck constant $\hbar$ are set to unity:

$$\hbar = c = 1 \ . \tag{2.1}$$

With this choice natural units simplify the central quantities of particle physics. The mass, the momentum, and the energy are given in the same unit, usually stated in GeV.
For convenience, the natural units are not used for time and length, which are still given in SI units. In addition, cross sections and the integrated luminosity are expressed in powers of barn ($1 \text{ b} = 10^{-28} \text{ m}^2$).

2.2 Standard Model of Particle Physics

The standard model of particle physics (SM) [18–22] is the main theoretical framework describing the properties and interactions of all known elementary particles. In this model, the fundamental forces responsible for the interactions between particles are based on a renormalizable quantum field theory. They result from the local gauge invariance under the combined symmetry group of the SM:

$$SU(3) \text{ x } SU(2) \text{ x } U(1) \ . \tag{2.2}$$

The strong force is based on the $SU(3)$ group, while the electromagnetic and the weak force are unified under $SU(2)$ x $U(1)$. Thus, the SM can describe three of the four known fundamental forces of nature but does not account for gravitation.

2.2.1 Particle Content and Fundamental Forces

The elementary particles of the SM are classified by their spin into two groups, the fermions and the bosons (cf. Fig. 2.1). Fermions have a half-integer spin and consist of a total of twelve[1] particle and their corresponding antiparticle types. These antiparticles differ only by the sign of the additive quantum numbers from the associated particle. Unless otherwise stated, no distinction between particle and antiparticle is made in the following. The fermions are further divided into leptons and quarks.
Leptons interact via the weak force and, if they are electrically charged, also via the electromagnetic force. In this group, each of the charged leptons (electron e, muon μ, and tau τ) can be connected to a corresponding uncharged lepton (electron neutrino ν_{e}, muon neutrino ν_μ and tau neutrino ν_τ), which together form a generation resulting in a total of three lepton generations. Quarks, in contrast, also interact via the strong force and therefore couple to all three fundamental forces described by the SM. They can be further divided into up-type quarks with an electrical charge of $Q = +2/3$ and down-type quarks with $Q = -1/3$. Here, each of the three quark generations includes an up-type and a down-type quark.

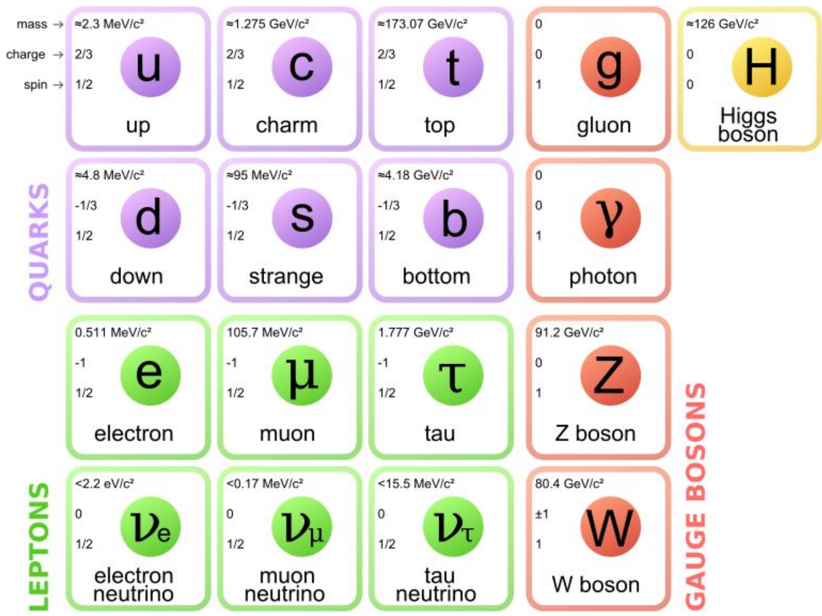

Figure 2.1: Elementary particles of the SM [23] grouped into quarks (purple) and leptons (green), which build the group of fermions. The bosons include the gauge bosons (red) and the Higgs boson (yellow). The charge and the spin of each particle are given in units of the elementary charge e and the reduced Planck constant $\hbar$, respectively.

The second group of the elementary particles is given by bosons, which have integer spin. They consist of the gauge bosons mediating the forces described in the SM and the Higgs boson, which introduces mass to charged fermions and massive gauge bosons via the Higgs mechanism [24]. This mechanism as well as the three fundamental forces will be briefly introduced in the next paragraphs.

The SM simultaneously describes the electromagnetic force and the weak force based on the $SU(2)$ x $U(1)$ gauge group. The electroweak force is mediated by the four eigenstates of this

[1] Neglecting different chirality states.

gauge group (W^1, W^2, W^3, and B). Due to electroweak symmetry breaking the gauge eigenstates mix to the four gauge bosons ($W^{\pm}$, Z^0, and γ), which have been experimentally observed [25–29]. The only massless particle of these electroweak gauge bosons after the symmetry breaking is the photon γ, which couples to the electric charge and therefore mediates the electromagnetic force. The weak force, in contrast, is mediated by the remaining three massive gauge bosons $W^{\pm}$ and Z^0, which couple to the weak isospin I_3, also called flavor. While the photon does not distinguish between different chirality states, which in case of massless particles correspond to the projection of the spin along the linear momentum of the particle, the massive gauge bosons do. This so-called parity violation is maximal for interactions mediated by $W^{\pm}$, which does not couple to right-handed fermions, and is also found in interactions mediated by Z^0, which couples to right- and left-handed fermions with a different strength.
In order to preserve local gauge invariance, which was otherwise violated by $W^{\pm}$ and Z^0 not being massless, the Higgs mechanism [24] was introduced as the latest addition to the SM. The mechanism is based on the non-zero vacuum expectation value of the Higgs potential leading to a spontaneous symmetry breaking. As a consequence of this, $W^{\pm}$ and Z^0 are massive while local gauge invariance is still preserved. Furthermore, this mechanism results in the prediction of an additional neutral particle, the Higgs boson. A particle with properties consistent with the SM Higgs boson was observed in 2012 verifying the latest part of the SM [16, 17].

In the SM, quantum chromodynamics (QCD) is used to describe the interactions between quarks caused by the strong force. This non-abelian gauge theory is based on the $SU(3)$ gauge group, which has eight eigenstates associated with eight gluons completing the group of gauge bosons (cf. Fig. 2.1). Gluons mediate the strong force by coupling to color charge carried by all quarks and the gluons themselves. Therefore, there are not only interactions between gluons and quarks, but also between two or more gluons (gluon self-coupling). In contrast to the electroweak force, where charged particles can be observed, only color neutral combinations of quarks, but no free quarks or gluons have been detected so far. These combinations can be classified into combinations of a quark and an anti-quark (mesons) and of three (anti-)quarks (baryons), which together form the group of hadrons[2]. The reason for this behavior is the effect of color confinement [31]. This effect is based on the linearly increasing potential energy with increasing distance between two quarks leading to the creation of new quark pairs in between. Since the quark pairs immediately form color neutral combinations, separated quarks can cause hadronic showers, also called jets.

2.2.2 Shortcomings of the Standard Model

So far the SM has been confirmed by multiple experimental tests and precision measurements. It was able to predict several particles over the last decades like for example the Higgs boson or the top quark observed by Tevatron in 1995 [32, 33]. Nevertheless, there are experimental observations as well as problems in the model itself, which call for extensions of the SM, often referred to as physics beyond the standard model. Some of the main shortcomings motivating one possible extension, namely supersymmetry, will be shortly discussed in the following.

Unification of Forces

Based on the unification of the electromagnetic and weak force it seems likely that all forces described in the SM can be unified at a higher energy scale. This would allow for a consis-

[2] Just recently additional combinations of four quarks and one anti-quark, called pentaquark, have been observed [30]

tent theory of the electroweak and strong force at high energy scales, also called grand unified theory (GUT), using only one common symmetry. For this, the coupling constants associated with the three forces would need to be energy dependent, which is the case and enables the electroweak unification as a consequence of electroweak symmetry breaking [34]. In addition, a common intersection point of all three coupling constants is required for the unification of the three forces. By extrapolating the coupling constants to higher energies, this common intersection point cannot be predicted by the SM. Therefore, a unification of all three forces is not possible in the SM.

Hierarchy Problem

A fundamental problem in the SM is based on quantum corrections to the Higgs mass caused by the coupling of massive particles to the Higgs field [7]. In case of the scalar Higgs boson, these loop corrections depend in first-order quadratically on the energy cutoff scale Λ_{UV}:

$$\Delta m_H^2 = -\frac{|\lambda_f^2|}{8\pi^2}\Lambda_{\mathrm{UV}}^2 + ... \tag{2.3}$$

Each massive fermion can play the role of f leading to the largest corrections in case of the top quark. If the SM was valid up to for example the reduced Planck scale $M_{\mathrm{P}} \approx 10^{18}$ GeV, the cutoff scale needed to be of the same order resulting in corrections to the Higgs mass, which are around 30 orders of magnitude larger than the measured value. Since these corrections would have to cancel each other almost exactly, this would result in fine-tuning of the Higgs mass, often referred to as the hierarchy problem.

Dark Matter Problem

Multiple astrophysical experiments found evidence for the existence of non-baryonic matter, which accounts for up to one quarter of the energy density of the universe. The strongest of these evidence is given by the difference in the rotational speed of galaxies between its measured value and the calculated result based on the visible mass of the galaxies [6]. Since non-baryonic matter does not interact via the electromagnetic force, neutrinos are the only stable particles in the SM which could contribute to the hot (relativistic) dark matter. Taking into account that only a small part of the dark matter can be relativistic [34] and that the neutrino masses are small, neutrinos cannot account for the complete amount of dark matter present in the universe. Therefore, there is no particle in the SM, which could serve as an adequate dark matter candidate.

2.3 Supersymmetry

One possible extension to the SM is the theory of supersymmetry (SUSY) [7]. This theory can account for several of the shortcomings, introduced before, by extending the SM particle content. Each elementary particle in the SM is assigned an additional supersymmetric partner (sparticle) together forming a supermultiplet. The superpartners inside these multiplets have the same quantum numbers with exception of the spin, which differs by half a unit between the superpartners. Thus, the superpartners of fermions are bosonic (integer spin) and vice versa. To adapt this symmetry in the naming scheme the superpartners of fermions are named with a prepending "s" (e.g., smuon) while the superpartners of the bosons have an appending "ino" (e.g., wino).

This extension to the SM is accompanied by changes in the Higgs sector as well as additions covering gravitation to form the minimal supersymmetric standard model (MSSM). In contrast to the SM, the Higgs sector in the MSSM is described by two doublets (cf. Fig. 2.2). Here, the down-type doublet H_d causes the mass of the down-type quarks and all charged leptons, while H_u is responsible for the up-type quark masses. The SM Higgs boson is given by a linear combination of H_u^0 and H_d^0. These changes to the Higgs sector are necessary since, among other reasons, using only one supermultiplet based on the SM Higgs boson would lead to a gauge anomaly in the electroweak gauge symmetry and therefore to an inconsistent quantum theory. To account for gravitation, an additional boson called graviton G is added to the SM (cf. Fig. 2.2).
Similarly to the situation in the electroweak sector described in Sec. 2.2.1 the gauge eigenstates, namely bino $\widetilde{\mathrm{B}}$, winos $\widetilde{\mathrm{W}}$, and higgsinos $\widetilde{\mathrm{H}}$, mix to mass eigenstates. These mass eigenstates can be grouped by their electrical charge into charginos $\tilde{\chi}^{\pm}_{1,2}$ and neutralinos $\tilde{\chi}^{0}_{1\text{-}4}$, where higher indices correspond to larger masses (cf. Fig. 2.2).

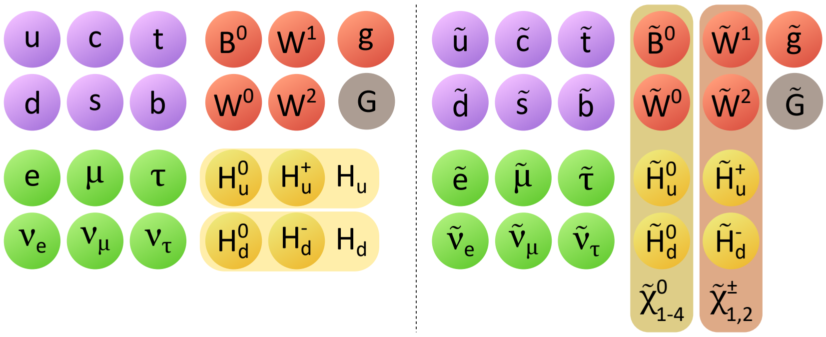

Figure 2.2: Particle content of the minimal supersymmetric standard model. The left side covers the standard model content. The SM particles are grouped into quarks (purple), leptons (green), gauge eigenstates (red), and two Higgs doublets (yellow), while the corresponding SUSY particles are shown on the right. Gauginos (red) and higgsinos (yellow) mix to the mass eigenstates $\tilde{\chi}^{0}_{1\text{-}4}$ and $\tilde{\chi}^{\pm}_{1,2}$.

The theory of supersymmetry can account for several shortcomings of the SM. The three coupling constants can have a common intersection point at high energies enabling the unification of forces [34]. In addition, the hierarchy problem can be solved, since the contributions to Δm_H^2 due to bosonic loops have a relative minus sign compared to the ones by fermionic loops (cf. Eq. (2.3)), which allows for the absorption of the large corrections to the Higgs mass. Furthermore, R-parity conserving SUSY theories can provide an adequate dark matter candidate solving the dark matter problem. The R-parity, which is given by

$$R = (-1)^{3B+L+2S}\,, \tag{2.4}$$

includes baryon number B, lepton number L as well as the spin S. The baryon and lepton numbers equal $+1$ and -1 for the corresponding particles and antiparticles, respectively. Thus, the R-parity of SM particles is given by $+1$ while for SUSY particles it equals -1. Since the conservation of the three quantum numbers (B, L, S) holds for all measurements so far [34], R-parity could be conserved as well, which is assumed in the following. This leads to two main consequences. On the one hand, SUSY particles can only be produced in pairs. On the other hand, the lightest supersymmetric particle (LSP), which is included in the final state of each decay chain containing SUSY particles, has to be stable. If the LSP is electrically neutral, which holds for most of the R-parity conserving SUSY theories, it can be a dark matter candidate.

2.3.1 Gauge-mediated Supersymmetry Breaking

Since none of the predicted sparticles have been observed so far, SUSY has to be a broken symmetry, which allows for mass differences between the superpartners [7]. The symmetry breaking in SUSY can be achieved by introducing a hidden sector. This sector causes the breaking per se, which is then mediated to the MSSM (visible sector). There are different theories about how the breaking is mediated between the two sectors. The most popular way is to describe the mediation via gravitation, whereas this thesis will focus on SUSY scenarios, which feature gauge-mediated symmetry breaking [7, 35].

To cover a large number of different gauge-mediated models the general gauge-mediation framework (GGM) [36–38] is used, among others, for the final interpretation. In this framework, the SM gauge interactions are the only source of communication between the hidden sector and the MSSM. In addition, GGM does not consider different realizations of the hidden sector used by various gauge-mediated models but describes the effects of SUSY breaking based on a completely arbitrary hidden sector.
With this definition of GGM, the framework itself yields two of the main generic predictions of gauge-mediation models. Since gauge interactions are flavor independent (e.g., the coupling of electrons and muons to Z^0 is the same), flavor universality among the sfermions is guaranteed. Furthermore, the gravitino, the superpartner of the graviton, is the lightest supersymmetric particle, which could account for dark matter to some extent. Besides these two predictions, which are made by every gauge-mediation model, there are additional sfermion mass relations in the GGM:

$$\begin{aligned} m_L^2 &= m_Q^2 + m_U^2 - 2m_D^2 \\ m_E^2 &= 3\left(m_U^2 - m_D^2\right) . \end{aligned} \tag{2.5}$$

Each m denotes the sfermion mass of a different flavor. The indices are given by the five flavor groups[3] of the SM. With these relations for the sfermion masses the initial parameter space of the MSSM combined with SUSY breaking, which includes up to 105 free parameters, is strongly reduced. The full phase space can be spanned by eight independent parameters:

$$M_1,\ M_2,\ M_3,\ m_Q^2,\ m_U^2,\ m_D^2,\ \mu,\ \text{and}\ M_{mess} \tag{2.6}$$

Here, $M_{1,2,3}$ are given by the bino $\widetilde{\mathrm{B}}$, wino $\widetilde{\mathrm{W}}$, and gluino $\widetilde{\mathrm{g}}$ mass, respectively. These masses as well as all other parameters are defined at the messenger scale M_{mess}, which also corresponds to the scale where Eq. (2.5) holds. In addition, the Higgs mass parameter μ is used as an input parameter in the GGM. The gap between M_{mess} and the weak scale, which is currently accessible by experiments, can be of the order of up to 15 magnitudes. Thus, due to renormalization group (RG) running the parameters in (2.6) can be significantly modified at the weak scale [7].

[3] Left-handed quarks (Q), right-handed up-type (U), and down-type anti-quarks (D), left-handed leptons (L) and right-handed anti-leptons (E)

2.3.2 Signal Scenarios

The interpretation of the combination performed in this thesis will be mainly focused on two different GGM signal scenarios [38, 39]. With the recent discovery of the Higgs boson and its measured mass of $m_h = 125$ GeV [34], there are some constraints on the spectra of sparticles. In particular, small stop masses in the order of 1 TeV can conflict with the size of the measured Higgs mass. To avoid such conflicts the squark masses, including the stop mass, are set to high values ($8 - 10$ TeV), which satisfies the Higgs mass constraints in a trivial way.
The stable gravitino $\widetilde{\mathrm{G}}$ is the LSP in gauge-mediated scenarios. Thus, the final states, which could be observed by the detector, are determined by the next-to-lightest supersymmetric particle (NLSP), given by the lightest neutralino $\widetilde{\chi}_1^0$, decaying to its SM superpartner and the LSP. To ensure NLSP decays inside the detector, which are necessary for the GGM scenarios to become accessible for the analyses used in the combination, the NLSP decay width given by

$$\lambda_{\widetilde{\chi}_1^0 \to X\widetilde{\mathrm{G}}} = \frac{m_{\widetilde{\chi}_1^0}^5}{48\pi m_{3/2}^2 M_P^2} \tag{2.7}$$

has to be taken into account. Here $m_{\widetilde{\chi}_1^0}$ and $m_{3/2}$ denote the NLSP and gravitino mass, respectively, while M_P stands for the reduced Planck mass. With Eq. (2.7), the decay length of the NLSP can be derived by

$$l_{\widetilde{\chi}_1^0} = \frac{\hbar c}{\lambda_{\widetilde{\chi}_1^0 \to X\widetilde{\mathrm{G}}}} \approx 53\ \mu\mathrm{m} \left(\frac{200\ \mathrm{GeV}}{m_{\widetilde{\chi}_1^0}}\right)^5 \left(\frac{m_{3/2}}{10\ \mathrm{eV}}\right)^2 . \tag{2.8}$$

Fixing the gravitino mass to $m_{3/2} = 10$ eV for both GGM scenarios used in the combination ensures prompt NLSP decays on the detector scale.

Since the squark masses are set to large values to satisfy the Higgs mass constraints and the gluino masses turn out to be large as well (cf. Sec. 6.2.1), the production channels for the GGM scenarios at the LHC are based on electroweak production. The implicit production mechanisms are shown as a blob in Figure 2.3, since different channels can contribute to the production

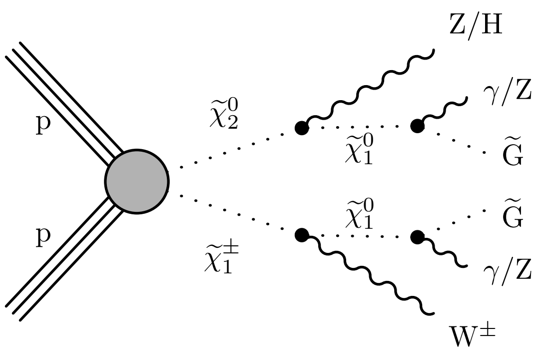

Figure 2.3: One possible GGM diagram with $\widetilde{\chi}_1^\pm \widetilde{\chi}_2^0$ production. The $\widetilde{\chi}_2^0$ line of the upper leg including its decay can be removed to illustrate $\widetilde{\chi}_1^\pm \widetilde{\chi}_1^0$ production, while $\widetilde{\chi}_1^\pm \widetilde{\chi}_1^\mp$ production can be achieved by replacing the upper leg by the lower leg of the diagram.

itself. Each of the channels yields an initial state with two nearly mass degenerate gauginos, which decay further determining the final state. In total there are three different combinations of gauginos accessible in the GGM scenarios. These combinations are given by $\widetilde{\chi}_1^{\pm}\widetilde{\chi}_1^{\mp}$, $\widetilde{\chi}_1^{\pm}\widetilde{\chi}_1^0$, and $\widetilde{\chi}_1^{\pm}\widetilde{\chi}_2^0$ production, with their relative abundance depending on the input parameters.

The decay chain for each of the gauginos, which can be produced in the initial state, is shown in Figure 2.3. The main focus lies on the $\widetilde{\chi}_1^0$ decay, since this decay corresponds to the only source of photons, which are essential for each of the analyses used in the combination. Besides the $\widetilde{\chi}_1^0$ decaying to γ and $\widetilde{\mathrm{G}}$, the photon can also be substituted by a Z boson leading to final states with additional fermions. The corresponding branching fractions of the $\widetilde{\chi}_1^0$ for these two decays are determined by the composition of the neutralino and depend, similar to the abundance of the production processes, on the GGM input parameters.
Two different GGM signal scenarios will be used for the interpretation. The statements made before hold for both of these scenarios. However, they differ in the way the remaining parameters, mainly the gaugino mass parameters M_i, are chosen. The main properties caused by these different choices as well as the different gaugino decays are discussed in detail in Sec. 6. Since based on the choice of the GGM input parameters several production channels and gaugino decay modes are accessible, in the following both GGM scenarios are referred to as full scenarios.

In addition to the two GGM scenarios, several simplified models (SMS) [40] will be used for the final interpretation. In contrast to the full GGM scenarios, these models usually contain fixed branching fractions for the gaugino decays, and only the gaugino masses are changed within the models. Besides the electroweak production, which is present in the GGM scenarios, for the SMS also strong gluino pair production is accessible due to lower gluino masses (cf. Fig. 2.4).

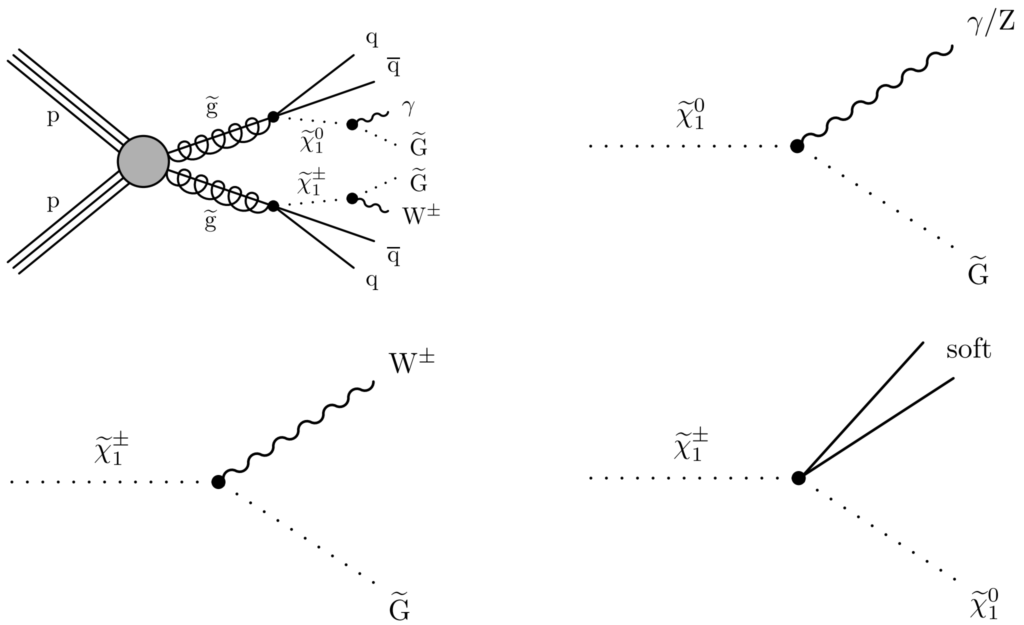

Figure 2.4: The upper left diagram corresponds to strong gluino pair production with charged and neutral gluino decay. In the upper right diagram the $\widetilde{\chi}_1^0$ decay, where the branching fraction to $\gamma\widetilde{\mathrm{G}}$ and $\mathrm{Z}\widetilde{\mathrm{G}}$ is varied, can be seen. In addition, two possible $\widetilde{\chi}^{\pm}$ decays to $\mathrm{W}\widetilde{\mathrm{G}}$ (lower left) and $\widetilde{\chi}_1^0$ + soft (lower right) are shown.

To interpret the single analyses as well as the combination regarding different final states the gaugino branching fractions (cf. Fig. 2.4) are scanned for the different SMS. These variations are possible in case of the simplified models, whereas for the GGM scenarios the underlying full model would be spoiled. In detail, the branching fraction of the NLSP decay is varied between $\mathrm{Z}\widetilde{\mathrm{G}}$ and $\gamma\widetilde{\mathrm{G}}$ for the electroweak case corresponding to the neutralino branching fraction scan. In the chargino branching fraction scan, which features electroweak production, the decay of the lightest chargino is varied between $\mathrm{W}^{\pm}\widetilde{\mathrm{G}}$ and $\widetilde{\chi}_1^0$+soft. Here, the neutralino decays further to $\gamma\widetilde{\mathrm{G}}$ and soft denotes an off-shell $\mathrm{W}^{\pm}$, which leads to low-momentum particles not recovered by the detector. In case of strong gluino pair production, the gluino branching fraction for the neutral and charged decay is equally set to 50%, which for example can lead to signatures shown in the upper left part of Fig. 2.4.

These additional interpretations are motivated by the prospect of separating the contributing analyses by their specific final states. Performing the combination on simplified models might also allow for a better understanding of the more complex GGM scenarios. Furthermore, by using the strong gluino pair production scenario the combination can be interpreted with respect to strongly produced SUSY, which is not present in the two GGM scenarios.

3 Limit Setting

The primary goal of this thesis is to combine four individual analyses and interpret the results in the context of SUSY. Since none of the four analyses observed a significant deviation from the standard model prediction [12–15], the interpretation focuses on upper exclusion limits for the signal strength, which can be for a given signal scenario translated to limits on parameters such as sparticle masses. Each of the four analyses is designed as a multi-bin counting experiment. Thus, the result of the combination is given by a set of statistical independent search bins. For each of these bins a background prediction, the observed data, and a signal prediction, depending on the signal scenario under test, are available. Out of these three quantities, exclusion limits can be derived by the method explained in this chapter.

3.1 Profiled Likelihood Test Statistic

The result of a counting experiment can be interpreted in terms of a hypothesis test [41–43]. Here, the null hypothesis is given by the assumption that the SM background processes account entirely for the observed data. The alternative hypothesis is that the signal scenario under test is realized in nature and contributes to the observation. To separate these two hypotheses with respect to the outcome of the experiment a test statistic is used. Following the Neyman-Pearson lemma [44], which states that the ratio of two likelihoods is the most powerful discriminator for a hypothesis test, the test statistic used in the following is in general given by

$$q = -2\ln\frac{\mathcal{L}(data|signal + background)}{\mathcal{L}(data|background)}\ . \tag{3.1}$$

Both $\mathcal{L}$ denote likelihoods which are mainly based on a product of multiple Poisson probabilities (cf. Eq. (3.2)) assuming one of the two hypotheses for *signal + background* and *background*. With this ratio, the *background* hypothesis is favored for $q > 0$ while for $q < 0$ the *signal + background* hypothesis is favored.

Signal and background prediction, both used to evaluate the test statistic, are subject to multiple uncertainties. In order to account for these uncertainties in the limit setting, nuisance parameters θ are included in the likelihood. The resulting likelihood can in detail be written as

$$\begin{gathered}\mathcal{L}(data|\mu,\theta) = \prod_i \frac{(\mu s_i + b_i)^{n_i}}{n_i!} e^{-\mu s_i - b_i} \cdot p(\tilde{\theta}|\theta) \\ s_i = s_i(\theta),\, b_i = b_i(\theta)\ .\end{gathered} \tag{3.2}$$

Signal and background prediction for each search bin i, which both depend on the set of nuisance parameters θ, are given by $s_i(\theta)$ and $b_i(\theta)$, respectively. The observed count is denoted by n_i and μ is the signal strength parameter, which changes the signal cross section and is equal to zero for the null hypothesis. To take the distribution of the nuisance parameters into account, the product of Poisson probabilities is multiplied by the underlying probability density function (pdf) $p(\tilde{\theta}|\theta)$, where $\tilde{\theta}$ denotes the default values of the nuisance parameters. This pdf is either based on a log-normal, a gamma, or a log-uniform distribution, depending on the origin of the uncertainty and on the analysis using the corresponding nuisance.

With the test statistic given by Eqs. (3.1) and (3.2), an experimental result showing downward fluctuations with respect to the background prediction would lead to a stronger limit on the signal strength. To avoid this behavior caused by a negative signal strength, the corresponding parameter μ is forced to be positive. In addition, the test statistic is chosen to be one-sided, since only upper limits are set in the interpretation leading to a profiled likelihood test statistic given by

$$\tilde{q}_\mu = -2\ln\frac{\mathcal{L}(data|\mu,\hat{\theta}_\mu)}{\mathcal{L}(data|\hat{\mu},\hat{\theta})}\ , \quad 0 \leq \hat{\mu} \leq \mu\ . \tag{3.3}$$

Here $\hat{\mu}$ and $\hat{\theta}$ correspond to the global maximum of the likelihood while $\hat{\theta}_\mu$ refers to the likelihood maximum under the condition of μ.

3.2 The CL$_S$ Method

In order to set upper exclusion limits on the signal strength μ based on the test statistic $\tilde{q}_\mu$ the modified frequentist CL_s method is used [41–43]. In this method, the limit is calculated not based on a single confidence level but on the ratio of confidence in the *signal + background* (CL_{s+b}) to the *background* hypothesis (CL_b):

$$CL_s = \frac{CL_{s+b}}{CL_b} = \frac{p_\mu}{1-p_b}\ . \tag{3.4}$$

The p-values of the two hypotheses for a given observed value of the test statistic are denoted as p_μ and p_b (cf. Fig. 3.1). These p-values can be calculated as follows:

$$p_\mu = P(\tilde{q}_\mu \geq \tilde{q}_\mu^{obs}|signal + background) = \int_{\tilde{q}_\mu^{obs}}^{\infty} f(\tilde{q}_\mu|\mu,\hat{\theta}_\mu^{obs})\, d\tilde{q}_\mu\ , \tag{3.5}$$

$$1 - p_b = P(\tilde{q}_\mu \geq \tilde{q}_\mu^{obs}|background) = \int_{\tilde{q}_\mu^{obs}}^{\infty} f(\tilde{q}_\mu|0,\hat{\theta}_0^{obs})\, d\tilde{q}_\mu\ . \tag{3.6}$$

Here, $\tilde{q}_\mu^{obs}$ denotes the observed value of the test statistic. The integrand of both equations is given by a pdf of the test statistic $\tilde{q}_\mu$. For the first p-value, this pdf is constructed assuming the *signal + background* hypothesis, where a signal with strength μ is present, and the nuisance parameters $\hat{\theta}_\mu^{obs}$ fit the observation for the corresponding hypothesis. For the second p-value, the pdf is built for the *background* hypothesis, which is similar to the method described above with μ set to zero. A more detailed discussion of the pdfs and their construction, which can be based on pseudo-data or an approximative description, can be found in the next section.
The signal strength parameter μ is the only free parameter left in the CL_s method. Thus, using the observation to calculate $\tilde{q}_\mu^{obs}$ and $\hat{\theta}_{\mu,0}^{obs}$, a confidence level can be assigned to each signal parameter by applying Eq. (3.4). The upper exclusion limit on the signal strength μ at a confidence level of $(1-\alpha)$, which is commonly chosen to be 95%, is then given by $\mu_{(1-\alpha)}$ with $CL_s(\mu_{(1-\alpha)}) = \alpha$. Since the signal scenario under test refers to a signal strength of one, the *signal + background* hypothesis can be ruled out at a confidence level of 95% if $\mu_{95\%} < 1$.

The use of CL_s instead of the single confidence level CL_{s+b} is mainly motivated by experimental results which show downward fluctuations with respect to the background prediction. Using CL_{s+b} a signal strength of zero could be excluded by such downward fluctuations. By

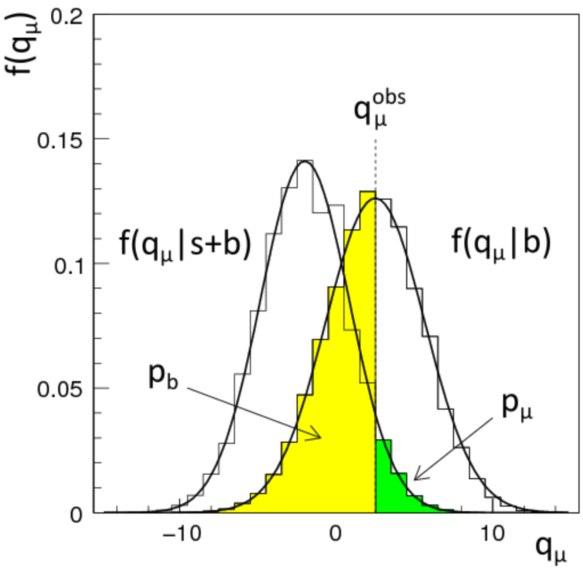

Figure 3.1: Sketched distribution [modified from [45]] of a test statistic q_μ, which with respect to the shown distributions equals the profiled likelihood test statistic $\tilde{q}_\mu$. The distributions under the *background* hypothesis $f(q_\mu|b)$ and the *signal* + *background* hypothesis $f(q_\mu|s+b)$ are shown. Both are derived from toy data (histograms) and from the asymptotic formula (curves). The observed value of the test statistic is given by q_μ^{obs}. In addition, the probabilities p_b (yellow) and p_μ (green) used for the CL_s are shown. Here, the observation is constructed to fit the mean background prediction.

construction of the CL_{s+b} method, 5% of all searches would exclude the *background* hypothesis ($\mu = 0$) at a confidence level of 95%. Even though this is a valid statistical statement, it should be interpreted such that the probability of observing a similar or stronger limit in a future experiment is less than 5%. To avoid this situation, the consistency between background prediction and observation is taken into account using the CL_s method. Thus, downward fluctuations with respect to the background prediction would result in a small denominator in Eq. (3.4) and therefore to a lower confidence level for excluding a signal strength of zero compared to CL_{s+b}. With the consistency between background prediction and observation taken into account, the CL_s method in general results in more conservative limits.

3.3 Asymptotic Approximation

When applying the CL_s method, the pdfs of the test statistic $\tilde{q}_\mu$ under the assumption of the alternative hypothesis $f(\tilde{q}_\mu^{obs}|signal + background)$ and the null hypothesis $f(\tilde{q}_\mu^{obs}|background)$ have to be available. These distributions are usually constructed by pseudo-data sets, which are simulated based on the two hypotheses [43]. Calculating the test statistic for these data sets leads to distributions which follow the pdfs in question (cf. Fig. 3.1). This procedure has to be repeated multiple times to find the signal strength parameter matching the conditions of $\mu_{95\%}$ resulting in a computing intensive method due to the simulation of multiple pseudo-data sets.
To save computing time an asymptotic approximation of the test statistic, which allows for a parametrized formulation of the pdfs, is used in this thesis [45]. For simplicity, the approximation of the test statistic q_μ, which does not include the constraint of μ being positive, is introduced

in the following. In the asymptotic limit, q_μ is equivalent to the test statistic $\tilde{q}_\mu$, which includes the lower bound of μ. A complete discussion of $\tilde{q}_\mu$ can be found in [45]. In the asymptotic approximation, q_μ can be expressed as

$$q_\mu = \frac{(\mu - \hat{\mu})^2}{\sigma^2} + \mathcal{O}(1/\sqrt{N}) \ , \quad \hat{\mu} \leq \mu \ . \tag{3.7}$$

The data sample size is denoted as N and $\hat{\mu}$ follows a Gaussian distribution with standard deviation σ. With this approximation, the corresponding probability density function for q_μ is in general given by

$$f(q_\mu|\mu') = \Phi\left(\frac{\mu' - \mu}{\sigma}\right)\delta(q_\mu) + \frac{1}{2\sqrt{2\pi q_\mu}} \exp\left[-\frac{1}{2}\left(\sqrt{q_\mu} - \frac{\mu' - \mu}{\sigma}\right)^2\right] \ . \tag{3.8}$$

Within this expression, the delta function is denoted as $\delta(q_\mu)$ and Φ denotes the cumulative Gaussian distribution. To get the pdf under the assumption of the *background* hypothesis, μ' has to be set to zero while for the *signal + background* hypothesis μ' is equal to the signal parameter μ under test. With this, the only unassigned parameter left in Eqs. (3.7) and (3.8) is the standard deviation σ. This parameter is estimated by the use of a so-called Asimov data set, which is defined as a data set where all statistical fluctuation are suppressed, and the observed count as well as all nuisance parameters are set to their expected values. Using the parametrized pdfs and their corresponding cumulative distributions the CL_s can then be calculated by an algebraic formula:

$$CL_s = \frac{1 - \Phi(\sqrt{q_\mu})}{\Phi(\sqrt{q_{\mu,A}} - \sqrt{q_\mu})} \ , \qquad \text{with } q_{\mu,A} = \frac{\mu^2}{\sigma^2} \ . \tag{3.9}$$

Here, $q_{\mu,A}$ denotes the test statistic evaluated with the Asimov data set. For $q_\mu = q_\mu^{obs}$ a confidence level based on the observed count can be assigned to each signal parameter. Thus, following the method introduced in the previous section, the observed limit $\mu_{95\%}^{obs}$ can be calculated. To interpret the results in the absence of data fluctuations, expected limits, which are achieved if the observation would fit the background prediction, are used in the final interpretation. This can be done by replacing $\hat{\mu}$ in Eq. (3.7), which is in case of the observed limits determined by the observation. For $\hat{\mu} = 0$ the observation would fit the background prediction, while $\hat{\mu} = N\sigma$ would correspond to a prediction shifted by N-times the standard deviation σ. Using this replacement Eq. (3.9) solves for the expected upper limit at 95% confidence level

$$\mu_{95\%_N} = \sigma\left[\Phi^{-1}(1 - \alpha\Phi(N)) + N\right] \ , \qquad \text{with } 1 - \alpha = 0.95 \ . \tag{3.10}$$

Thus, the median expected limit is given by $N = 0$, and the 1σ and 2σ uncertainty bands on the expected limit can be derived with $N = \pm 1$ and $N = \pm 2$, respectively.

4 Experimental Setup

All four analyses used in the combination are based on the study of high energy proton-proton collisions. These collisions are produced at the currently most powerful particle collider, the Large Hadron Collider, which is run by the European Organization of Nuclear Research (CERN) near Geneva. The Compact Muon Solenoid, which is a general-purpose particle detector located at one of the interaction points of this collider, recorded the data used by all four searches. In this chapter, the collider and the detector along with its subcomponents will be briefly introduced.

4.1 The Large Hadron Collider

The Large Hadron Collider (LHC) [8] based at CERN is currently the largest and most powerful particle collider. It has a circumference of 26.7 km and was built in the tunnel of the old Large Electron-Positron Collider (LEP) [46] at a depth between 45 m and 170 m underground. The collider is designed to collide protons at a center-of-mass-energy $\sqrt{s}$ of up to 14 TeV and heavy ions with an energy up to 2.76 TeV per nucleon.
The particle collisions, which occur at four interaction points at the LHC, are detected by four different experiments (cf. Fig. 4.1). Two of these experiments, namely ATLAS (A Toroidal LHC Apparatus) [9] and CMS (Compact Muon Solenoid) [10], are general-purpose detectors designed to perform SM precision measurements as well as searches for physics beyond the standard model. The third experiment, LHCb (Large Hadron Collider beauty) [47], is a forward detector specialized for the detection of heavy flavor quarks, which for example allows for studies on CP-violation. The fourth experiment, ALICE (A Large Ion Collider Experiment) [48], is a detector specially designed for heavy ion collision to study the quark-gluon plasma.

To achieve collisions with a center-of-mass energy up to 14 TeV at the LHC the protons are accelerated before entering the LHC itself. For this pre-acceleration a linear accelerator as well as three different synchrotrons are used (cf. Fig. 4.1), which accelerate the protons to an energy of 450 GeV. Following the pre-acceleration, every 25 ns around 10^{11} protons are injected in up to 2808 bunches into the two beam pipes of the LHC. Here, the protons are further accelerated to an energy of up to 7 TeV allowing for collisions with the center-of-mass energy stated above. Currently, the LHC is operated at $\sqrt{s} = 13$ TeV, which almost matches the design value of 14 TeV.
An additional measure for the performance of a particle collider is given by the instantaneous luminosity $\mathcal{L}$ and the integrated luminosity L_{int} [49]:

$$\mathcal{L} = \frac{n_b f N^2 F}{4\pi\sigma_x\sigma_y} \,, \qquad L_{int} = \int \mathcal{L} \cdot dt \,. \tag{4.1}$$

Here, n_b denotes the number of bunches per beam, N is the number of particles per bunch, and f is given by the revolution frequency of the bunches. The additional factor F takes losses due to the crossing angle at the interaction point into account. The denominator $4\pi\sigma_x\sigma_y$ accounts for the beam geometry, where σ_x and σ_y are given by the Gaussian widths of a bunch with respect to the plane perpendicular to the beam direction. Using the instantaneous luminosity, the expected rate $\dot{N}$ of a process with cross section σ can be derived by $\dot{N} = \mathcal{L}\sigma$. The integrated luminosity L_{int}, in contrast, determines the total number of events for a given process in a given data set.

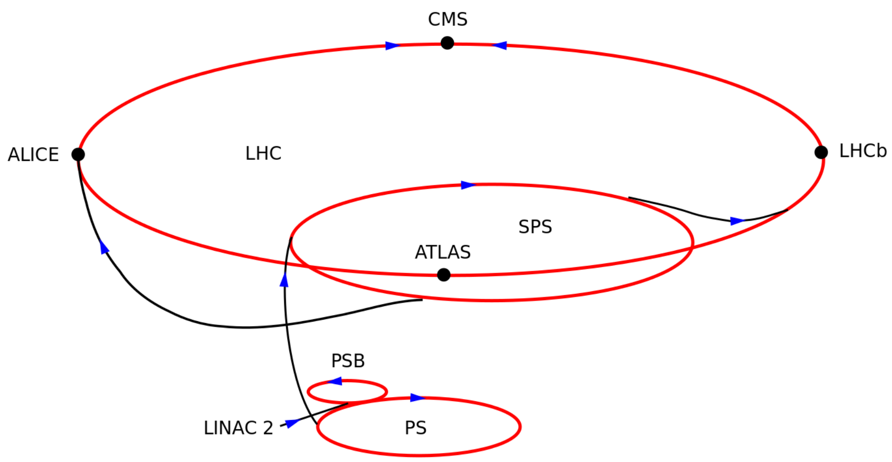

Figure 4.1: Different steps of the proton acceleration process at the LHC [modified from [50]]. Before the proton injection into the LHC, the protons run through a linear accelerator (LINAC 2) and three synchrotrons (PSB, PS, and SPS). In addition, the four experiments at the interaction points of the LHC are indicated.

4.2 The Compact Muon Solenoid

The CMS detector [10] is a multi-purpose detector located at one of the interaction points of the LHC. It is divided into four different subdetectors cylindrically placed around the interaction point (cf. Fig. 4.2). The tracker, measuring the tracks of charged particles, is the innermost part of the detector. Two calorimeters, which measure the energies of different types of particles, are located around the tracker. The outermost part of the detector is the muon system, which detects muons escaping the calorimeters. Each of the subdetectors is separated into two main parts. The part shown in Fig. 4.2 is called barrel and encloses the beam pipe around the interaction point. In addition, each subdetector has two endcaps, which close both open ends of the barrel around the beam pipe.
Another main feature of the CMS detector is the large superconducting solenoid located between the calorimeters and the muon system. This magnet, which is cooled to about 4.5 K, provides an almost homogeneous magnetic field of 3.8 T in the inner part of the detector. The whole detector measures 21.6 m in length and has a diameter of 14.6 m. The following paragraphs briefly introduce the coordinate system as well as the four subdetectors and the trigger system of the CMS detector.

Coordinate system

A coordinate system centered around the interaction point, which matches the features of the CMS detector, is defined as follows. The x-axis is pointing towards the center of the LHC, and the z-axis is parallel to the beam axis, which points in the direction of the beam moving counter-clockwise in the collider. The y-axis is then chosen to point upwards resulting in a right-handed coordinate system. Particle trajectories inside the detector are described based on spherical coordinates. To simplify the discussion of tracks from relativistic particles, the pseudorapidity

$$\eta = -\ln\left(\tan\frac{\theta}{2}\right) \tag{4.2}$$

is used instead of the polar angle θ. Thus, distances with respect to the beam plane are stated in $\Delta\eta$, which is, in contrast to $\Delta\theta$, invariant against Lorentz boosts along the z-axis in the limit of massless particles. In addition, $\Delta\phi$ is used to measure distances regarding the plane perpendicular to the z-axis, while ΔR, given by

$$\Delta R = \sqrt{(\Delta\eta)^2 + (\Delta\phi)^2} \,, \tag{4.3}$$

states combined distances. Regarding the coordinate system used in this thesis, particle momenta as well as energies are in the following usually projected to the transverse plane perpendicular to the beam axis (p_{T} and E_{T}).

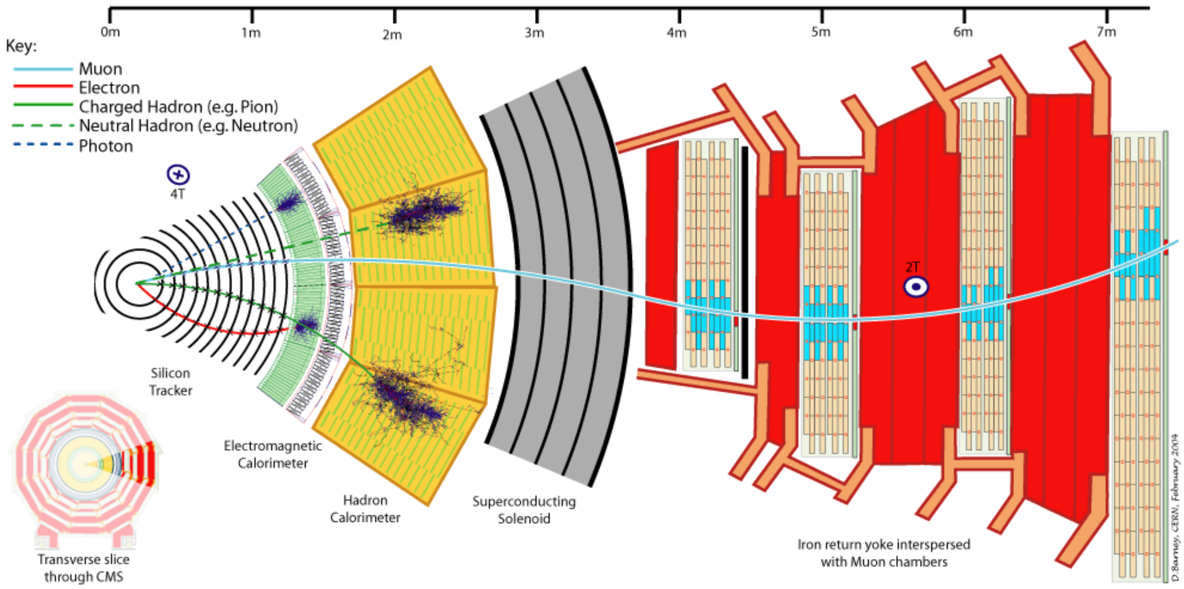

Figure 4.2: A transverse slice of the CMS detector [51]. The different subdetectors as well as the superconducting solenoid are shown. In addition, starting at the interaction point, signatures for various particle types in the different parts of the detector can be seen.

Tracker system

The tracker system, which starts at a distance of 4.4 cm to the center of the beam pipe and extends to a radius of 1.3 m, is the innermost subdetector. It measures the trajectory of charged particles emerging the beam pipe and is divided into two parts. The part next to the interaction point is composed of a silicon pixel detector, which covers an area of around 1 m^2. On this area, a total amount of 66 million pixels are used for detection allowing for a spacial resolution of $\sim$ 15 µm. The second part of the tracker, which is built around the pixel detector, is a silicon strip detector, which includes a total of 9.3 million strips. With both parts combined the tracker system covers the range of $|\eta| < 2.5$.
Charged particles flying through the tracker system result in hits in the different layers of the tracker, which are used to reconstruct the particle trajectories. Due to the curved trajectories caused by the magnetic field inside the tracker not only the particle tracks but also the momenta of charged particles can be measured. A resolution of 1 to 2% can be achieved up to $|\eta| \approx 1.6$ for high momentum particle tracks around 100 GeV. This resolution decreases for lower momenta as well as for larger values of $|\eta|$.

Calorimeter systems

The CMS detector consists of two different calorimeters, the electromagnetic calorimeter (ECAL) and the hadronic calorimeter (HCAL), which are both mainly used to measure the energy of particles stopped in the corresponding calorimeter.
The ECAL, which covers the range up to $|\eta| < 3.0$, is built around the tracker system and extends to a radius of 1.77 m. Here, more than $7 \cdot 10^4$ lead tungstate ($PbWO_4$) crystals are used to essentially identify photons and electrons and measure their energy. Particles interacting with the $PbWO_4$ detector material produce electromagnetic showers inside the crystals. Due to scintillating features of the material the showers result in multiple photons, which are detected by photodiodes and phototriodes in the barrel and endcap part, respectively. Thus, the total energy of all scintillation photons caused by a particle, which is stopped in the ECAL, should match the initial particle energy. By this method, an energy resolution, which depends on the measured energy itself, of around 0.5% can be achieved for electrons with 120 GeV.
The HCAL is located around the ECAL, covers a total range of $|\eta| < 5.2$, and extends to a radius of 2.95 m. Here, a different technique to the one described above is used to measure the energy of hadrons included in jets, which were initially produced by quarks and gluons. The main difference to the technique used in the ECAL is that the HCAL consists of two different types of layers, which are stacked in an alternating way. Incoming hadrons crossing the brass absorber layers produce hadronic showers via strong interactions. These showers are then measured by plastic scintillators, which build the second type of layers. In the HCAL an energy resolution of $120\%/\sqrt{E}$ for a single pion with energy E can be achieved in the barrel [52].

Muon system

Muons, which usually escape both calorimeters without leaving a signal, are detected in the muon system, which corresponds to the outermost part of the CMS detector. It extends to the full radius of the detector (7.3 m), covers a range of $|\eta| < 2.4$, and is embedded into the flux-return yoke of the solenoid. Three different detector types are used to measure the muon trajectories. The barrel region of the muon system consists of drift tubes, while in the endcap part cathode strip chambers are used. To improve the trigger performance of the muon system, additional resistive plate chambers are installed in the area of $|\eta| < 1.6$.
Embedding the muon system into the flux-return yoke allows for the use of the homogeneous magnetic field inside the yoke itself, which is close to zero in the remaining parts of the muon system, since the muon system is installed outside the solenoid (cf. Fig. 4.2). Thus, the curved trajectories of the muons can be exploited, similar to the method used in the tracker, to measure the muon momenta. With this, a momentum resolution of around 9% can be achieved for momenta up to 200 GeV and small $|\eta|$ without including information from the tracker system.

Trigger system

To manage the huge event rate delivered by the LHC, which is of the order of 40 MHz, a two-step trigger system is used [53, 54]. The first step corresponds to the Level-1 trigger (L1), which is purely based on electronics. Here, the event rate is reduced to a maximum of 100 kHz using information from both calorimeters and the muon system. This rate is further reduced by the High-Level Trigger (HLT), which accounts for the second step of the trigger system. In the HLT a software system exploiting information from all subdetectors is used to reduce the event rate by an additional factor of 10^3. Thus, the initial event rate, which would be impossible to store, can be reduced by a total factor of around 10^5 trying to keep only events of possible interest at a rate of the order of 1 kHz.

5 Event Reconstruction and Background Simulation

The final interpretation of the combination is mainly based on the signal prediction, depending on the signal scenario under test, the observed data, as well as the background prediction for each search bin. In each of the four independent analyses, the latter two yields are derived using data sets recorded by the CMS detector and Monte-Carlo simulations of standard model processes. In this chapter, the data sets including the triggers used by the four analyses are introduced. Furthermore, the procedure of SM Monte-Carlo simulation as well as the object definitions used for the event reconstruction are briefly explained.

5.1 Data Sets and Triggers

The data sets used by the analyses were recorded by the CMS detector in 2016 at a center-of-mass energy of 13 TeV and correspond to an integrated luminosity of 35.9 fb^{-1} [11]. The complete list of data sets can be found in Appx. 1. Due to the different final states targeted by the analyses multiple high-level triggers, which are summarized in Tab. 5.1, are used. The corresponding trigger efficiencies were derived by the individual analyses.

Table 5.1: Summary of the triggers grouped by the corresponding analyses. The last column states the efficiencies derived in the individual analyses. The first two Photon+Lepton triggers are combined with a logical disjunction. In case of the Diphoton analysis, no uncertainty on the efficiency was available.

Analysis	Trigger	ϵ (%)
Photon+S_T^γ	*HLT_Photon165_HE10*	94.3 ± 0.4
Photon+H_T^γ	*HLT_Photon90_CaloIdL_PFHT600*	96 ± 4
Photon+Lepton	*HLT_Mu17_Photon30_CaloIdL_L1Iso*	94 ± 4
	HLT_Mu38NoFilterNoVtx_Photon38_CaloIdL	
	HLT_Diphoton30_18_R9Id[4]	96 ± 4
Diphoton	*HLT_Diphoton30_18_R9Id*[4]	97.2

The Photon+S_T^γ analysis targets final states, which are mainly characterized by the presence of at least one high-momentum photon. Thus, the SinglePhoton primary data set[5] (PD) is used. The trigger requires a photon with $p_\mathrm{T} > 165$ GeV, where the fraction of energy deposited by the photon candidate in the HCAL compared to the ECAL is not allowed to exceed 10%.
As in the Photon+S_T^γ analysis, the SinglePhoton PD is also used for the Photon+H_T^γ search. The targeted final state is defined by a photon and a large amount of hadronic activity. These characteristics are covered by a trigger, which requires a photon with $p_\mathrm{T} > 90$ GeV and a transverse hadronic activity (H_T) of at least 600 GeV. In addition, the photon has to fulfill a loose calorimeter identification.

[4]Full trigger name: *HLT_Diphoton30_18_R9Id_OR_IsoCaloId_AND_HE_R9Id_Mass90*.
[5]Primary data sets are defined by groups of triggers, which require similar high-level objects.

The final states targeted by the Photon+Lepton analysis are split up depending on the nature of the detected charged lepton, which is required in addition to the photon. For the final states including a muon, two different muon-photon triggers based on the MuonEG PD are used. The first trigger requires a muon with $p_T > 17$ GeV and an isolated photon with $p_T > 30$ GeV, which passes a loose calorimeter identification. The second trigger has a symmetric p_T threshold of 38 GeV and no additional isolation requirements. Since there is no distinction between photons and electrons on trigger level, a diphoton trigger can be used with the DoubleEG PD to select events with an electron accompanying the photon.
The Diphoton analysis, which covers final states with two photons, is based on the same primary data set and trigger. Here, two isolated electromagnetic objects, which have an invariant mass above 90 GeV, are required. In addition, the leading object has to fulfill $p_T > 30$ GeV, while for the subleading object $p_T > 18$ GeV is required.

5.2 Standard Model Background Simulation

Besides background predictions based on data-driven methods, Monte-Carlo (MC) simulations of SM processes are used by each of the four analyses to predict the number of expected background events in the signal regions. A detailed description of the background prediction methods used by the individual analyses is given in Sec. 7, while the following part will focus on the background simulation process itself.

The MC simulation process can mainly be divided into three different steps. In the first step, the particles produced in the proton-proton collision are simulated based on the matrix element, which corresponds to the SM process of interest, by using the MadGraph [55–57] or POWHEG [58–62] event generators. The second step covers the showering of the particles produced in the first step. Here, the hadronization of color-charged particles as well as additional particle radiations, such as photon emission by electrons, can be simulated. For this step, the PYTHIA framework [63] is used, which can also replace the event generators mentioned above. Finally, the interactions between particles and the detector material resulting in the detector response are simulated. This step is provided by GEANT4 [64] based on a detailed implementation of the CMS detector. Due to the last step the MC samples do not only contain information on the generated particles but can also be processed by the same event reconstruction (cf. Sec. 5.3) used for data.

To compare the simulation to data recorded by the CMS detector, additional weights have to be applied to the MC samples. To match the integrated luminosity L_{int} of the CMS data set with respect to the cross section σ of a SM process and the total number of generated events N_{gen}, each of the simulated events is weighted by

$$w = \frac{\sigma \cdot L_{int}}{N_{gen}} \ . \tag{5.1}$$

Independent of the Feynman diagrams considered by the event generators in the first step of the simulation the cross section σ is usually chosen to match the highest available accuracy (e.g., leading order (LO) or next-to-leading order (NLO)).
Another difference between simulation and data is based on the triggers used by the analyses. Two different ways of reweighting are considered. For the first option the simulated events are weighted by the efficiency of the trigger, which is used for the corresponding data set (cf. Tab. 5.1). The second option makes use of the trigger simulation available in the MC sam-

ples. In this case, the simulated events are weighted by the ratio between the trigger efficiency measured in data and the simulated trigger efficiency.
To match the number of proton-proton interactions per bunch crossing (pileup) observed in data each simulated event is overlaid with a certain number of additional events and an additional weight is applied to each simulated event. This weight is derived such that the simulated pileup distribution is reweighted to match the distribution measured in data.

5.3 Object Definitions

Particles produced by proton-proton collisions in the center of the CMS detector result in a large number of signals from the subdetectors. The main task in terms of event reconstruction is to identify each detected particle as well as its kinematics from these signals. At the CMS detector, this task is carried out by combining the information from the different subdetectors using the particle flow (PF) algorithm [65].
In the first step of the PF algorithm, signals from the tracking system, which result from charged particles, are merged into tracks by an iterative tracking algorithm. In addition, energy depositions in both calorimeters are combined into clusters around their local maxima using a clustering algorithm. In the second step, the PF algorithm connects the information from the different subdetectors. Here, the reconstructed tracks can be linked to energy clusters in the calorimeters or depositions in the muon system. In the last step, the particles are identified using the linked entries from the different subdetectors. Thus, the PF algorithm is able to distinguish photons, electrons, and muons as well as neutral and charged hadrons.
In the contributing analyses, supplementary identification criteria (IDs) are applied to the candidates reconstructed by the PF algorithm to further improve the object reconstruction. These criteria as well as additional variable definitions will be covered by the following sections.

5.3.1 Photons

Photons in the CMS detector mainly originate from particle decays or emissions by charged particles. They are reconstructed by the PF algorithm using energy clusters in the ECAL, which are not linked to an electron track[6] in the tracker system. To reduce the rate of other particles being misidentified as a photon a cut-based photon ID [67], which follows the recommendations of the CMS collaboration, is applied in each of the four analyses.
The most significant difference between the analyses is that the photon ID is used at a medium working point (WP) by the Diphoton analysis, while the remaining three analyses choose the loose WP for their definition of signal photons. In addition, endcap photons ($1.566 < |\eta| < 2.5$) are utilized in the background validation method of the Photon+H_T^γ analysis while only barrel photons ($|\eta| < 1.4442$) are used by the other analyses. Besides these differences the four searches are based on a quite similar photon definition, which is mainly given by the photon ID (cf. Tab. 5.2). The parameters used in this photon identification are defined as follows:

$\boldsymbol{H/E}$ is the energy deposited in the HCAL segment, which is closest to the ECAL cluster linked to the reconstructed photon, divided by the energy of the ECAL cluster itself. Since photons are stopped inside the ECAL, there should be no significant energy deposit in the HCAL, which could be linked to the reconstructed photon. Thus, an upper limit on this parameter reduces, among others, the rate of jets being misidentified as photons.

[6] Electron tracks are reconstructed by an Gaussian-sum filter algorithm taking additional bremsstrahlung into account [66]

$\boldsymbol{\sigma_{i\eta i\eta}}$**:** This parameter takes the width of the electromagnetic shower in the ECAL initiated by the photon candidate with respect to the η-coordinate into account. An energy weighted mean distance between the crystal with the highest energy deposition, called seed, to the crystals forming a 5x5 cluster around the seed is calculated. Since hadrons, in contrast to photons, usually initiate showers with a larger expansion, the rate of misidentification caused by jets can be further reduced.

$\boldsymbol{I_{NH}, I_{CH}, I_{PH}}$**:** These requirements are used to suppress the reconstruction of photons originating from jets by only extracting well-isolated photons. Neutral hadrons (NH), charged hadrons (CH), as well as additional photons (PH) reconstructed in a cone of $\Delta R < 0.3$ around the photon are taken into account. The sum of transverse momenta from the corresponding PF candidates is calculated for each of the three particle classes. Upper limits on these sums corrected by additional contributions from pileup are then used to reduce jet contributions.

$\boldsymbol{N_{seed}}$ denotes the number of seeds in the innermost part of the tracking system (pixel seeds) that would allow for the reconstruction of a trajectory between the ECAL cluster and the interaction point. Since electrons create ECAL entries similarly to photons but should also be detected by the tracker system, the rate of electrons misidentified as photons can be significantly reduced by requiring the absence of such seeds.

Table 5.2: Definition of the loose and medium working point for the cut-based photon ID with additional N_{seed} criterion [67]. Here, only the values for the barrel photon are shown. The definitions for the endcap photons vary slightly. The parametrization for I_{NH} is given by $f(p_{\mathrm{T}}) = 0.0148 \cdot p_{\mathrm{T}} + 1.7 \cdot 10^{-5} \cdot (p_{\mathrm{T}})^2$.

Parameter	Loose WP	Medium WP
H/E	< 0.0597	< 0.0396
$\sigma_{i\eta i\eta}$	< 0.01031	< 0.01022
I_{CH}	< 1.295 GeV	< 0.441 GeV
I_{NH}	< 10.910 GeV $+ f(p_{\mathrm{T}})$	< 2.725 GeV $+ f(p_{\mathrm{T}})$
I_{CH}	< 3.630 GeV $+ 0.0047 \cdot p_{\mathrm{T}}$	< 2.571 GeV $+ 0.0047 \cdot p_{\mathrm{T}}$
N_{seed}	< 1	< 1

5.3.2 Electrons

Electrons initiate electromagnetic showers in the ECAL similar to the showers created by photons. However, due to their electric charge, electrons are also detected in the tracking system. Thus, the PF algorithm identifies electrons from ECAL clusters, which can be linked to an electron track reconstructed in the tracker system.
To reduce the rate of misidentified electrons, an additional electron ID [68] is used. The Diphoton analysis identifies electrons based on the loose WP to veto events with charged leptons. In the Photon+Lepton search as well as in the veto strategy of the combination (cf. Sec. 8.2), the medium WP with a small change in the isolation criterion is used. In each case, barrel and endcap electrons are considered. The parameters of the electron ID listed in Tab. 5.3, of which H/E and $\sigma_{i\eta i\eta}$ are already used in the photon ID, are defined as follows:

$\boldsymbol{\Delta\eta_{seed}}$**,** $\boldsymbol{\Delta\phi_{ln}}$ take the distance between the reconstructed trajectory and the corresponding ECAL cluster in η and ϕ, respectively, into account. A good match between cluster and track reduces the rate of false links created by the PF algorithm.

r_{iso}: The relative isolation criterion is used to only reconstruct well-isolated electrons. The contributions from charged and neutral hadrons, as well as photons in a cone of $\Delta R < 0.3$ around the electron relative to the electron p_{T} are taken into account. As for the isolation criterion in the photon ID contributions from pileup are removed. A slightly different isolation criterion, PF mini isolation [69], is used when applying the medium WP.

$|E^{-1} - P^{-1}|$: This parameter is also used to test the agreement between the reconstructed track and the corresponding ECAL cluster. The difference between the inverse energy measured in the ECAL and the momentum derived by the bending of the trajectory is used. Since electrons are nearly massless compared to the measured energy scale, this difference should be small for a correct link between track and cluster.

N_{miss}, Conversion Veto are used to reduce the rate of reconstructed electrons, which originate from pair production caused by an initial photon. Here, N_{miss} denotes the number of missing hits in the tracker, which would be expected for an electron not originating from an initial photon. In addition, a conversion veto, based on a conversion vertex fit probability, is used to further reduce the rate of reconstructing electrons from pair production.

Table 5.3: Definition of loose and medium working point for the cut-based electron ID used for barrel (endcap) electrons [68]. *Relative isolation replaced by PF mini isolation [69].

Parameter	Loose WP	Medium WP
H/E	$< 0.298\,(0.101)$	$< 0.253\,(0.0878)$
$\sigma_{i\eta i\eta}$	$< 0.011\,(0.0314)$	$< 0.00998\,(0.0298)$
$\Delta\eta_{seed}$	$< 0.00477\,(0.00868)$	$< 0.00311\,(0.00609)$
$\Delta\phi_{in}$	$< 0.222\,(0.103)$	$< 0.213\,(0.045)$
r_{Iso}	$< 0.0994\,(0.107)$	$< 0.1\,(0.1)^{*}$
$\lvert E^{-1} - P^{-1}\rvert$	$< 0.241\,(0.14)$ GeV^{-1}	$< 0.134\,(0.13)$ GeV^{-1}
N_{miss}	$< 2\,(2)$	$< 2\,(2)$
Conversion Veto	pass (pass)	pass (pass)

5.3.3 Muons

The reconstruction of muons is performed in two ways resulting in global and tracker muons. For global muons, tracks inside the muon system are reconstructed and then linked to trajectories in the tracker system. For tracker muons, each reconstructed track in the tracker system is assumed to be possibly caused by a muon. If a track can be linked to entries in the muon system, a tracker muon is reconstructed.
The muon identification used by the analyses, which covers the range of $|\eta| < 2.4$, is slightly different. The Diphoton analysis utilized muons, which fulfill a loose identification [70], to veto events with charged lepton. This loose identification does only require the muon to be reconstructed in one of the ways explained above. In addition, the muon has to match a loose isolation similar to the criterion used for the electron ID. The muon identification in the Photon+Lepton search as well as in the veto strategy used for the combination is based on the medium muon ID, which in detail is shown in Tab. 5.4. The requirements can depend on whether the muon is assumed to be a "good" global muon. In contrast to the Diphoton analysis, a medium isolation criterion supplements the identification used in the Photon+Lepton search and in the combination.

There are three different requirements for the muon to be tagged as a "good" global muon. The parameter χ^2_{track}/ndf describes the goodness of the combined fitted trajectory in the tracker system and the muon system using a χ^2 test. The position match and the kink finder ensure a good quality of the trajectory in the tracker system only.
The additional parameters used for both muon categories in the medium muon ID can be explained as follows:

Segment Compatibility: The compatibility of entries inside the muon system is tested and assigned with a score. In addition, the matching between the extrapolated trajectory of the tracking system to the corresponding entries in the muon system is taken into account.

Valid Tracker Hits denote the fraction of valid hits inside the inner tracker system. This requirement does also ensure a good quality of the reconstructed trajectory in the tracker system.

$|d_0|$, $|d_z|$ denote impact parameters, which are given by the transverse and longitudinal distance of the reconstructed trajectory to the primary vertex. By this requirement, the number of muons originating from pileup is reduced.

Table 5.4: Definition of the medium muon ID [70] supplemented by additional impact parameter requirements (last two rows). The limit for the segment compatibility depends on whether the muon matches the "good" global muon requirements.

Parameter	"Good" Global Muon	"Normal" Muon
Loose Muon	true	true
Global Muon	true	-
χ^2_{track}/ndf	< 3	-
Position Match	< 12	-
Kink Finder	< 20	-
Segment Compatibility	> 0.303	> 0.451
Valid Tracker Hits	> 80 %	> 80 %
$\|d_0\|$	< 0.05 cm	< 0.05 cm
$\|d_z\|$	< 0.1 cm	< 0.1 cm

5.3.4 Jets

Quarks and gluons produced in proton-proton collisions eventually result in jets, which are built in the reconstruction by combining neutral and charged hadrons reconstructed by the PF algorithm. Here, the anti-k_T clustering algorithm [71] with a distance parameter of 0.4 is used. In addition, jets have to fulfill the identification criterion shown in Tab. 5.5.
The parameters used in the jet ID predominantly consider energy fractions for different particle classes with respect to the reconstructed jet energy E_{jet}. In addition, the total number of constituents as well as the number of charged hadrons and neutral particles is taken into account. These requirements have been optimized for different $|\eta|$ ranges to ensure a good jet reconstruction.
The $|\eta|$ ranges used for the reconstruction differ between the individual analyses. The Photon+S_T^γ and Photon+H_T^γ searches consider jets in the range of $|\eta| < 3.0$, while the Photon+Lepton analysis reconstructs jets in the range of $|\eta| < 2.5$. In the Diphoton search jets are not used.

Table 5.5: Definition of the jet ID, which is defined for three different $|\eta|$ ranges. Here, h denotes hadrons, while em stands for electromagnetic particles. Both particle classes are separated into charged ($\pm$) and neutral (0) representatives.

Parameter	$\|\eta\| < 2.4$	$2.4 < \|\eta\| < 2.7$	$2.7 < \|\eta\| < 3.0$
E_{h^0}/E_{jet}	< 0.99	< 0.99	< 0.98
E_{em^0}/E_{jet}	< 0.99	< 0.99	> 0.01
$N_{particle}$	> 1	> 1	-
$E_{h^\pm}/E_{jet}$	> 0	-	-
$E_{em^\pm}/E_{jet}$	< 0.99	-	-
$N_{h^\pm}$	> 0	-	-
$N_{particle^0}$	-	-	> 2

5.3.5 Additional Variables

Besides kinematic variables, like the transverse momentum or the longitudinal flight direction of reconstructed particles, additional variables, which combine the properties of multiple particles, are used in the individual analyses as well as in the combination. These variables allow for a better separation between background and signal processes and better classification of different signal scenarios.

The missing transverse momentum $p_{\mathrm{T}}^{\mathrm{miss}}$ (cf. Eq. (5.2)) is one of the main variables used in searches for SUSY. It is motivated by particles, which are not detected by the different subdetectors and escape the experiment without any signal. In case of the considered SUSY scenarios (cf. Sec. 2.3.2) the gravitino, which is the LSP, would match the criterion of such an undetected particle. Here, the missing transverse momentum would provide a measure for the transverse momentum of the escaping gravitino. Thus, the missing transverse momentum is based on all particles reconstructed by the PF algorithm and is defined as

$$p_{\mathrm{T}}^{\mathrm{miss}} = \left|\vec{p}_{\mathrm{T}}^{\mathrm{miss}}\right| = \left|-\sum_{i}^{N} \vec{p}_{\mathrm{T}_i}\right| . \tag{5.2}$$

Due to the negligible transverse momenta of the colliding protons, the summed transverse momenta $\vec{p}_{\mathrm{T}_i}$ of the N reconstructed particles should be zero if each of the produced particles is detected and reconstructed. An undetected particle, however, would lead to an imbalance, which can be quantified by $p_{\mathrm{T}}^{\mathrm{miss}}$. For an ideal measurement of the transverse momenta in the case of only one undetected particle, $p_{\mathrm{T}}^{\mathrm{miss}}$ would match the transverse momentum of this undetected particle by construction. In the case of multiple undetected particles, $p_{\mathrm{T}}^{\mathrm{miss}}$ corresponds to a measure for the transverse momentum sum of all undetected particles.
To measure the mass of a mother particle decaying into two or more daughter particles the invariant mass of the daughter particles is used. Here, the four-momenta of the daughter particles are summed and then transformed into the rest frame of the mother particle. In case of an undetected particle, this construction fails since only the transverse momentum of the undetected particle can be approximated by $p_{\mathrm{T}}^{\mathrm{miss}}$. This problem is addressed by using the transverse mass M_{T}, defined by

$$M_{\mathrm{T}} = \sqrt{2 p_{\mathrm{T}}^{\mathrm{miss}} p_{\mathrm{T}}^{x} \left[1 - \cos\Delta\phi\left(x, \vec{p}_{\mathrm{T}}^{\mathrm{miss}}\right)\right]} , \tag{5.3}$$

as a measure for the mass of the mother particle. Here, x denotes the detected daughter particle, while $p_{\mathrm{T}}^{\mathrm{miss}}$ takes the undetected daughter particle into account. Thus, for the considered SUSY signals the mass of the NLSP, for example, can be approximated by M_{T}.

Besides these commonly used variables there are specific variables characterizing the Photon+H_{T}^{γ} and Photon+S_{T}^{γ} analyses. As the names already imply H_{T}^{γ} is used in the Photon+H_{T}^{γ} search to separate signal scenarios from background processes, while for the same reason S_{T}^{γ} is used in case of the Photon+S_{T}^{γ} analysis. These variables are defined as follows:

$$S_{\mathrm{T}}^{\gamma} = p_{\mathrm{T}}^{\mathrm{miss}} + \sum_{\mathrm{phot.}} p_{\mathrm{T}}^{\gamma} \,, \qquad H_{\mathrm{T}}^{\gamma} = p_{\mathrm{T}}^{\gamma} + \sum_{\mathrm{jets}} p_{\mathrm{T}} \tag{5.4}$$

For the S_{T}^{γ} variable the transverse momenta of all reconstructed photons are combined with $p_{\mathrm{T}}^{\mathrm{miss}}$. In the SM there are no processes, where a photon and a neutrino are correlated, which could result in large S_{T}^{γ}. In the SUSY scenarios, in contrast, the NLSP can decay to a photon and a gravitino, where the gravitino accounts for $p_{\mathrm{T}}^{\mathrm{miss}}$ in the event. Thus, SUSY events populate higher S_{T}^{γ} regions compared to SM events, which allows for good separation between SM and SUSY events using the S_{T}^{γ} variable [12].
The H_{T}^{γ} variable, in contrast, is defined by the summed transverse momenta of the leading photon and all reconstructed jets. This variable is specially designed to gain sensitivity for strong SUSY scenarios. In those scenarios, the mass of the SUSY particles can extend to high values. Since the decays of these particles usually contain high-momentum jets as well as high-momentum photons from the NLSP decays, the SUSY events populate higher H_{T}^{γ} regions, where only a small number of SM events is expected. Thus, in the case of strong SUSY scenarios, the H_{T}^{γ} variable ensures good separation between SM and SUSY events [13].

6 Signal Samples

Signal yields based on the signal prediction for a given scenario are required for the final interpretation of the combination. This prediction is derived using simulated signal samples, which are based on the scenarios introduced in Sec. 2.3.2.
The simulation of these samples mainly follows the procedure discussed in Sec 5.2. The only significant difference to the simulation of SM background processes is given by the detector simulation. Here, the full CMS detector simulation implemented in GEANT4 is replaced by the FastSim framework [72], which is based on a simplified description of the CMS detector. With this replacement the computation time needed for the last step of the production procedure can be reduced by a factor of ~ 100 while obtaining similar observable distributions compared to the use of GEANT4.
Different signal scenarios, given by simplified models [40] as well as two full GGM scenarios, are used for the interpretation of the combination. The SMS scenarios have been already used for the interpretation of the individual analyses. Based on the manipulation of these samples the interpretation of the combination is performed on scenarios with variable gaugino branching fractions. Both new GGM models, in contrast, were not used in the initial searches. Thus, the corresponding samples were not available in advance and had to be specially produced for the combination based on model parameters provided by theorists [38, 39]. This procedure and the corresponding cross section calculations for the GGM models as well as the manipulation of the SMS samples are discussed in the following sections.

6.1 Simplified Models and Branching Fraction Scans

Two different scenarios with scanned gaugino branching fractions (BF) and one with a fixed BF are used for the final interpretation. The former two are based on electroweak (EWK) production and include a variable neutralino[7] and chargino BF, respectively. The third scenario is based on strong gluino pair production. Here, the gluino BF is fixed. For all three scenarios, next-to-leading order plus next-to-leading-log (NLO+NLL) production cross sections are available [73–81].

For the EWK production two different SMS samples, namely TChiNg and TChiWg, are available. The masses of the lightest neutralino $\widetilde{\chi}_1^0$ and chargino $\widetilde{\chi}_1^{\pm}$, which are simultaneously varied across the phase space, are assumed to be approximately degenerate. The TChiNg sample is constructed such that each event contains two neutralinos $\widetilde{\chi}_1^0$, each decaying to $\gamma\widetilde{\mathrm{G}}$, $\mathrm{Z}\widetilde{\mathrm{G}}$, and $\mathrm{H}\widetilde{\mathrm{G}}$ with 50, 25 and 25% probability, respectively. In the TChiWg sample, in contrast, each simulated event consists of one neutralino $\widetilde{\chi}_1^0$ decaying to $\gamma\widetilde{\mathrm{G}}$ and one chargino $\widetilde{\chi}_1^{\pm}$ decaying to $\mathrm{W}^{\pm}\widetilde{\mathrm{G}}$.
In the neutralino BF scan the $\widetilde{\chi}_1^0$ decay probability is rescaled between $\gamma\widetilde{\mathrm{G}}$ and $\mathrm{Z}\widetilde{\mathrm{G}}$, while the $\mathrm{H}\widetilde{\mathrm{G}}$ case is neglected assuming no higgsino contributions to $\widetilde{\chi}_1^0$. For this purpose, the simulated events in the TChiNg sample are separated by their final state into $\gamma\gamma$, $\gamma\mathrm{Z}$, and ZZ events. With this separation the BF-dependent signal yield $A(X)$ can be expressed as

$$A(X) = X^2 \cdot A_{\gamma\gamma} + 2 \cdot X \cdot (1 - X) \cdot A_{\gamma\mathrm{Z}} + (1 - X)^2 \cdot A_{\mathrm{ZZ}} \,, \tag{6.1}$$

with the BF of a neutralino decaying to $\gamma\widetilde{\mathrm{G}}$ given by X. For the neutralino BF scan, the combined chargino-chargino and chargino-neutralino production cross section is used. This is possible due to the degenerate mass mentioned above and the assumption that produced charginos decay to

[7] Unless otherwise stated, "neutralino" denotes the lightest neutralino.

neutralinos via soft radiation ($\widetilde{\chi}_1^{\pm} \rightarrow \widetilde{\chi}_1^0 + \text{soft}$), which corresponds to low momentum particles from an off-shell $W^{\pm}$ decay not reconstructed by the detector. Thus, both production channels effectively contain two neutralinos.
For the chargino BF scan, in contrast, the chargino decay probability is rescaled between $W^{\pm}\widetilde{G}$ and $\widetilde{\chi}_1^0 + \text{soft}$ with the neutralino further decaying to $\gamma\widetilde{G}$. This variation results in $\gamma\gamma$, $W^{\pm}\gamma$, and $W^{\pm}W^{\mp}$ final states. The TChiWg sample is used for the $W^{\pm}\gamma$ final state, the $\gamma\gamma$ events are taken from the TChiNg sample, and the $W^{\pm}W^{\mp}$ final state is neglected. The signal yield depending on the chargino BF is then given by

$$A(X) = X^2 \cdot A_{\gamma\gamma} + 2 \cdot X \cdot (1 - X) \cdot A_{W^{\pm}\gamma} \, . \tag{6.2}$$

Here, X denotes the BF for $\widetilde{\chi}_1^{\pm} \rightarrow \widetilde{\chi}_1^0 + \text{soft}$. The chargino BF scan is scaled only to the chargino-chargino production cross section since by construction the production of two charginos is assumed for each event.

In the case of strong gluino pair production one SMS scenario, namely T5Wg, is available. In this scenario, the gluino mass and the mass of the neutralino, which equals the mass of the chargino, are used to span the phase space. The BF for the charged ($\widetilde{g} \rightarrow \widetilde{\chi}_1^{\pm} + q\overline{q}$) and neutral gluino decay ($\widetilde{g} \rightarrow \widetilde{\chi}_1^0 + q\overline{q}$) are equally set to 50%. The neutralino decays to $\gamma\widetilde{G}$ while the chargino decay is given by $\widetilde{\chi}_1^{\pm} \rightarrow W^{\pm} + \widetilde{\chi}_1^0$. Thus, the dominant final state is $W^{\pm}\gamma$ with a decay probability of 50%, while the $\gamma\gamma$ and $W^{\pm}W^{\mp}$ final state each make up 25% of the signal events.

6.2 General Gauge-Mediation Scenarios

Two full GGM scenarios based on the GGM framework (cf. Sec. 2.3.2) are used for the main part of the final interpretation. In contrast to the SMS scenarios, the different gaugino branching fractions are not rescaled by hand but come as a result of the model itself. While the SMS samples were already available for the individual analyses, the GGM samples are produced along with the combination. Thus, the model parameters used for the GGM sample production as well as the corresponding cross section calculations are described in more detail in the following sections.

6.2.1 Model Parameters and Sparticle Spectra

The GGM framework hase been used by theorists [38, 39] to develop both GGM scenarios. The model parameters, which correspond to the eight independent GGM parameters, and the sparticle masses, are available in SUSY Les Houches Accord (SLHA) files. These files are studied to get better insight into the GGM scenarios used for the interpretation of the combination.

The choice of the GGM input parameters for both scenarios can be seen in Tab. 6.1. The main difference between the scenarios corresponds to the pair of parameters, which are used to span the phase space. In case of the M1M2 scenario, the bino mass M_1 and the wino mass M_2, both defined at the messenger scale M_{mess}, are scanned while the gluino mass M_3 is fixed to 8 TeV. In the M1M3 scenario, the phase space is spanned by M_1 and M_3 while the wino mass is set between the bino and gluino mass. The Higgs mass parameter μ equals M_3 and $-M_2$ for the M1M2 and M1M3 scenario, respectively. This is mainly motivated by the range of the gaugino masses, which can be limited by the choice of μ. The remaining input parameters are kept unchanged between the two scenarios. For both scenarios, the variable parameters are scanned in 50 GeV steps. Each of the resulting parameter combinations is denoted as a signal point in the following.

Table 6.1: Definition of GGM input parameters for the two different GGM signal scenarios used in the final interpretation of the combination. All parameters are defined at the messenger scale $M_{mess} = 10^{15}$ GeV. The separation between up- and down-type squarks holds only for right-handed squarks.

Parameter	M1M2 Scenario	M1M3 Scenario
Bino Mass M_1	(250, 1500) GeV	(50, 1500) GeV
Wino Mass M_2	(250, 1500) GeV	$(M_1 + M_3)/2$
Gluino Mass M_3	8 TeV	(1000, 2500) GeV
Left-handed Squark Mass m_Q	10 TeV	10 TeV
Up-type Squark Mass m_U	10 TeV	10 TeV
Down-type Squark Mass m_D	8 TeV	8 TeV
Messenger Scale M_{mess}	10^{15} GeV	10^{15} GeV
Higgs mass[8] μ	8 TeV	$-M_2$

The physical masses of the sparticles are derived based on the GGM input parameters for both scenarios. Since the input parameters are defined at the messenger scale of 10^{15} GeV while the physical masses are usually interpreted at the EWK scale, renormalization group running has to be taken into account. This running results in a difference between the gaugino masses used as input parameters and the corresponding physical masses.
The resulting physical masses for the gauginos of main interest in the M1M2 scenario can be seen in Fig. 6.1. The most intuitive distribution corresponds to the chargino $\widetilde{\chi}_1^{\pm}$ mass, which scales with the wino mass M_2 and varies between 90 GeV and 1200 GeV. The scaling of both neutralino masses, in contrast, depends on the area of the phase space. This behavior is caused by one of the main features of the M1M2 scenario. For signal points with $M_1' > M_2'$, where the primed masses denote the gaugino masses exploited at the EWK scale, the lightest neutralino $\widetilde{\chi}_1^0$, which is the NLSP, is dominated by its wino component. Thus, in this area the physical mass of the NLSP scales with the wino mass M_2. While for signal points with $M_1' < M_2'$ the bino component is dominant and the NLSP mass scales with the bino mass M_1. In total, the NLSP mass varies between 90 GeV and 700 GeV. The statements on the NLSP mass can be simply reversed in case of the $\widetilde{\chi}_2^0$ as can be seen by comparing the two upper plots in Fig. 6.1. Here, the mass varies in the same range as the chargino mass. The effect of the dominant gaugino component for the NLSP is also visualized in the mass difference between NLSP and chargino (cf. lower right plot in Fig. 6.1). Since the chargino is dominated by its wino component, NLSP and chargino are almost mass degenerate for points with $M_1' > M_2'$ while the mass difference reaches up to 1100 GeV for the remaining signal points. Due to the constant M_3 value of 8 TeV the physical gluino mass is of the order of 5 TeV, which effectively suppresses contributions from gluinos in this GGM scenario.

[8] Here, the Higgs mass parameter of the GGM framework is defined and not the mass of the SM Higgs.

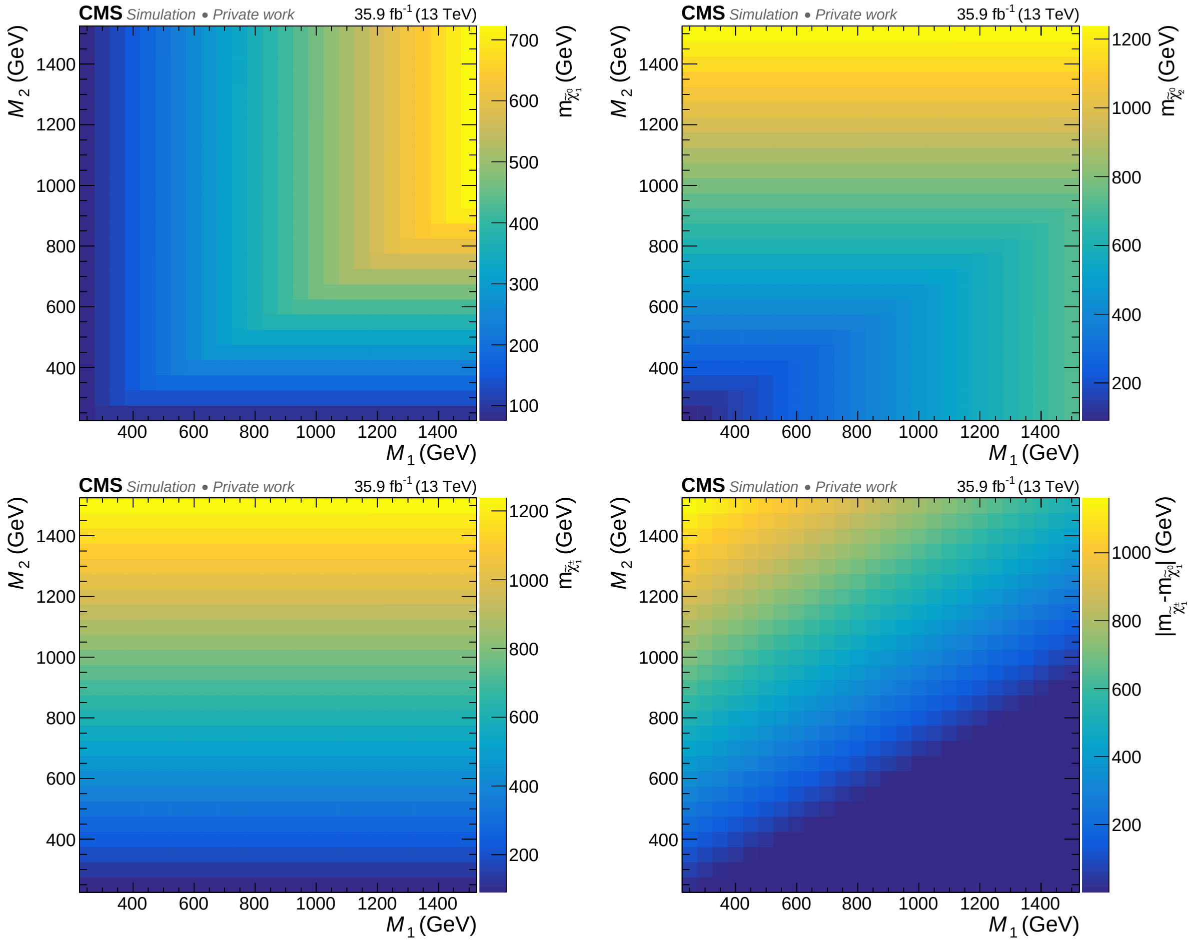

Figure 6.1: Physical masses in the M1M2 scenario of the lightest neutralino $\widetilde{\chi}_1^0$ corresponding to the NLSP (upper left), the next-to-lightest neutralino $\widetilde{\chi}_2^0$ (upper right) and the lightest chargino $\widetilde{\chi}_1^\pm$ (lower left). In addition, the mass difference between the lightest neutralino and the lightest chargino is shown (lower right).

The physical gaugino masses for the M1M3 scenario are shown in Fig. 6.2. Here, the physical masses scale more intuitively, since for all signal points $\widetilde{\chi}_1^0$ and $\widetilde{\chi}_2^0$ are bino- and wino-like, respectively. Thus, the NLSP mass varies with M_1 between 10 GeV and 750 GeV, while the $\widetilde{\chi}_2^0$ mass scales with M_2, which is set to $(M_1 + M_3)/2$, between 450 GeV and 1750 GeV. Another consequence is that for all signal points in the M1M3 scenario $\widetilde{\chi}_1^\pm$ and $\widetilde{\chi}_2^0$ are nearly mass degenerate. Due to the lower values of M_3 compared to the M1M2 scenario gluino masses down to 2350 GeV are possible. However, gluino pair production is still not accessible.

6.2.2 Sparticle Decays

Based on the sparticle spectra branching fractions for sparticle decays in both GGM scenarios are calculated using the SUSYHIT framework [82]. This framework combines two separate software packages, SDECAY [83] and HDECAY [84], to account for sparticle as well as Higgs decays, which are described by the two Higgs doublets (cf. Fig. 2.2).

The event signatures in both GGM scenarios are mainly determined by the decays of the lightest chargino $\widetilde{\chi}_1^\pm$ and the two lightest neutralinos $\widetilde{\chi}_1^0$ and $\widetilde{\chi}_2^0$. The main parameters driving the

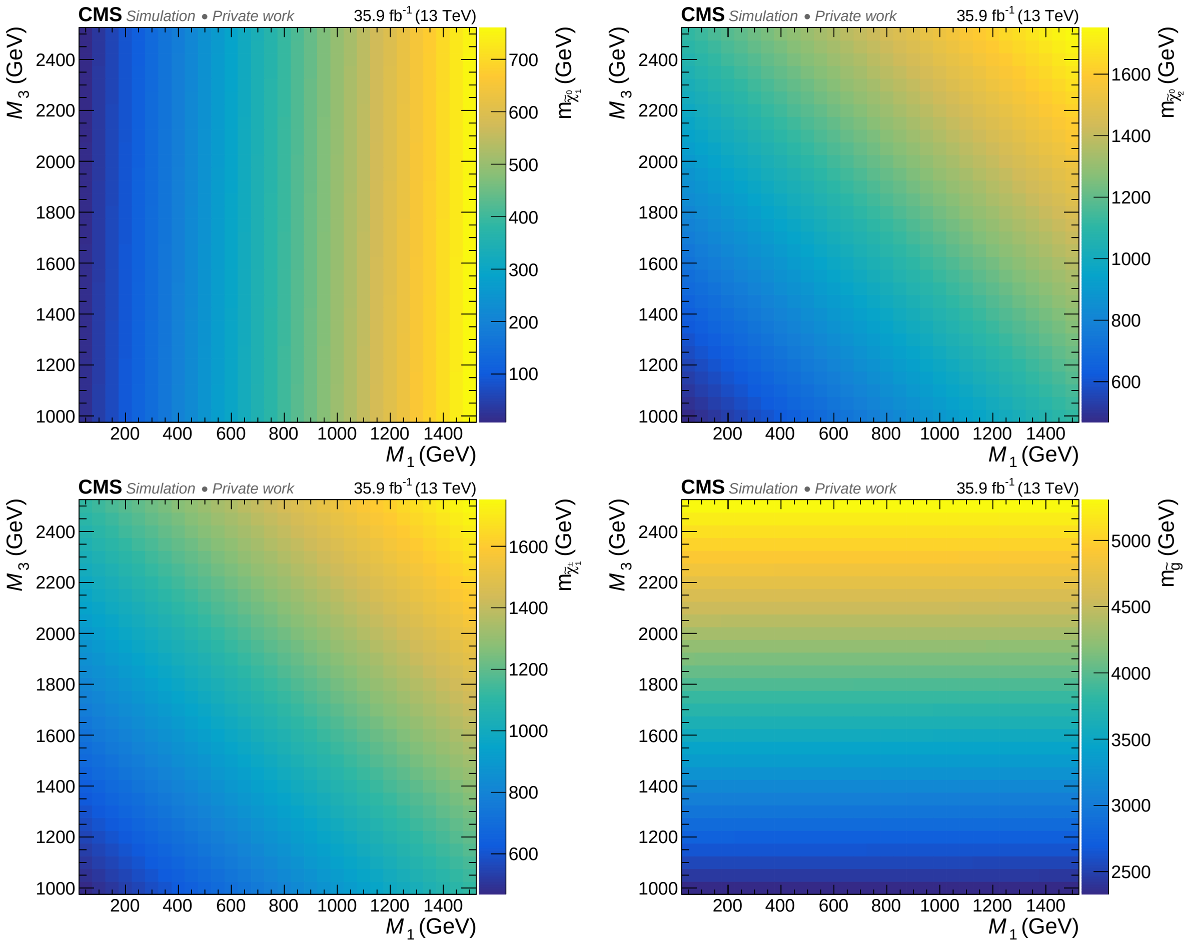

Figure 6.2: Physical masses in the M1M3 scenario of the lightest neutralino $\widetilde{\chi}_1^0$ corresponding to the NLSP (upper left), the next-to-lightest neutralino $\widetilde{\chi}_2^0$ (upper right), the lightest chargino $\widetilde{\chi}_1^\pm$ (lower left), and the gluino $\widetilde{g}$ (lower right).

branching fractions for these decays correspond to the mixing of the gauginos as well as the physical gaugino masses.

Since the lightest chargino $\widetilde{\chi}_1^\pm$ is wino-like for all signal points in both scenarios, its dominant decay is $\widetilde{\chi}_1^\pm \rightarrow \mathrm{W}^\pm + \widetilde{\chi}_1^0$. The only exception to this occurs in the M1M2 scenario if $\widetilde{\chi}_1^\pm$ and $\widetilde{\chi}_1^0$ are almost mass degenerate (cf. Fig. 6.1). In this case, the mass difference between the two gauginos is too small for an on-shell $\mathrm{W}^\pm$ to be produced. Thus, in this part of the phase space, the decay of the lightest chargino is dominated by $\widetilde{\chi}_1^\pm \rightarrow \mathrm{W}^\pm + \widetilde{\mathrm{G}}$.

The decay scheme of the $\widetilde{\chi}_2^0$, in contrast, differs between the two GGM scenarios. For the M1M3 scenario $\widetilde{\chi}_2^0$ and $\widetilde{\chi}_1^\pm$ are almost mass degenerate over the entire phase space (cf. Fig. 6.2). Thus, the charged decay ($\widetilde{\chi}_2^0 \rightarrow \mathrm{W}^\pm + \widetilde{\chi}_1^\pm$) is suppressed while the neutral decay ($\widetilde{\chi}_2^0 \rightarrow \mathrm{Z}/\mathrm{H} + \widetilde{\chi}_1^0$) is allowed with the decay including the Z boson dominating across the phase space. For the M1M2 scenario again the neutral decay dominates in the part of the phase space where $\widetilde{\chi}_2^0$ and $\widetilde{\chi}_1^\pm$ are almost mass degenerate. In this area, the decay including H is dominant due to a different $\widetilde{\chi}_2^0$ composition compared to the M1M3 scenario. For the phase space with $M_1' > M_2'$, the mass degeneracy between $\widetilde{\chi}_2^0$ and $\widetilde{\chi}_1^\pm$ does not hold (cf. Fig. 6.1). Thus, the charged decay dominates in this part of the phase space.

The most relevant gaugino decay is the decay of the lightest neutralino $\widetilde{\chi}_1^0$, which is the NLSP and the primary source of photons in both GGM scenarios. There are only two NLSP decays possible in both GGM scenarios. Bino-like NLSPs predominantly decay to $\gamma\widetilde{G}$, while the decay of wino-like NLSPs is predominantly given by $\widetilde{\chi}_1^0 \rightarrow Z{+}\widetilde{G}$. The branching fractions for these two decays are complementary. Due to the change of the NLSP composition in the M1M2 scenario the phase space with $M_1' < M_2'$ features a large branching fraction to $\gamma\widetilde{G}$. Signal points with $M_1' > M_2'$, in contrast, are characterized by decays to $Z\widetilde{G}$, as can be seen in Fig. 6.3. The only exception to this separation of the phase space corresponds to the area where the NLSP is wino-like, but its mass is smaller than m_Z. Here, again the decay to $\gamma\widetilde{G}$ is dominant. Since in the M1M3 scenario the NLSP is dominated by its bino component across all signal points, the lightest neutralino predominantly decays to a photon and a gravitino with rather small contributions from the decay to $Z\widetilde{G}$ (cf. Fig. 6.3).

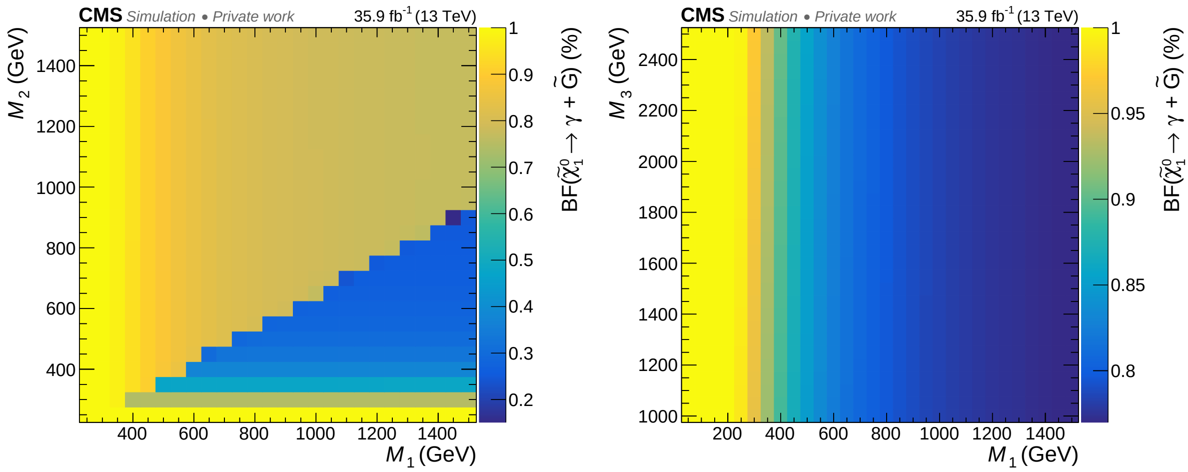

Figure 6.3: Branching fractions of the lightest neutralino $\widetilde{\chi}_1^0$, which corresponds to the NLSP, decaying to a photon and a gravitino for the M1M2 (left) and M1M3 (right) scenario. The branching fractions for $\widetilde{\chi}_1^0 \rightarrow Z{+}\widetilde{G}$ are complementary to the ones shown in the plots.

Due to the varying gaugino BFs across the phase spaces combined with multiple production channels, both GGM scenarios feature a large number of different final states. Since all four analyses, which contribute to the combination, are based on final states including at least one photon, the NLSP decay is the most relevant decay for the final interpretation. As can be seen in Fig. 6.3 most of the signal points in both scenarios can be related to a large BF for the NLSP decaying to $\gamma\widetilde{G}$. This does not hold for an area in the phase space of the M1M2 scenario, where the NLSP is wino-like and its mass exceeds m_Z. Here, the possibility of NLSP decays including a photon is of the order of 30% resulting in a higher amount of events without photons in the final state. The impact of the remaining two gauginos ($\widetilde{\chi}_2^0$ and $\widetilde{\chi}_1^\pm$) discussed above is mainly based on the observation that not every GGM event features two NLSPs and that additional $W^\pm$ can be produced. The latter feature significantly affects the Photon+Lepton analysis, since additional charged leptons can be present in the events due to $W^\pm$ decays.

6.2.3 Cross Section Calculation

In addition to the different decay branching fractions, production cross sections have to be derived based on the model parameters for both GGM scenarios. These cross sections differ from the ones used for the SMS scenarios due to varying gaugino compositions. Thus, a complete next-to-leading order (NLO) cross section calculation is performed using the PROSPINO 2.1 framework [85, 86].

The cross sections are derived for each signal point in both scenarios based on the corresponding model parameters given by the SLHA files. In addition to the model parameters, a parton density function (PDF), which describes the parton momentum distributions inside a proton, has to be used as an additional input to the framework. Since the resulting cross section strongly depends on the PDF choice, different PDFs are taken into account in the calculation and a PDF-dependent uncertainty is assigned to the final cross section following the PDF4LHC recommendations [87]. The recommended procedure is to perform the cross section calculation for each signal point 100 times while changing the input PDF for each iteration. Out of these 100 PDF replicas, one third each is based on CT14 [88], MMHT14 [89], and NNPDF3.0 [90] covering the uncertainty of the PDF itself. The final cross section is then given by the mean of the 100 results and the cross section uncertainty due to different PDF choices is derived by the corresponding standard deviation. The uncertainty on the strong coupling constant $\alpha_s = 0.1180 \pm 0.0015$ is taken into account by two additional iterations based on PDFs, which are derived with an α_s value shifted by its uncertainty. For the resulting α_s uncertainty on the final cross section half the difference between these two additional iterations is used. Since the PROSPINO 2.1 framework does not support the LHAPDF file format [91], which is needed to perform the calculation following the PDF4LHC recommendations, a small extension to the framework has been implemented. A validation of this extension can be found in Appx. 2. In addition to uncertainties based on the PDF and α_s choice, effects of different renormalization and factorization scales are studied. For the proper cross section calculations, these scales are set to the mass of the produced sparticles. To test the cross section dependency to different scale choices the nominal scales are shifted by a factor of two in both directions. The results based on the shifted scales are used to assign an additional scale uncertainty to the final cross section. The difference between the cross sections with a shifted scale and the initial results are taken as the scale uncertainty. Using this procedure a nominal cross section as well as corresponding uncertainties due to PDF, α_s, and scale variation are derived for each signal point. To ensure a complete coverage of the total cross section each possible production channel is tested for both signal scenarios. Due to the large sfermion, squark, and gluino masses, production channels including these sparticle classes do not contribute to the total cross section. While the remaining light gauginos, namely $\widetilde{\chi}_1^{\pm}$, $\widetilde{\chi}_2^0$, and $\widetilde{\chi}_1^0$, can be produced in the proton-proton collisions resulting in pure EWK production for both scenarios.

The total cross section and the combined relative uncertainty, covering PDF, α_s, and scale variations, for the M1M2 scenario can be seen in Fig. 6.4. Here, the dominant production channel changes across the phase space. Chargino pair ($\widetilde{\chi}_1^+\widetilde{\chi}_1^-$) production makes up around 30% of the total cross section for all signal points. For the phase space with $M_1' > M_2'$, the remaining 70% result from chargino-neutralino ($\widetilde{\chi}_1^{\pm}\widetilde{\chi}_1^0$) production, while for $M_1' < M_2'$, this fraction is covered by $\widetilde{\chi}_1^{\pm}\widetilde{\chi}_2^0$ production, including the next-to-lightest neutralino. Comparing the production channels with the gaugino masses (cf. Fig. 6.1) shows that the dominant contributions result from pair production for nearly mass degenerate gaugino pairs. The total cross sections decrease with increasing mass of the produced particles. The total uncertainty, in contrast, increases with increasing mass for most of the signal points. This behavior is caused by the PDF uncertainty, which dominates the total uncertainty for $M_2 > 500$ GeV. The total uncertainty for the remaining signal points is dominated by the scale uncertainty, which scales contrary to the PDF uncertainty. A complete overview of the individual uncertainties can be found in Appx. 3.

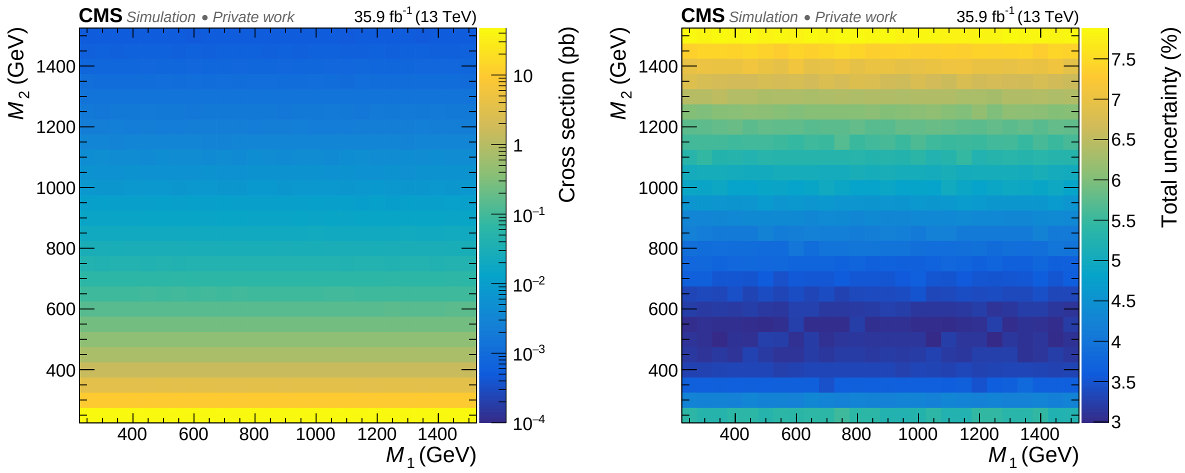

Figure 6.4: Total NLO cross sections derived for the M1M2 scenario (left). Combined relative cross section uncertainties including PDF, α_s, and scale uncertainty (right).

The results of the cross section calculation for the M1M3 scenario are shown in Fig. 6.5. In contrast to the M1M2 scenario, around 70% of the total cross section corresponds to $\widetilde{\chi}_1^\pm \widetilde{\chi}_2^0$ production across the whole phase space. The remaining 30% is covered by chargino pair production for all signal points. As already stated in case of the M1M2 scenario, the total cross section scales contrary to the mass of the produced particle while the opposite holds for the combined relative uncertainty. Here, the total uncertainty is dominated by the PDF uncertainty across the whole phase space (cf. Appx. 3).
Comparing the total cross sections for both GGM scenarios shows that in the M1M2 scenario larger cross sections can be achieved. The main reason for this is the lower mass of the produced particles in the M1M2 scenario compared to the M1M3 scenario (cf. Fig. 6.1 and 6.2).

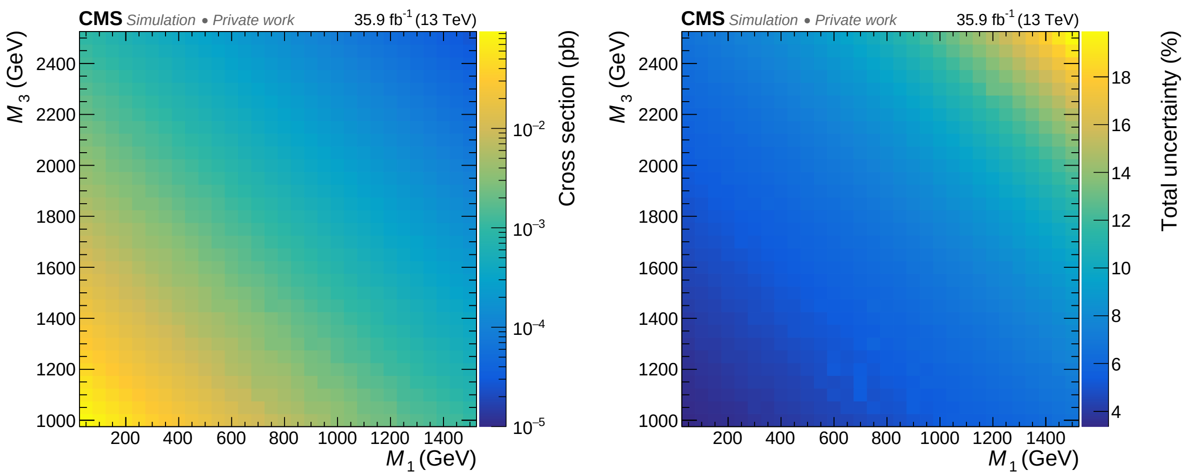

Figure 6.5: Total NLO cross sections derived for the M1M3 scenario (left). Combined relative cross section uncertainties including PDF, α_s, and scale uncertainty (right).

7 Event Selections and Background Estimation Methods

The four analyses, which are used in the combination, were all developed individually based on different final states including at least one photon. Thus, each of the searches is characterized by its own event selection resulting in a large phase space that can be covered by the combination. Due to the different final states, the background processes contributing to the individual search regions differ between the analyses. These contributions to the signal regions are estimated using different background estimation methods. To give an overview of the different event selections[9] as well as the different techniques used in the background estimations each of the four contributing analyses is briefly introduced in the following.

7.1 Photon+S_T^γ

The Photon+S_T^γ analysis [12] is designed to cover a wide range of different SUSY models mainly focusing on EWK scenarios. In this analysis, events are required to contain a high-energy photon and a large amount of missing transverse momentum p_T^{miss}. To maintain sensitivity to EWK as well as strong SUSY scenarios no additional jet requirements are considered.

The event selection is mainly defined by the presence of at least one high-energy photon with $p_T > 180$ GeV to match the requirements of the single photon trigger (cf. Sec. 5.1). The photon has to be reconstructed in the ECAL barrel ($|\eta| < 1.4442$). In addition, the events in the signal region are required to fulfill $p_T^{miss} > 300$ GeV. To avoid significant p_T^{miss} contributions from mismeasurements of jet energies, each jet with $p_T > 100$ GeV is required to exceed an angular distance to $\vec{p}_T^{miss}$ of $\Delta\phi(\vec{p}_T^{miss}, \mathrm{jet}) > 0.3$. Finally, the selected events have to match $M_T(\gamma_1, p_T^{miss}) > 300$ GeV, where γ_1 denotes the leading photon, to further improve the signal sensitivity while reducing SM background contributions. The final signal region is separated into four exclusive bins in S_T^γ, where all photons fulfilling $p_T > 15$ GeV and the object definitions in Sec. 5.3.1 are used in the calculation of S_T^γ. The corresponding bins are defined by the S_T^γ regions $600 - 800$, $800 - 1000$, $1000 - 1300$, and > 1300 GeV. In addition to the signal region, a control region (CR), used in one of the background estimation methods, is defined. Here, the p_T and $M_T(\gamma_1, p_T^{miss})$ requirements are both lowered to 100 GeV while excluding the signal region.

The main SM background contribution to the signal region arises from vector boson production with initial-state radiation of a photon (Vγ). The prediction of this SM process as well as of direct photon production in association with jets (γ+jets) is based on a χ^2-fit performed in the CR. Here, the distribution of $\Delta\phi(\vec{p}_T^{miss}, \text{nearest jet}/\gamma)$ is used to separate the two backgrounds. Using the simultaneous χ^2-fit between the MC prediction and the observed data in the CR, a scale factor for each of the two backgrounds is derived. Contributions from other SM backgrounds to the CR, which are small compared to Vγ and γ+jets, are kept constant in the fit. The corresponding post-fit distribution in the CR can be seen in Fig. 7.1. For the final background prediction, the MC prediction in the signal region is scaled by the scale factors derived in the CR.
An additional contribution to the signal region originates from electrons which are misidentified as photons (e $\rightarrow \gamma$). A misidentification rate $f_{e\rightarrow\gamma}$ measured in observed Z $\rightarrow e^+e^-$ events with the tag-and-probe method [92] is used to estimate this contribution. Since the derived rate depends on several kinematic properties of the photon, a 50% uncertainty is assigned to $f_{e\rightarrow\gamma}$.

[9] The event selections discussed in this chapter are based on the initial analyses while additional changes with respect to the combination strategy are discussed in Sec. 8.2.

To estimate the final contribution to the signal region an additional sample, which fulfills the event selection of the signal region but replaces the photon by an electron, is scaled by misidentification rate $f_{e\rightarrow\gamma}$. Smaller contributions to the signal region from $t\bar{t}(\gamma)$ and diboson processes are estimated based on simulation.
The combination of the different background prediction methods is tested in an exclusive validation region, which is defined by the same event selection as the signal region but instead requires $S_T^{\gamma} < 600$ GeV. As can be seen in the right plot of Fig. 7.1, a good agreement between the SM background prediction and the selected data is achieved.

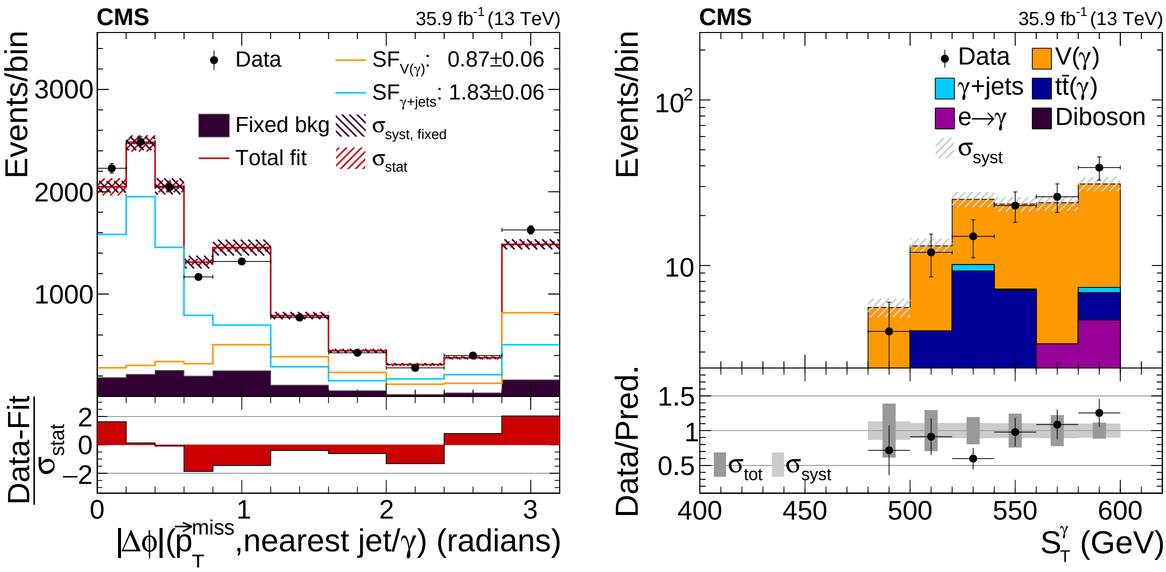

Figure 7.1: Left plot: Distribution of the angular distance between $\vec{p}_T^{\,miss}$ and the nearest jet or γ after the simultaneous χ^2-fit in the control region [12]. The scaled contributions from Vγ (orange) and γ+jets (blue) including scale factors as well as the total fit (red) and the fixed background (dark magenta) are shown. The statistical uncertainty (σ_{stat}) for the fit, the systematical uncertainty ($\sigma_{syst,\,fixed}$) for the fixed background, and the pull between data and fit can be seen. Right plot: Validation of the background prediction in the validation region [12]. In the ratio plot, the systematic (σ_{syst}) as well as the total uncertainty (σ_{tot}) of the background prediction are shown, while in S_T^{γ} distribution only the systematic uncertainty is given.

7.2 Photon+H_T^{γ}

In the Photon+H_T^{γ} analysis [13], the targeted final states are again characterized by a high-energy photon and a large amount of p_T^{miss}. Since this analysis focuses mainly on strong SUSY scenarios, events are required to fulfill an additional condition on the transverse event activity.

To fulfill the requirements of the trigger used in this analysis (cf. Sec. 5.1), the signal region is mainly defined by at least one high-energy photon with $p_T > 100$ GeV reconstructed in the ECAL barrel and an event activity of $H_T^{\gamma} > 700$ GeV. In addition, the missing transverse momentum p_T^{miss} of the selected events has to exceed 350 GeV. Due to possible misreconstruction of the photons in the barrel, $\vec{p}_T^{\,\gamma}$ and $\vec{p}_T^{\,miss}$ can be falsely aligned. Thus, events in the signal region are additionally required to match $|\Delta\phi(\pm\vec{p}_T^{\,miss}, \vec{p}_T^{\,\gamma})| > 0.3$ allowing for a reliable background prediction. In contrast to the Photon+S_T^γ search, the signal region is separated in two dimensions by splitting it into three p_T^{miss} ranges $(350 - 450,\ 450 - 600$ and ≥ 600 GeV) and two H_T^γ ranges $(700 - 2000$ and ≥ 2000 GeV). This results in a total of six search bins of which only the three bins with $H_T^\gamma > 2000$ GeV are used for the final combination (cf. Sec. 8.2). Two additional CRs, used for the background predictions, are defined. Events in the photon CR fulfill all requirements of the signal region but match $p_T^{miss} < 100$ GeV. The jet CR, in contrast, is only defined by the H_T^γ condition of the event selection.

One of the main background contributions for most parts of the signal region corresponds to QCD processes with jets, where the photon is directly produced (γ+jet) or reconstructed from a jet (multijet). Here, large amounts of p_T^{miss} can arise from mismeasurements of the jet energies (nongenuine p_T^{miss}). Since the p_T^{miss} shape of both processes is similar, estimates for these contributions are simultaneously derived by a data-driven method. The shape of the p_T^{miss} distribution in the jet CR is corrected to match the corresponding shape in the photon CR. This is achieved by applying a constant shift factor, which is derived by a χ^2 method in the region of $p_T^{miss} < 100$ GeV, to the p_T^{miss} values in the jet CR. To avoid contributions other than multijet events to the jet CR additional events are subtracted using simulation. Finally, the modified p_T^{miss} distribution of the jet CR, which is normalized to the p_T^{miss} distribution of the photon CR in the range of $p_T^{miss} < 100$ GeV, is used to estimate contributions from nongenuine p_T^{miss} to the signal region. Uncertainties on this background prediction arise mainly from the statistics in the photon CR and from uncertainties on the derived factor, which take, among others, its deviation from unity into account. This background prediction method is tested on simulated γ+jet and multijet events resulting in a good agreement between the direct simulation and the data-driven method applied to simulation (cf. Fig. 7.2).

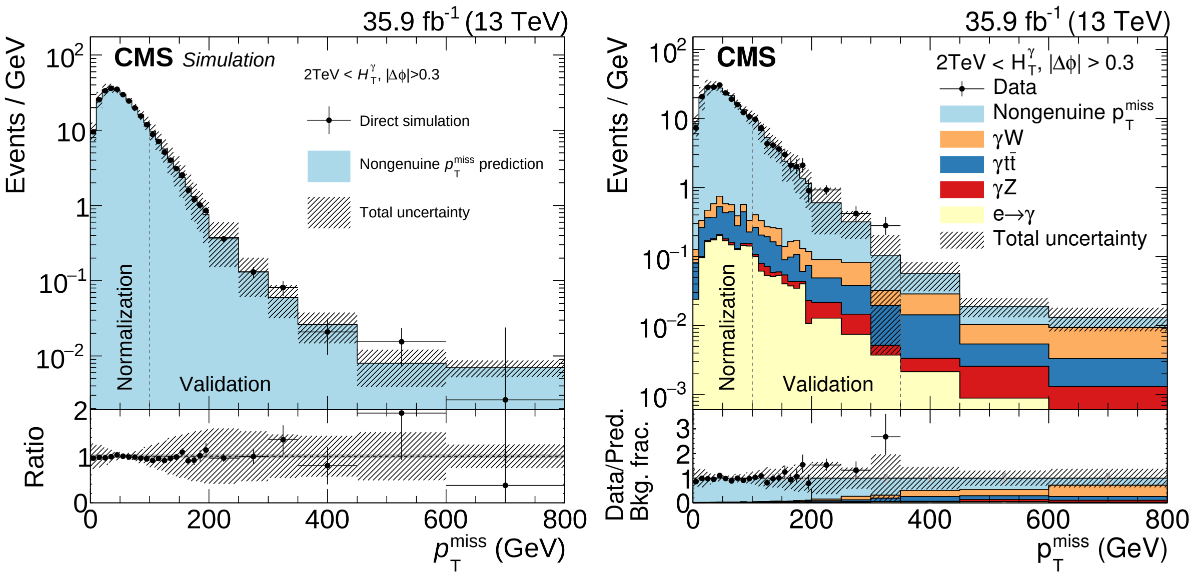

Figure 7.2: Left plot: Validation of the nongenuine p_T^{miss} prediction for $H_T^\gamma > 2000$ GeV using γ+jet and multijet simulation [13]. The blue bins correspond to the background prediction method applied to simulation, while the black dots are given by the direct simulation. The total uncertainty on the background is shown as the shaded area. Right plot: Validation of all background prediction methods for $H_T^\gamma > 2000$ GeV [13]. Since the validation of the background prediction is the primary goal, the data in the last three bins, which correspond to the signal region, is not shown.

Further contributions to the signal region from vector boson production with photon radiation (γW/γZ) and top quark pair production in association with a photon ($\gamma t\bar{t}$) are estimated using simulation. The impact of electrons being reconstructed as photons and thus contributing to the signal region is predicted by a scale factor using the same procedure as in the Photon+S_T^{γ} search.
The complete background prediction is validated in two different ways. First, the whole method is applied to events, where the signal photon is replaced by a photon reconstructed in the range of $1.6 < |\eta| < 2.5$, corresponding to a selection which is orthogonal to the signal region and shows negligible contributions from signal events. The corresponding plot can be found in [13]. Additionally, the p_T^{miss} range between the photon CR ($p_T^{miss} < 100$ GeV) and the signal region ($p_T^{miss} > 350$ GeV) is used to validate the background prediction (cf. Fig. 7.2). Both validations show a good agreement between background prediction and observed data.

7.3 Photon+Lepton

The Photon+Lepton analysis [14, 93], in contrast to the inclusive searches introduced before, targets rather specific final states. A charged lepton is required in addition to the photon and a high amount of missing transverse momentum. Due to the charged lepton requirement a lower photon-p_T threshold, compared to the inclusive searches, can be used allowing for a high signal efficiency even in phase space regions with low sparticle masses. As in the Photon+S_T^{γ} search additional criteria with respect to the hadronic activity are not applied, which maintains sensitivity for strong as well as EWK SUSY scenarios.

The signal region of this analysis is separated into eγ and $\mu\gamma$ channels considering the nature of the charged lepton. The lepton has to exceed a transverse momentum of 25 GeV. In case of the $\mu\gamma$ channels, muons are reconstructed in the range of $|\eta| < 2.4$ while electrons for the eγ channels have to be detected in $|\eta| < 2.5$ excluding the barrel-endcap transition region of $1.44 < |\eta| < 1.56$. If more than one charged lepton matches these criteria, the one with the highest p_T is selected. For the reconstructed photon, a moderate p_T threshold of 35 GeV and a $|\eta|$-value below 1.44 are required. To suppress photons created by final state radiation of the charged lepton, photons are rejected in the area of $\Delta R < 0.3$ around any reconstructed electron or muon. This criterion is tightened in case of the separation between the leading photon and the leading lepton. Here, the photon is rejected if the separation in ΔR falls below 0.8. To avoid high contributions from $Z \rightarrow e^+e^-$ events to the eγ channels, where one of the electrons is reconstructed as a photon, the invariant electron-photon mass has to exceed m_Z by at least 10 GeV. In addition to these criteria, the selected events have to fulfill $p_T^{miss} > 120$ GeV and $M_T(\ell, p_T^{miss}) > 100$ GeV. Based on the splitting into eγ and $\mu\gamma$ channels the signal region is further separated into bins of p_T^{miss} ($120-200$, $200-400$, >400 GeV), p_T^{γ} ($35-200$, >200 GeV), and H_T ($0-100$, $100-400$, >400 GeV)[10] resulting in a total of 36 exclusive search bins.

In the Photon+Lepton analysis contributions from SM processes to the signal region are classified into five different groups. In two of the groups, the photon is misidentified, while a real charged lepton can be reconstructed. As in the two searches introduced before there is the chance of electrons being misreconstructed as photons. Again contributions from this process are estimated using a misidentification factor applied to a control sample. The factor is derived in the region of $p_T^{miss} < 70$ GeV using the tag-and-probe method in data. In contrast to the inclusive

[10] Only jets, which are separated from the photon and the charged lepton by $\Delta R > 0.4$, contribute to the hadronic activity H_T.

searches, where contributions from this process are small, in the Photon+Lepton search, the method is performed for several bins in p_{T} and $|\eta|$ of the probed object as well as in the number of vertices in the selected events. This allows for a more accurate background prediction and thus, for a smaller uncertainty assigned to this contribution. The method is validated by comparing the background prediction to the simulation of the corresponding SM processes as can be seen for the $\mu\gamma$ channels in Fig. 7.3.
In addition to electrons, jets can be misidentified as photons. To predict contributions from this process a jet-to-photon misidentification factor $R = N_{had.\gamma}/N_{proxy}$ depending on the photon candidate p_{T} is derived in the region of $p_{\mathrm{T}}^{\mathrm{miss}} < 70$ GeV. The denominator is based on the number of jet proxies, which are given in a hadron control sample defined by inverting the cluster shape and isolation criteria of the photon identification (cf. Sec. 5.2). The nominator is derived by applying a hadron fraction factor to the selected photons resulting in an estimate on the number of photons, which are reconstructed from jets. This hadron fraction is calculated using a template fit to the isolation distribution separating pure photons and jet-to-photon misidentifications. To improve the method in the region of high-p_{T} candidates, which is limited by statistics, the p_{T} distribution of $N_{had.\gamma}$ and N_{proxy} is modeled with the sum of two exponential functions. The jet-to-photon misidentification factor R derived from these two functions is finally applied to the hadronic control sample in the area of $p_{\mathrm{T}}^{\mathrm{miss}} > 120$ GeV to predict the contributions of misidentified jets to the signal region.

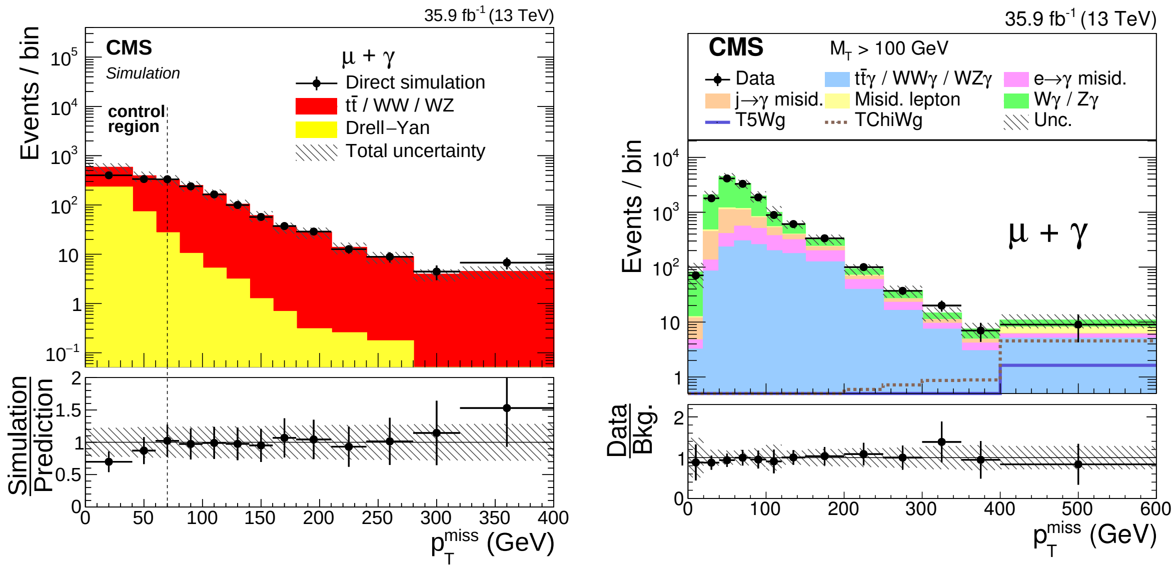

Figure 7.3: Left plot: Validation of the e $\to \gamma$ background prediction [14]. The misidentification rate is derived in a control region, which is dominated by Z $\to$ e^{+}e^{-} events (yellow). The final prediction (red) is compared to the prediction from direct simulation, which is shown as black points. The hatched areas correspond to the total uncertainty on the final prediction. Right plot: Validation of the complete background prediction in the region of $M_{\mathrm{T}}(\ell, p_{\mathrm{T}}^{\mathrm{miss}}) > 100$ GeV using the full $p_{\mathrm{T}}^{\mathrm{miss}}$ distribution without signal region binning [14]. For both plots, the $p_{\mathrm{T}}^{\mathrm{miss}}$ distribution of the $\mu\gamma$ channels is shown.

To predict the background contribution from vector boson production in association with a photon and from misidentified charged leptons a fit method similar to the method applied in the Photon+S_{T}^{γ} analysis is used. The shape of Vγ is modeled by simulation, while for the misidentified leptons a lepton CR with inverted isolation requirement of the lepton identification is

used. The fit is performed in the region of $40 < p_{\mathrm{T}}^{\mathrm{miss}} < 70$ GeV using the $\Delta\phi(\ell, \vec{p}_{\mathrm{T}}^{\mathrm{miss}})$ distribution resulting in a scale factor for each of the two background processes. The $p_{\mathrm{T}}^{\mathrm{miss}}$ region below 40 GeV is left out to reduce contributions from Zγ events. The final contributions to the signal region are derived by applying the scale factors to events in the lepton CR and simulation, which match $p_{\mathrm{T}}^{\mathrm{miss}} > 120$ GeV, for misidentified leptons and Vγ, respectively.
Additional contributions from diboson and top quark pair production in association with a photon are predicted based on simulation only. The final background prediction including all five different contributions is, for example, validated using the $p_{\mathrm{T}}^{\mathrm{miss}}$ distribution of the signal region without applying the signal region binning (cf. Fig. 7.3). A good agreement between the background prediction and the observed data is found.

7.4 Diphoton

The fourth analysis used in the combination is based on final states with two photons and a significant amount of missing transverse energy. The Diphoton analysis [15] mainly targets SUSY scenarios where the NLSP features a large bino component leading to a large probability for $\widetilde{\chi}_1^0 \rightarrow \gamma + \widetilde{\mathrm{G}}$ decays. As in the Photon+S_{T}^{γ} and Photon+Lepton searches, no additional requirement on the hadronic event activity is used to maintain high sensitivity to EWK and strong SUSY scenarios.

Motivated by the choice of the diphoton trigger the signal region of this analysis is mainly defined by the requirement of two photons with $p_{\mathrm{T}} > 40$ GeV, whose invariant mass has to exceed 105 GeV. To select events with a significant amount of $p_{\mathrm{T}}^{\mathrm{miss}}$, each event in the signal region has to fulfill $p_{\mathrm{T}}^{\mathrm{miss}} > 100$ GeV. An additional lepton veto is used to distinguish this analysis from other SUSY searches with photons and leptons. An event is rejected if an electron (muon) with $p_{\mathrm{T}} > 25$ GeV and $|\eta| < 2.5$ (2.4) can be reconstructed. The final signal region is separated into six exclusive bins using $p_{\mathrm{T}}^{\mathrm{miss}}$. The boundaries of these bins are given by $p_{\mathrm{T}}^{\mathrm{miss}} = 100$, 115, 130, 150, 185, and 250 GeV with the last bin including the region of $p_{\mathrm{T}}^{\mathrm{miss}} > 250$ GeV.

The background in the signal region of the Diphoton analysis is dominated by QCD events, where the photons can be directly produced or misreconstructed from jets. To predict the contributions from these processes a data-driven method is used. Two misidentified photons ("fakes"), which are defined by looser photon and neutral-hadron isolations and fail the shape requirement or the charge-hadron isolation (cf. Sec. 5.3.1), are selected to construct the ff control sample, which includes two fakes. To avoid a large number of signal events in this control sample, the fakes are required to satisfy $R_9 > 0.9$, where R_9 corresponds to the ratio of the energy in a 3x3 array cluster around the ECAL seed to the total energy of the reconstructed supercluster. To predict the contributions from QCD processes, the ratio of real diphoton events to ff events is modeled by an exponential function in the region of $p_{\mathrm{T}}^{\mathrm{miss}} < 100$ GeV, as shown in the left plot of Fig. 7.4. The final QCD prediction is derived by scaling the number of ff events, which fulfill the remaining requirements of the event selection, with the exponential function. To validate this procedure, the same method is used to predict the number of events with one photon and one fake (γf events). A good agreement between the prediction and the observed γf events, which are cleaned from W+jet events using simulation, is found [15].
Additional contributions to the signal region result from EWK events, which feature inherent $p_{\mathrm{T}}^{\mathrm{miss}}$ and electrons being reconstructed as photons. Similar to the searches introduced before, an electron-to-photon misidentification factor ($f_{\mathrm{e}\rightarrow\gamma}$), derived by the tag-and-probe method, is applied to an eγ control sample to predict this background contribution. To cover possible de-

pendencies between $f_{e \to \gamma}$ and various kinematic variables a 30% uncertainty is assigned to the misidentification factor.
Irreducible contributions from $Z\gamma\gamma$ events with the vector boson decaying to neutrinos are predicted by simulation. The final background prediction including QCD, EWK, and $Z\gamma\gamma$ contributions is validated using events, which match the event selection with exception to the p_T^{miss} requirement (cf. Fig. 7.4). A good agreement between background prediction and observed data is found.

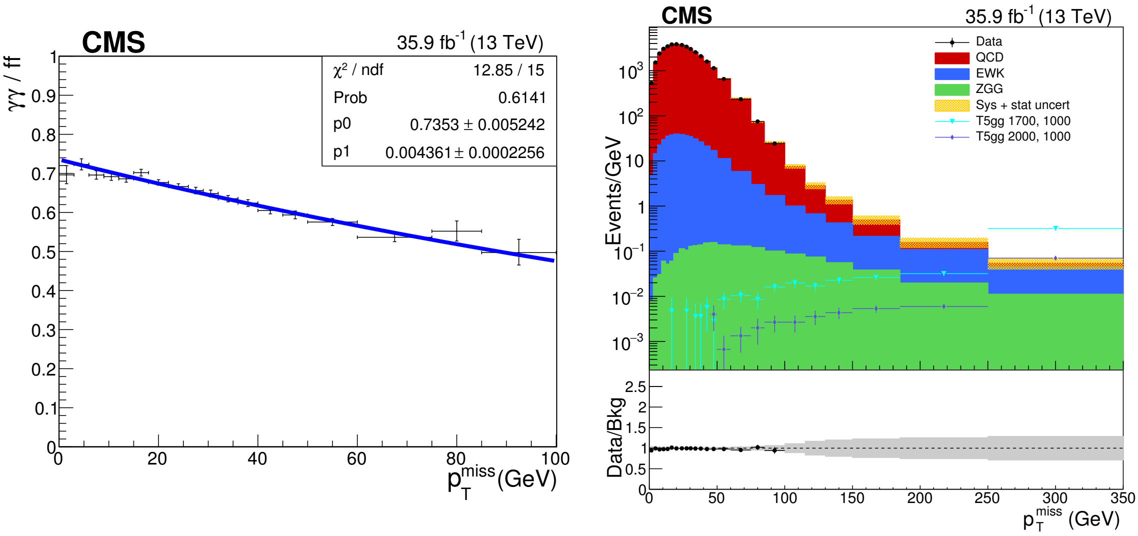

Figure 7.4: Left plot: Ratio of real diphoton events ($\gamma\gamma$) to events with two misreconstructed photons (ff) modeled by an exponential function $p_0 \cdot e^{-p_1 x}$ in the region of $p_T^{miss} < 100$ GeV [15]. Right plot: Final prediction for the whole p_T^{miss} spectrum [modified from [15]]. The shaded yellow areas in the upper part as well as the grey region in the ratio plot correspond to the total uncertainty on the background prediction. Since the validation of the background prediction is the primary goal, the data in the last six bins, which correspond to the signal region, is not shown.

8 Phase Space Overlaps

As the event selections of the four contributing analyses introduced in the previous chapter are not exclusive, phase space overlaps between the four signal regions have to be studied. Since a reliable combination can only be performed in the case of statistically exclusive signal regions, overlaps have to be removed by additional vetoes. To keep the rather specific signal regions of the Photon+Lepton and Diphoton analyses (specific searches) unchanged, this procedure is performed on the signal regions of the two inclusive searches (Photon+S_{T}^{γ} and Photon+H_{T}^{γ}). Different combination strategies are tested to find an ideal strategy, which results in improved limits across different SUSY scenarios. Since the additional criteria imposed to remove the overlap can lead to changes in the background predictions of the two inclusive searches the corresponding background validations are repeated.
These three steps, namely the study of phase space overlaps, the development of additional vetoes and combination strategies, as well as the background validations for the modified signal regions, are discussed in the following sections.

8.1 Overlap Studies

The four analyses used in the combination can be separated into two groups. The Photon+Lepton and Diphoton analyses target specialized signal regions due to additional object requirements besides the photon criteria (c.f. Sec. 7). Phase space overlaps between these two analyses should be naturally avoided by the lepton veto applied in the initial event selection of the Diphoton analysis. The remaining searches, Photon+S_{T}^{γ} and Photon+H_{T}^{γ}, in contrast, cover a wider phase space, since their signal regions are mainly defined by the existence of only one high-energy photon. Here, overlaps between these two searches as well as to the signal regions of the specific searches are expected to be found.

The phase space overlaps are studied using data events selected by the four analyses. The event selections of the three remaining searches are implemented in the frameworks of both inclusive analyses. Thus, each event selected by one of the inclusive searches can be tested with respect to the remaining three event selections. This procedure is validated on an event-by-event basis by comparing event lists of the four signal regions.
The resulting phase space overlaps in data are shown in Fig. 8.1. The search bins of both inclusive searches are dominated by events, which are not selected by any of the three remaining analyses. The ratio of exclusive events with respect to the total number of events per bin varies in the range of 67 to 88%. The only exceptions to this are the third and the fifth search bin of the Photon+H_{T}^{γ} analysis, where the exclusive events account for $\sim 50\%$ of the total yield. The smallest overlap to the signal regions of the inclusive searches is found in the event selection of the Diphoton analysis. Only one search bin in each of the inclusive searches is affected. This can be explained by the restrictive Diphoton event selection where only events in the highest $p_{\mathrm{T}}^{\mathrm{miss}}$-bin of the Diphoton signal region could be shared with the inclusive searches (c.f. Sec. 7.4).
The overlap to the Photon+Lepton analysis, in contrast, is spread over multiple search bins of the inclusive searches. For the Photon+S_{T}^{γ} signal region, an overlap in all four bins which corresponds to a fraction of 2 to 4% is found. For the Photon+H_{T}^{γ} search only the first four bins are affected with a contribution of 4 to 17% from events, which are likewise selected by the Photon+Lepton analysis.
The main overlap in both inclusive analyses is found among each other shown by the third row in each of the two plots (c.f. Fig. 8.1). The four bins of the Photon+S_{T}^{γ} search feature a contribution from Photon+H_{T}^{γ} events in the range of 9 to 31% with the third bin ($S_{\mathrm{T}}^{\gamma} = 1000 - 1300$ GeV)

corresponding to the largest overlap. These fractions are exceeded in case of the Photon+H_T^γ signal region. Here, events selected by both inclusive searches account for 24 to 50% of the yield in the six search bins. Due to the two inclusive event selections, which are both designed to cover a wide phase space, this comparatively large overlaps match the expectation.

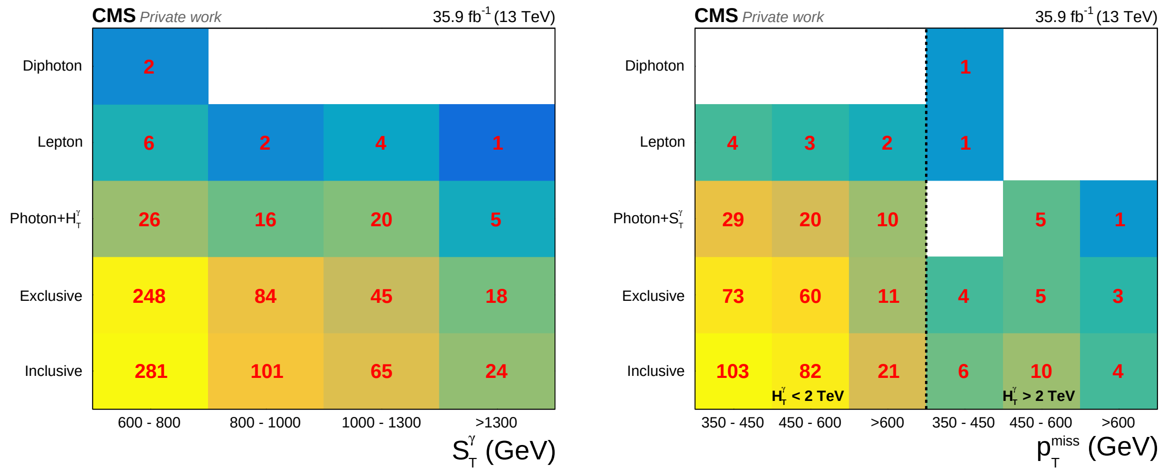

Figure 8.1: Phase space overlaps in data studied for the four search bins of the Photon+S_T^γ analysis (left) and the six search bins of the Photon+H_T^γ analysis (right). The latter six bins are separated into events with H_T^γ above and below 2 TeV. The first and the second row in both plots show the number of total events and the number of events which are exclusive for the corresponding analysis, respectively. The upper three rows account for the overlap to the remaining searches, which is non-exclusive between these three rows. The number of data events per bin is shown in red.

8.2 Veto and Combination Strategy

To perform a reliable combination of the four analyses the overlaps studied in the previous section have to be assigned to one of the four analyses by applying additional vetoes to the remaining searches. The veto strategies, which are developed in the following, are applied to the two inclusive searches. There is one main reason for modifying the signal regions of the inclusive searches instead of changing the event selection of the specific searches. The most significant overlap was found between the two inclusive searches while the event selection of the specific searches is exclusive by design. Thus, by developing a veto strategy, which only affects the inclusive searches, two of the four analyses can remain unchanged. Although the sensitivity of the inclusive searches might decrease due to the additional vetoes, in the combination the contributions from the two specific searches are expected to make up for this decrease.

The vetoes used for the combination are given by the criteria shown in Tab. 8.1. To remove the overlap between the inclusive searches and specific searches a lepton veto as well as a diphoton veto are applied to the event selection of the Photon+S_T^γ and the Photon+H_T^γ analyses. These two vetoes are designed to match the corresponding event selection of the Photon+Lepton and Diphoton searches (c.f. Sec. 7.3 and 7.4).
The overlap removal between the two inclusive searches is studied in detail to develop an optimized way of assigning the large phase space overlap between both inclusive searches. Three different vetoes are designed to study different combination strategies of the Photon+S_T^γ and the

Photon+H_T^γ analyses. For the first strategy (Strategy 1), the event selection of the Photon+S_T^γ search remains unchanged while an S_T^γ veto is applied to the Photon+H_T^γ analysis. With this strategy, the overlap is entirely assigned to the signal region of the Photon+S_T^γ analysis. In the second strategy (Strategy 2), the opposite approach is used. Here, the Photon+H_T^γ search remains unchanged while a full-H_T^γ veto is applied to the event selection of the Photon+S_T^γ analysis. The last strategy (Strategy 3), in contrast to the first two strategies, is designed to split the overlap in a natural way. Here, only the three search bins of the Photon+H_T^γ search with $H_T^\gamma > 2$ TeV (c.f. Sec. 7.2) are used in the combination while a high-H_T^γ veto is applied to the event selection of the Photon+S_T^γ search. This strategy is motivated by the features of the different SUSY scenarios targeted by the two inclusive searches. Since the Photon+H_T^γ analysis is designed for strong SUSY scenarios, which feature a large amount of hadronic activity in each event, the high-H_T^γ bins provide the largest sensitivity. The Photon+S_T^γ search, in contrast, mainly targets EWK scenarios with a low hadronic activity. Thus, applying the high-H_T^γ veto should not affect the sensitivity to EWK scenarios of the Photon+S_T^γ search to a large degree.

All vetoes designed for the combination are validated by comparing the resulting signal regions on an event-by-event basis in data. Thus, it is ensured that none of the observed events is included in more than one of the combined signal regions.
The validation of the three combination strategies regarding the background predictions, which could change due to the veto applications, can be found in Appx. 4. In case of the final strategy, which also includes both specific searches as well as the corresponding diphoton and lepton vetoes, the background validation is discussed in Sec. 8.3.

Table 8.1: Definition of vetoes used for different combination strategies. The diphoton as well as the lepton vetoes are applied to the event selection of both inclusive searches for the final combination. The full- and the high-H_T^γ vetoes are applied to the Photon+S_T^γ event selection for Strategy 2 and Strategy 3, respectively. The S_T^γ veto is applied to the Photon+H_T^γ event selection for Strategy 1. An event is only affected by the veto if all criteria of the corresponding veto are fulfilled. The number photons, which fulfill the photon identification with respect to the medium working point, are denoted as $N_{\gamma_{med}}$.

Veto	Criteria
Diphoton Veto	$N_{\gamma_{med}} \geq 2$ with $p_T^\gamma > 40$ GeV $m_{\gamma\gamma} > 105$ GeV
Lepton Veto	$N_\ell \geq 1$ with $p_T^\ell > 25$ GeV $M_T(\ell, p_T^{miss}) > 100$ GeV, $\lvert m_{\ell\gamma} - m_Z\rvert > 10$ GeV Leptons satisfying Photon+Lepton criteria
High-(full-) H_T^γ Veto	$H_T^\gamma > 2000$ (700) GeV, $p_T^{miss} > 350$ GeV $\lvert\Delta\phi(\pm\vec{p}_T^{miss}, \vec{p}_T^\gamma)\rvert > 0.3$
S_T^γ Veto	$p_T^\gamma > 180$ GeV, $S_T^\gamma > 600$ GeV $M_T(\gamma_1, p_T^{miss}) > 300$ GeV

The performance of the three different combination strategies introduced above is tested by combining only the two inclusive searches. The two specific searches, whose usage does not differ between the three strategies, as well as the lepton and diphoton vetoes are not included in these studies.
The combination itself as well as the limit setting, following the procedure introduced in Sec. 3, is performed using the HiggsCombine framework [43]. For the interpretation of the combined results, which include a total of ten search bins for the first two strategies and seven search bins in case of the third strategy, two unmodified SMS scenarios are used. To cover both possible SUSY production channels, namely EWK and strong production, which might behave differently for a given strategy, expected mass limits are set for the TChiNg and the T5Wg scenario (c.f. Sec. 6.1). To avoid possible bias caused by fluctuations in the observed data, only the expected limits are studied to test the performance of the different combination strategies.

The results for the three strategies with respect to both SMS scenarios can be seen in Fig. 8.2. Since the phase space of the strong T5Wg scenario is spanned by the gluino mass and the neutralino mass, which is degenerate to the chargino mass, the limit contour is displayed in a two dimensional way. Significant differences between the three strategies can be found. Strategy 2 and 3 coincide over a wide range and only differ for larger neutralino masses, where the limit resulting from Strategy 3 starts to exceed the others. The first strategy, in contrast, results in a weaker limit for most parts of the phase space but coincides with Strategy 3 close to the diagonal. This behavior can be explained by the design of the different strategies. The first strategy favors the Photon+S_T^γ search, which mainly targets signal events with a low amount of hadronic activity. Since these kinds of events are predominantly produced if the mass difference between gluino and neutralino is small, Strategy 1 results in a strong limit close to the diagonal.

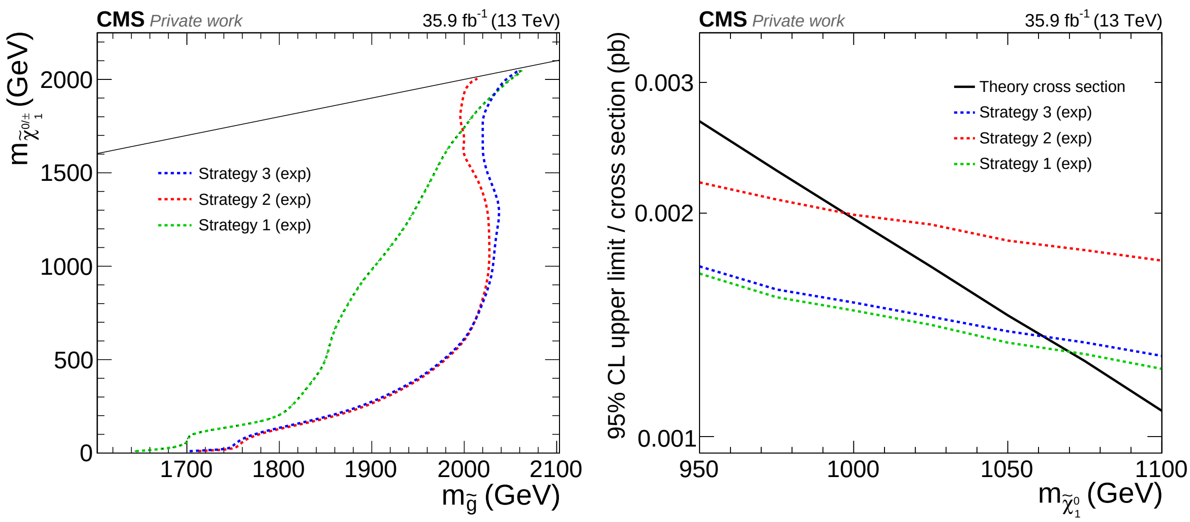

Figure 8.2: Left plot: Expected exclusion limit contours in the phase space of the T5Wg scenario, which is spanned by the gluino and neutralino mass. Right plot: Expected upper cross section limits in the phase space of the TChiNg scenario, which is spanned by the mass of the neutralino. The solid black line corresponds to the theoretical cross section of the given signal scenario. The results of all three combination strategies are shown in both plots, with Strategy 1 (green) and Strategy 2 (red) favoring the Photon+S_T^γ and Photon+H_T^γ analyses, respectively. In Strategy 3 (blue) the overlap is split between these two inclusive. In these studies the two specific searches as well as the lepton and diphoton vetoes are neglected.

The second strategy favors the Photon+H_T^γ analysis, which targets events with a large hadronic activity. For most parts of the signal region, such events are dominant due to the large mass difference between gluino and neutralino, resulting in the limit contour of Strategy 2. The third strategy is designed to keep the strengths of both inclusive analyses by splitting the overlap. The resulting limit verifies the success of this approach since this limit not only envelopes the other two limits but exceeds them at neutralino masses of the order of 1500 GeV.
The phase space of the EWK TChiNg scenario, in contrast, is only spanned by the mass of the lightest neutralino. Thus, cross section limits for all three strategies as well as the theoretical cross section are shown in Fig. 8.2. Here, the first and the third strategy, whose difference is small, exceed Strategy 2 across the whole phase space. This is caused by the design of Strategy 2, which favors the Photon+H_T^γ search. Since electroweakly produced signal events usually feature only a small hadronic event activity, the second strategy results in a weaker limit. Strategy 3 almost coincides with Strategy 1, which favors the Photon+S_T^γ search.

Based on the study of the three different combination strategies, it can be stated that the first two strategies, which are designed to assign the overlap to only one of the inclusive searches, lead to a performance, which strongly depends on the nature of the tested scenario. The third strategy, in contrast, is developed to keep the strengths of both inclusive analyses. Here, good performance across both signal scenarios is found. In the final combination, the Photon+S_T^γ and Photon+H_T^γ analyses are combined using Strategy 3. In addition, the two specific searches, which were neglected for the performance studies of the different combination strategies, associated with the lepton and diphoton vetoes are included in the final combination.

8.3 Validation of Background Estimations

For the final combination of all four analyses, multiple vetoes are applied to the signal selection of the two inclusive searches. To remove the overlap between each of the inclusive to the specific searches, lepton and diphoton vetoes are applied to the signal region of Photon+S_T^γ and Photon+H_T^γ. In addition, overlap removal according to Strategy 3 is applied. Due to these additional vetoes the compositions of both inclusive search regions change. To include these changes into the background predictions, the vetoes are applied to all additional regions used for the different background estimation methods (c.f. Sec.7.1 and 7.2). Since this might change the performance of the different methods, the main background validations for the two inclusive searches are reproduced for the modified event selections to ensure that the background predictions are still reliable.

In case of the Photon+S_T^γ search the lepton, the diphoton, and the high-H_T^γ vetoes, defined by Tab. 8.1, are applied to the event selection. To validate the full background prediction for this modified selection the validation region, which is given by the same selection as the signal region but requires $S_T^\gamma < 600$ GeV, is used. To take the changes of the signal region into account, the same vetoes are applied to the validation region. The result of this validation can be seen in Fig. 8.3. The S_T^γ distribution as well as the p_T spectrum of the leading photon in the validation region are shown. For both distributions, good agreement between the observed data and the predicted background yields is achieved. Thus, it can be concluded that the background prediction methods used by the Photon+S_T^γ analysis still provide reliable predictions after applying the modified event selection.

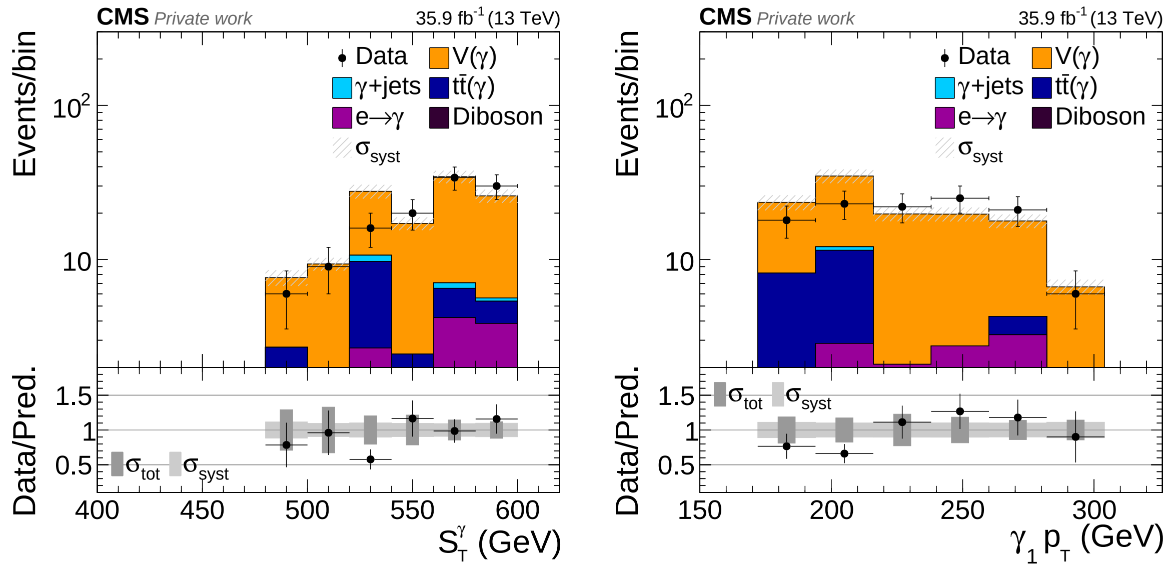

Figure 8.3: Validation of the background prediction in the validation region ($S_T^\gamma < 600$ GeV) with lepton, diphoton, and full-H_T^γ vetoes applied. The left plot shows to the S_T^γ spectrum while in the right plot the p_T distribution of the leading photon is shown. The systematic uncertainty on the background prediction (σ_{syst}) is shown in both parts of the plots while the total background uncertainty (σ_{tot}) can additionally be seen in the ratio parts.

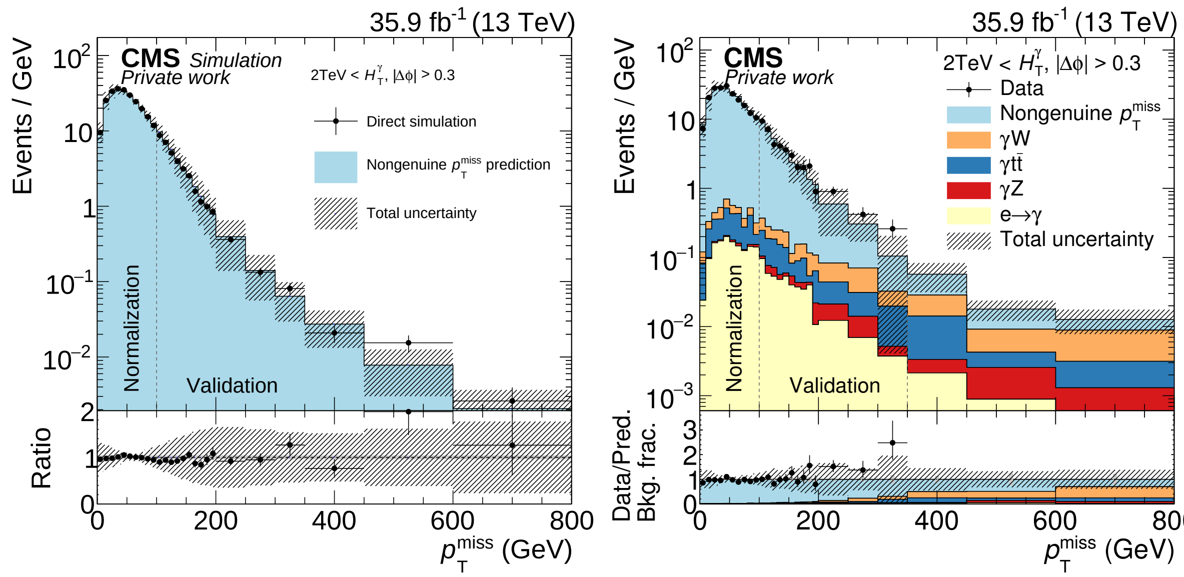

Figure 8.4: Left plot: Validation of the nongenuine p_T^{miss} background prediction for the high-H_T^γ region with lepton and diphoton vetoes applied using simulation. The blue bins correspond to the background prediction performed on simulation. The black dots are given by the direct simulation. The total uncertainty on the background is shown as the shaded area. Right plot: Validation of all background prediction methods combined for the high-H_T^γ region with the lepton and diphoton vetoes applied. Since the validation of the background prediction is the primary goal, the data in the last three bins, which correspond to the signal region, is not shown.

Following the combination strategy only the three high-H_{T}^{γ} bins of the Photon+H_{T}^{γ} search, which fulfill $H_{\mathrm{T}}^{\gamma} > 2$ TeV, contribute. Thus, the effects of the lepton and diphoton vetoes on the background prediction for this part of the initial Photon+H_{T}^{γ} search region have to be studied. As in the procedure for the Photon+S_{T}^{γ} search, the corresponding background validations are reproduced with respect to the additional vetoes. The dominant nongenuine $p_{\mathrm{T}}^{\mathrm{miss}}$ background is validated comparing direct simulation and the data-driven method performed on simulation (c.f. Sec. 7.2). The result of this validation, which is performed with the additional vetoes applied, is shown in the left plot of Fig. 8.4. A good agreement between direct simulation and the nongenuine $p_{\mathrm{T}}^{\mathrm{miss}}$ background prediction is observed. In addition to the validation of the main background, the combination of all background predictions is tested in data using the validation region $100 < p_{\mathrm{T}}^{\mathrm{miss}} < 350$ GeV. Again good agreement between the observed data and the background prediction with respect to the uncertainties is found. Both plots can be compared to the initial background validations shown in Fig. 7.2, which do not include the vetoes. With both background validations showing a good agreement, it can be stated that the methods of the Photon+H_{T}^{γ} analysis lead to reliable background estimates also for the modified event selection.

The reproduction of the main background validations for the two inclusive searches with respect the modified event selections shows that the background estimation methods for both searches still provide reliable background predictions. Since the Photon+Lepton and the Diphoton analyses remain unchanged in the final combination, no additional background validations for these two searches have to be performed.

9 Uncertainty Correlations

The estimated background yields as well as the signal predictions are subject to multiple uncertainties. These uncertainties are calculated individually by each of the corresponding analyses[11]. As introduced in Sec. 3, nuisance parameters are used in the limit setting procedure to account for different uncertainties. In contrast to the interpretation of a single analysis, additional correlations between the uncertainties used in the contributing searches have to be taken into account in the combination. The neglect of such correlations could spoil the limit setting, which would lead to an inaccurate interpretation of the combined results. In the following, the uncertainties on the estimated backgrounds as well as on the signal predictions used by the analyses are discussed regarding correlations. Following the procedure of the HiggsCombine framework [43], the uncertainties are assumed to be either fully correlated or fully uncorrelated between analyses.

9.1 Background Uncertainties

Regarding uncertainties, considered in the background prediction methods of the searches, two different aspects are discussed. On the one hand, correlations can be based on statistical overlaps between the multiple data control regions used for the background prediction methods (cf. Sec. 7). On the other hand, similarities between the methods could justify correlations between the corresponding uncertainties.

To study the overlap between the data control regions used by the different analyses, selected events are compared on an event-by-event basis. To adapt the combination strategy introduced in the previous chapter, the corresponding vetoes are applied to the control regions of the two inclusive searches. The results can be seen in Tab. 9.1. Most of the 15 possible combinations, based on a total of six control regions, do not show any overlapping events. The highest number of events selected by two of the control region definitions is found between the jet control region of the Photon+H_T^γ analysis and the ff control sample of the Diphoton search. However, this overlap only corresponds to an overlapping fraction way below one per mill, which can be neglected. The highest overlapping fraction with respect to the total yield is found for the lepton control region in the Photon+Lepton search. Here, the study shows an overlap of around 5% with respect to the Photon+S_T^γ control region.

In addition to the study of the control region overlaps, similarities between the different background prediction methods are studied. While comparing the different methods, described in Sec. 7, the most apparent similarities can be found in the method used to predict the contributions from electrons being reconstructed as photons. In all four searches, variations of the tag-and-probe method [92] are used to estimate the background yields given by this process. Thus, the corresponding uncertainties, which are assigned by the analyses, are assumed to be fully correlated between all four searches.

In each of the four analyses mainly subdominant background contributions are estimated based on plain simulation. These backgrounds are given by diboson and top quark pair processes in three of the searches while in the Diphoton analysis the $\mathrm{Z}\gamma\gamma$ background is estimated by this method. Since the simulated samples used for these predictions are produced similarly (cf. Sec. 5.2) and do coincide in case of the diboson and top quark pair background estimations, the corresponding uncertainties are assumed to be fully correlated between the analyses. Motivated by the small contributions from these processes, a conservative uncertainty estimate is preferred against a detailed calculation by each of the four analyses. To use a similar estimate

[11] A detailed description of the different uncertainties can be found in the references of the individual analyses.

Table 9.1: Overlaps between the control regions used by the individual analyses modified by the additional vetoes. The first and the last row correspond to the Photon+S_T^γ and Diphoton control regions, respectively. For the Photon+H_T^γ search the photon (γ) as well as the jet control region are studied. In the case of the Photon+Lepton analysis, the lepton (ℓ) and the hadron (jet) control sample are taken into account. The diagonal denotes the total event yield of the corresponding control regions.

	S_T^γ	H_T^γ (γ)	H_T^γ (jet)	Lepton (ℓ)	Lepton (jet)	Diphoton
S_T^γ	12568	-	-	9	2	-
H_T^γ (γ)	-	107260	-	-	-	-
H_T^γ (jet)	-	-	8894300	-	1	36
Lepton (ℓ)	9	-	-	184	-	-
Lepton (jet)	2	-	1	-	1274	-
Diphoton	-	-	36	-	-	210554

across all searches, the uncertainty used in the Photon+S_T^γ analysis is changed from 30% to 50%, matching the description used in the remaining searches.
The last prediction methods, which feature similarities between at least two of the contributing analyses, correspond to the fit procedure used in the Photon+S_T^γ and Photon+Lepton searches. In the case of the Photon+S_T^γ search, scale factors for the Vγ and γ+jets prediction are derived by performing a fit in an angular distribution, which separates the shape of both background contributions (cf. Sec. 7.1). In the Photon+Lepton search, a similar procedure is used to derive scale factors for the Vγ processes and contributions from misidentified charged leptons (cf. Sec. 7.3). In addition, the control regions used in these predictions show an overlap of 9 events, which make up for 5% of the lepton control region. To cover these similarities as well as the overlap the uncertainties regarding the fitting procedure are assumed to be fully correlated between the Photon+S_T^γ search and the Photon+Lepton search.

9.2 Signal Uncertainties

In addition to the uncertainties assigned to the background yields, nuisance parameters are also assigned to the signal prediction, to take uncertainties based on the signal simulation into account. Here, additional uncertainties are assigned to the initial set of uncertainties used by the different analyses. This step is mainly motivated by the fact that the same signal simulations are used by all analyses, but different sets of signal uncertainties are taken into account. Thus, by assigning a uniform set of signal uncertainties to each analysis, a consistent description across the combination can be ensured. In addition, all uncertainties assigned to the signal predictions are assumed to be fully correlated between the four searches. The only exception to this is given by the statistical uncertainties of the signal yields. As discussed before, the signal regions used in the combination are exclusive due to the removal of the overlaps discussed in Sec. 8.2. Thus, each of the simulated events used for the signal prediction is only selected by one of the four analyses.

Since the assignment of a uniform set of signal uncertainties can result in small changes compared to the description of uncertainties used by initial analyses, the set of systematic signal uncertainties will be briefly introduced in the following:

Fast Simulation of $p_{\mathrm{T}}^{\mathrm{miss}}$: In the procedure of signal simulation the detector simulation using GEANT4 [64] is replaced by the FastSim framework [72] to save computing time. This replacement can affect the simulated reconstruction of particles in the signal events. Since the missing transverse momentum is based on all reconstructed particles, changes with respect to the reconstructed $p_{\mathrm{T}}^{\mathrm{miss}}$ cannot be excluded. Comparisons between FastSim and GEANT4 yield large changes in events where $p_{\mathrm{T}}^{\mathrm{miss}}$ is caused by mismeasurements. To reduces these changes, the signal selection of all four analyses is performed twice, once using the reconstructed and once using the generated missing transverse momenta. The average yield of both iterations is used as the final yield while half the difference between the iterations is assigned as uncertainty to the signal yield.

Initial State Radiation: To improve the modeling of initial state radiation (ISR), which affects the total transverse momentum of the SUSY particle system (p_{T}^{ISR}), a reweighting of the p_{T}^{ISR} distribution in EWK SMS scenarios is performed. This reweighting procedure is based on studies of the transverse momentum of Z events [94]. To account for any systematic effects, the difference to the result based on the unweighted distribution is assigned as an ISR uncertainty to the signal prediction.

Photon Scale Factors: Since the event selections of all contributing analyses are mainly based on the reconstruction of at least one photon, differences between the photon reconstruction efficiency in data and simulation have to be taken into account. Here, studies comparing data and simulation with respect to the photon reconstruction were performed by each of the analyses. These studies result in an additional uncertainty on the signal yield between 2 and 5%.

Pileup: To take differences between data and simulation with respect to the number of simultaneous interactions into account, an additional pileup uncertainty is assigned to the signal yield. This uncertainty is derived by splitting the simulated signal events into a low-pileup and a high-pileup category and performing the signal prediction for each of the categories individually. The difference between the signal yields derived from the two categories is assigned as the pileup uncertainty to the signal prediction.

Jet Energy Scale: The energy scale of reconstructed jets is corrected to account for effects of pileup and of non-uniform detector responses [95]. This correction propagates to observables like the missing transverse momentum, which can change the final signal yield. To account for these changes the signal prediction is additionally performed using a jet energy scale, which is shifted upward and downward by its uncertainty. Half the difference between the signal yields from these two additional iterations is assigned as a jet energy scale uncertainty to the signal prediction.

Measured Luminosity: The simulated signal events are scaled to match the measured luminosity of the observed data. Since the luminosity measurement has an uncertainty of 2.5% [96], the same value is assigned as luminosity uncertainty to the final signal prediction.

All of these uncertainties, except for the first two uncertainties, are also assigned to parts of the background predictions performed by the individual analyses. Thus, the correlation of these signal uncertainties not only affect the signal predictions but can also lead to minor effects on the background predictions.

10 Results and Interpretations

The different steps towards a reliable combination of the four analyses, including overlap studies, additional background validations, and studies regarding the uncertainty correlations between different searches, are discussed in the previous sections. In this section, the results of the final combination are presented. The observed yields are compared to the background prediction for each search bin of the combination. In addition, SMS as well as GGM scenarios are used to interpret the final results and to set upper limits on multiple signal parameters following the method discussed in Sec. 3.

10.1 Results

The final results used in the combination are based on the combination strategy developed in Sec. 8.2. In this strategy, the two specific searches, Photon+Lepton and Diphoton, are kept unchanged while additional vetoes are applied to the event selection of the two inclusive searches, Photon+S_T^γ and Photon+H_T^γ. A lepton veto as well as a diphoton veto are added to the selection of both inclusive searches. In addition, the signal region of the Photon+S_T^γ analysis is modified by a high-H_T^γ veto while only the three Photon+H_T^γ search bins, which fulfill $H_\mathrm{T}^\gamma > 2$ TeV, are used. Due to this strategy, the final results include a total of 49 exclusive search bins. Four out of these 49 bins are based on the Photon+S_T^γ analysis, where the signal region is divided by the S_T^γ variable. The Photon+H_T^γ search accounts for three search bins, which are divided with respect to $p_\mathrm{T}^\mathrm{miss}$. The largest number of the search bins used in the combination is contributed by the Photon+Lepton analysis. Here, the search region is divided into eγ and $\mu\gamma$ channels based on the nature of the reconstructed charged lepton. These channels are further divided by $p_\mathrm{T}^\mathrm{miss}$, the total hadronic activity H_T, and the transverse momentum of the leading photon p_T^γ resulting in a total of 36 bins. The remaining six search bins are contributed by the Diphoton search, where the signal region is only divided by $p_\mathrm{T}^\mathrm{miss}$.

The comparison between the observed yield and the background prediction for all 49 search bins is shown in Fig. 10.1. In case of the Photon+Lepton and Diphoton searches these comparisons correspond to the published results, while the yields of the Photon+S_T^γ and Photon+H_T^γ analyses are based on the modified event selections, which ensure exclusive signal regions. For most of the 49 search bins good agreement between the observed events and the standard model prediction is found. One significant deviation between the observed yield and the background prediction is found in the second search bin of the Photon+H_T^γ analysis. Comparing this deviation to the published result of this search [13] it is found, that the excess is not caused by the additional vetoes but is a feature of the initial analysis.
Additional deviations can be found in the search region of the Photon+Lepton analysis. The fourth and the last search bin in the eγ channels as well as the tenth bin in the $\mu\gamma$ channels show a small excess in the observed data compared to the background prediction. Since in case of the Photon+Lepton search the event selection is kept unchanged, these deviations are not caused by the combination strategy [14].
The same argumentation holds for the last search bin of the Diphoton search, which also shows an excess. While the deviations in case of the Photon+H_T^γ and Photon+Lepton analyses are found in search bins, which feature a rather low sensitivity to the shown GGM signal point, the excess in the last Diphoton search bin coincides with a rather high sensitivity affecting the interpretations discussed in the following sections.

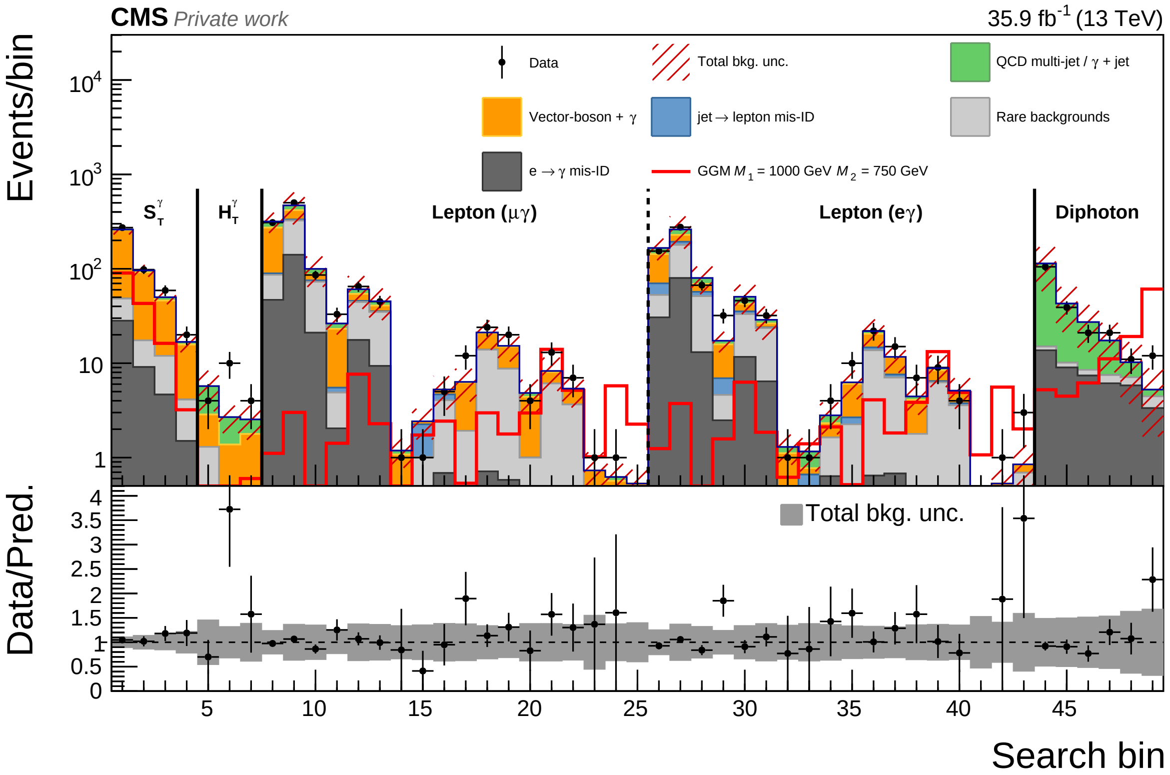

Figure 10.1: Comparison between background prediction and observed yields for all 49 search bins used in the combination. Bins 8 to 25 correspond to the $\mu\gamma$ channels of the Photon+Lepton search, while bins 26 to 43 cover the eγ channels. The six different background contributions (colored areas) as well as the total uncertainties (red shaded area) are shown in the upper part of the plot. In addition, one example signal point for the M1M2 scenario, which corresponds to a bino mass of 1000 GeV and a wino mass of 750 GeV, both defined at the messenger scale, is overlaid (red line). The lower part of the plot shows the ratio between background prediction and observation, including the total background uncertainty.

The largest two excesses discussed above, which both correspond to deviations of the order of two standard deviations from the background predictions, are expected. Since the combination includes a total of 49 bins, in around two to three bins a deviation of this order should be found. The majority of the search bins show a good agreement between the observation and the standard model prediction. Thus, no evidence for physics beyond the standard model is found, and the results of the combination are used to set upper exclusion limits with respect to several SUSY scenarios.

10.2 Limits on General Gauge-Mediation Scenarios

The results of the combination are used to set limits on two full GGM scenarios. The features of both scenarios as well as the corresponding cross section calculations are explicitly discussed in Sec. 6.2. Especially in case of the interpretation based on the M1M2 scenario, these features are essential to discuss the resulting limits, which are more complex compared to the remaining interpretations.

The interpretation of the combination in the M1M2 scenario at 95% confidence level (CL) is shown in the left plot of Fig. 10.2. Based on the expected limit all signal points below a wino mass M_2, defined at the messenger scale, of around 1250 to 1300 GeV can be excluded. The only exception to this is given by an area, where the wino mass is of the order of 850 GeV and the bino mass M_1 exceeds 1350 GeV. About the same area is likewise not excluded by the observed limit, which, in contrast to the expected limit, rules out signal points with wino masses below 1050 to 1100 GeV resulting in a discrepancy between expected and observed limit at high wino masses.

The interpretation based on the M1M3 scenario is shown in the right plot of Fig. 10.2. Based on the expected limit signal points with a gluino mass M_3 up to 2350 GeV and a bino mass M_1 up to 1450 GeV can be excluded. In case of the observed limit, these upper bounds are lowered by around 400 GeV and 500 GeV for the gluino and bino mass, respectively. This results in a visible discrepancy between the observed and expected limit, similar to the interpretation of the M1M2 scenario. These discrepancies will be discussed at a later point.

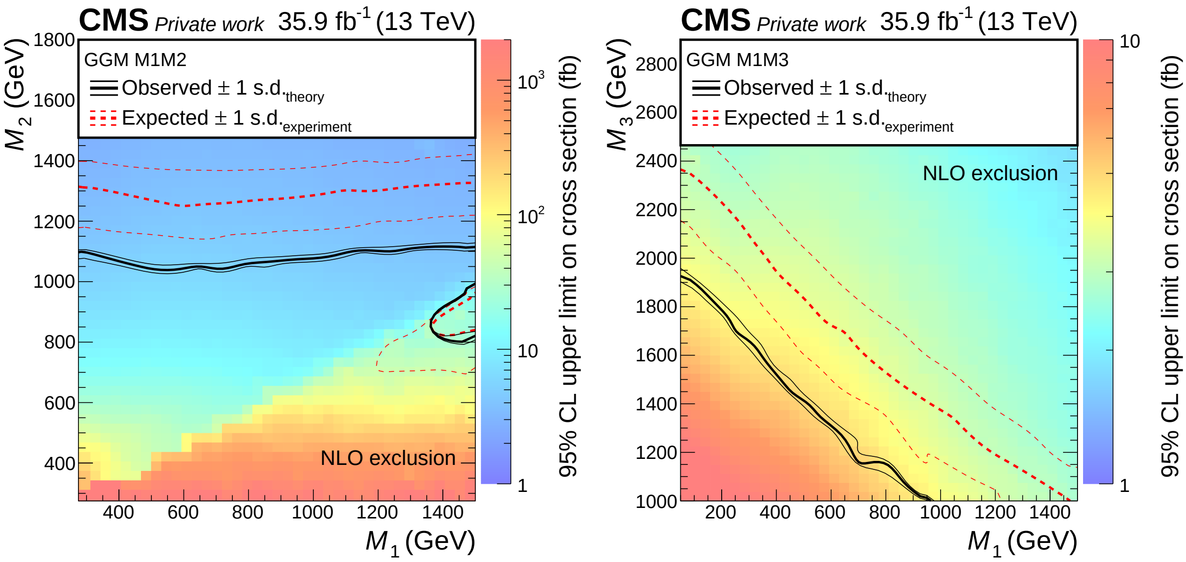

Figure 10.2: The 95% CL limits for the M1M2 (left) and M1M3 (right) scenarios. All masses spanning the phase spaces (bino mass M_1, wino mass M_2, and gluino mass M_3) are defined at the messenger scale of 10^{15} GeV. The colored histograms correspond to the observed upper cross section limit for each signal point. The thick lines in black and red show the observed and expected limits, respectively. The phase space below these lines is excluded by the combination. The thin lines indicate the uncertainty bands for both limits. For the observed limits, the theory uncertainties on the signal cross section are shown, while the expected limits are connected to the experimental uncertainties.

The features of the limit contours as well as the gain from the combination for the two GGM scenarios can be extracted from Fig. 10.3, where the area excluded by the expected limits of the combination and of the single analyses are shown. The results of the two inclusive searches, Photon+S_{T}^{γ} and Photon+H_{T}^{γ}, are summarized to improve the readability of the plot.

In case of the M1M2 scenario, the composition of the excluded area can be explained as follows. The green area denoted as "All" corresponds to the area, which is excluded by all four contributing analyses. The light green part of the phase space above this area, in contrast, is only ruled

out by the specific searches, while the small line below is covered by the inclusive searches and the Photon+Lepton search. In addition, areas, which are only excluded by one of the specific searches are found in the plot.
The low sensitivity of the Diphoton search as well as the two inclusive searches below the area, which is excluded by all searches, is caused by the smaller branching fraction of the neutralino[12] decaying to $\gamma\widetilde{\mathrm{G}}$ (cf. Sec. 6.2.2). This part of the phase space is mainly covered by the Photon+Lepton search, which benefits from the wino-like neutralino leading to additional charged leptons from the $\widetilde{\chi}_1^0 \rightarrow \mathrm{Z}+\widetilde{\mathrm{G}}$ decay. These features do not hold for signal points with a wino mass around 300 GeV. For these points the mass of the neutralino is too small for an on-shell Z to be produced and the decay to $\gamma\widetilde{\mathrm{G}}$ is again dominant.
In contrast to the sensitivity of the inclusive searches being limited by the nature of the neutralino decay below the area excluded by all searches, the restriction above this area is mainly caused by the signal cross section decreasing with an increasing wino mass combined with a smaller neutralino mass at low M_1 values. Since in the signal events $p_{\mathrm{T}}^{\mathrm{miss}}$ mainly originates from to the undetected gravitinos from neutralino decays, at low neutralino masses the high $p_{\mathrm{T}}^{\mathrm{miss}}$ requirements of the inclusive searches are not fulfilled by most of the signal events resulting in a reduced sensitivity.
The decreasing signal cross section is also the main reason for the limited sensitivity of the Photon+Lepton search for signal points at wino masses around 800 GeV as well as of the two specific analyses at high wino masses. At wino masses around 1200 GeV the separation between Photon+Lepton and Diphoton is caused by the different branching fractions of the neutralino decay. Here, the probability of pure diphoton final states decreases in favor of a higher probability of γZ final states with increasing bino masses.

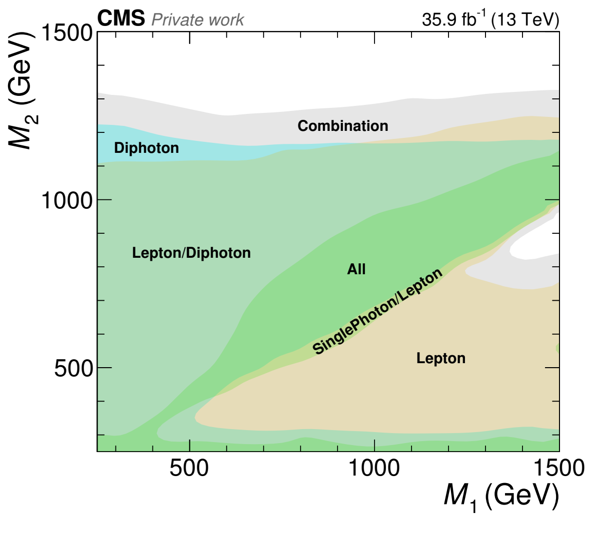

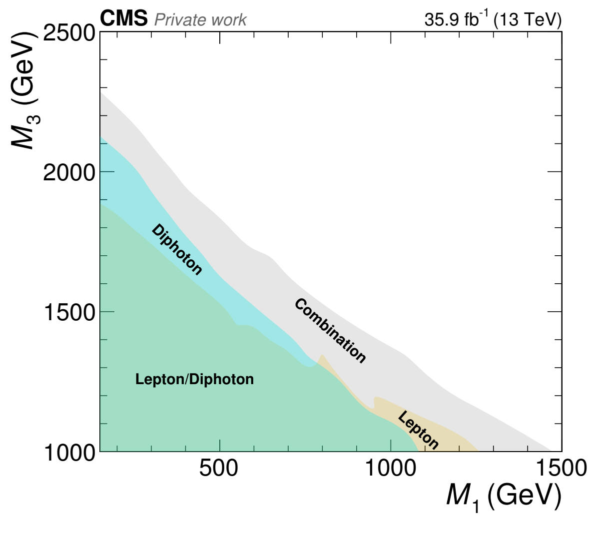

Figure 10.3: Excluded areas for the individual analyses and the combination based on the expected limit contours at 95% CL for the M1M2 (left) and M1M3 (right) scenario. The different areas are each labeled by the searches by which they can be excluded. The results of the Photon+S_{T}^{γ} and Photon+H_{T}^{γ} analyses are summarized and denoted as "SinglePhoton". The area marked as "All" is excluded by all analyses. The grey areas, labeled as "Combination" are only excluded by the combination and not by any of the individual searches. In the M1M3 scenario, no signal points excluded by the inclusive searches are found.

[12] Unless otherwise stated, "neutralino" denotes the lightest neutralino.

The main differences of the M1M3 scenario to the M1M2 scenario in the considered phase space correspond to the smaller signal cross sections and the bino-like nature of the neutralino (cf. Sec. 6.2.3 and 6.2.2). This results in a simpler structure regarding the excluded phase space of the M1M3 scenario. Since both inclusive searches do only feature a small sensitivity in this phase space, none of the signal points can be excluded by the Photon+S_{T}^{γ} or Photon+H_{T}^{γ} analyses alone. This is mainly caused by the comparably low signal cross sections across the whole phase space and the fact that the highest cross sections are found at low masses, which feature only small $p_{\mathrm{T}}^{\mathrm{miss}}$, as explained above. Although the two inclusive searches cannot exclude any points, they nevertheless contribute to the combination. The specific searches, in contrast, are able to exclude areas at lower masses both limited by the decreasing signal cross sections. The separation between both specific searches is again caused by the probability of pure diphoton final states decreasing in favor of γZ final states with increasing bino mass (cf. Sec. 6.2.2). An additional discussion of the most sensitive searches for each point in the phase space of both GGM scenarios can be found in Appx. 5.
The gain from the combination of the individual searches for both GGM scenarios with respect to the expected limit is shown as grey areas in both plots of Fig. 10.3. These parts of the phase space can only be excluded by the combination and not by any of the individual analyses. In case of the M1M2 scenario, two areas which are only covered by the combination are found. At high wino masses as well as at wino masses around 800 GeV, which are both limited by the decreasing signal cross sections, a gain of the order of 100 GeV for the expected limit on the wino masses can be achieved. For the M1M3 scenario, the expected limit on the gluino and wino masses can be increased by around 150 GeV and 200 GeV, respectively, by combining the four individual searches.

In order to discuss the discrepancy between the expected and observed limits found in the interpretation of both GGM scenarios as well as the gain achieved by the combination regarding sparticle masses, the limit contours are translated to the sparticle mass planes (cf. Fig. 10.4). In case of the M1M2 scenario, the area which features a small mass difference between the lightest neutralino and chargino (cf. Sec. 6.2.1) would lead to an inconsistent description of the mass diagonal. Thus, only signal points with a mass difference of at least 120 GeV are taken into account for the M1M2 scenario.
The discrepancies between the expected and observed limits are also found in both sparticle mass planes. These discrepancies originate from the individual limits of both specific searches, which drive the sensitivity at high chargino masses. Since both individual limits do already feature a weaker observed limit compared to the expected limit in the same regions of the phase space, the gap between expected and observed limits can only increase in the combination. The discrepancies can be explained by excesses found in multiple bins of both specific searches (cf. Fig. 10.1). For the second group of limit contours in the M1M2 scenario at wino masses of the order of 800 GeV, in contrast, no significant discrepancy is found (cf. Fig. 10.2). Here, a higher contribution from the Photon+S_{T}^{γ} search is present (cf. Appx. 5). Since in case of the Photon+S_{T}^{γ} analysis a good agreement between observation and background prediction is found, the expected and observed limit contours are in agreement in this area.
With the discrepancy between expected and observed limits assumed to be caused by excesses in some of the sensitive bins, there are multiple possible origins for these excesses. On the one hand, the excesses could be caused by an inaccurate standard model background prediction or statistical fluctuations in the corresponding search bins. On the other hand, there could be additional contributions to the observed yield from further processes, including physics beyond the standard model, which are not taken into account by the individual analyses. Since the signal region distributions used by the searches are not able to distinguish between these origins, this question cannot be finally answered by the combination either.

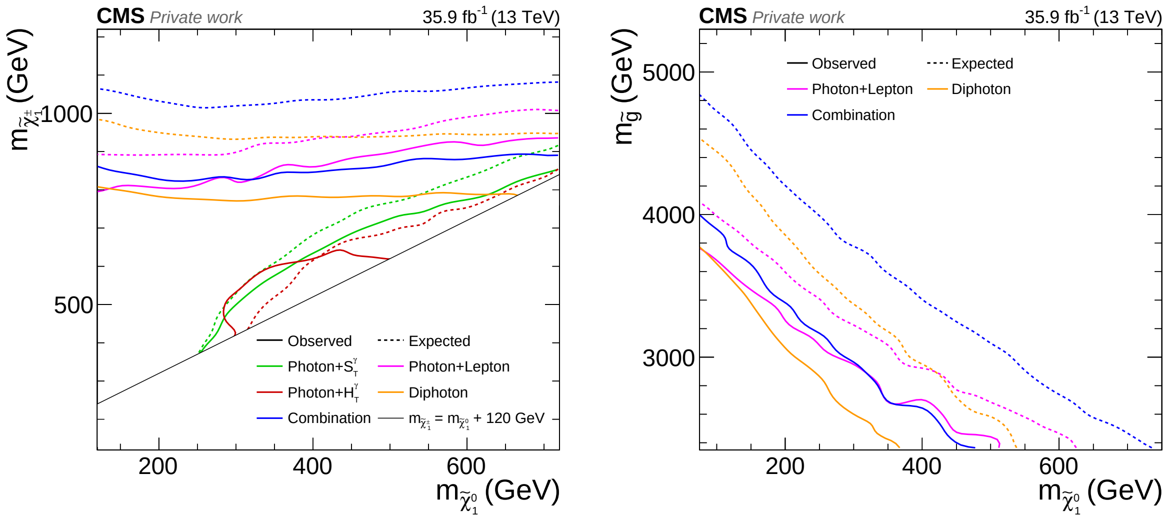

Figure 10.4: Exclusion contours at 95% CL of the individual searches and the combination for the sparticle mass planes of the M1M2 (left) and M1M3 (right) scenario. In case of the M1M2 scenario, the plane is spanned by the mass of the lightest neutralino and chargino, while only the phase space with a mass difference of at least 120 GeV is shown. The phase space of the M1M3 scenario is spanned by the mass of the lightest neutralino and the gluino mass.

The gain achieved by the combination regarding the expected limit on the wino mass in the M1M2 scenario, which is of the order of 100 GeV (cf. Fig. 10.3), can be translated to a gain of the same order on the expected limit of the chargino mass (cf. Fig. 10.4). In case of the observed limit, this gain can only be found at low neutralino masses, while at high neutralino masses the observed limit of the combination is slightly exceeded by the Photon+Lepton search. This feature is mainly caused by the excess in the Diphoton signal region, as discussed above. Thus, in case of the M1M2 scenario, the combination results in an observed (expected) limit on the chargino mass up to 850 (1050) GeV depending on the neutralino mass.
In case of the M1M3 scenario, the gain of 200 GeV in the bino mass corresponds to an increase of the upper expected limit on the neutralino mass of the order of 100 GeV. The gain of 150 GeV with respect to the gluino mass M_3, defined at the messenger scale, can be translated to an increase of the upper expected limit on the gluino mass at the EWK scale of the order of 250 GeV. For the observed limit, this gain is again only found at low neutralino masses. At higher neutralino masses, in contrast, the combination is slightly exceeded by the individual Photon+Lepton limit, similar to the M1M2 scenario. Thus, in case of the M1M3 scenario, the combination results in an observed (expected) upper limit on the neutralino mass of the order of 475 (650) GeV and on the gluino mass of the order of 4000 (4850) GeV. The latter limit has to be treated with caution since this limit is only valid in the M1M3 scenario and is derived indirectly from EWK production, while gluino pair production is not accessible.

10.3 Limits on Branching Fraction Scans

In addition to the interpretation based on the two GGM scenarios, exclusion limits for two scans based on simplified models are extracted from the results of the combination. Here, two different scans, which each feature a variable gaugino decay branching fraction (BF) as well as electroweak production, are used. The composition of these scans, namely the neutralino BF scan and the chargino BF scan, is discussed in Sec. 6.1.

The interpretation of the combination in both scans at 95% CL is shown in Fig. 10.5. In the neutralino BF scan, neutralino masses up to 1200 GeV at a BF of 100% to $\gamma\widetilde{\mathrm{G}}$ can be excluded by the expected limits, which extends to a BF of 5%. In case of the observed limit, this extension is only slightly smaller, while at a BF of 100% the upper neutralino mass limit drops to 1050 GeV. While this scan is based on the combined cross section for neutralino-chargino and chargino-chargino production, only the latter one is used for the chargino BF scan. Here, neutralino masses close to 1000 GeV can be excluded by the expected limit at a BF of 100% to $\widetilde{\chi}_1^0 + \mathrm{soft}$, with the neutralino further decaying to $\gamma\widetilde{\mathrm{G}}$. With respect to the chargino BF the expected limit extends to a value of 10%, while the observed limit only excludes points with a BF down to 18%. Similarly to the first scan, the upper neutralino mass is lowered in case of the observed limit, which excludes neutralino masses up to 825 GeV at a BF of 100%. As already seen in the interpretations based on the two GGM scenarios, in the results for the two branching fraction scans a discrepancy between the expected and observed limits, which is due to the same reasons as in the GGM scenarios, is found.

To discuss the performance of the individual analyses as well as the gain caused by the combination, the expected and observed limit for the combination and all four individual searches for both EWK branching fraction scans are shown in Fig. 10.6. Here, mainly the expected limits are studied since those are not affected by the excesses discussed before.
In case of the neutralino BF scan, the Photon+S_T^γ search covers a wide area of the phase space. Since only one photon is required by this search, good performance even at lower BFs

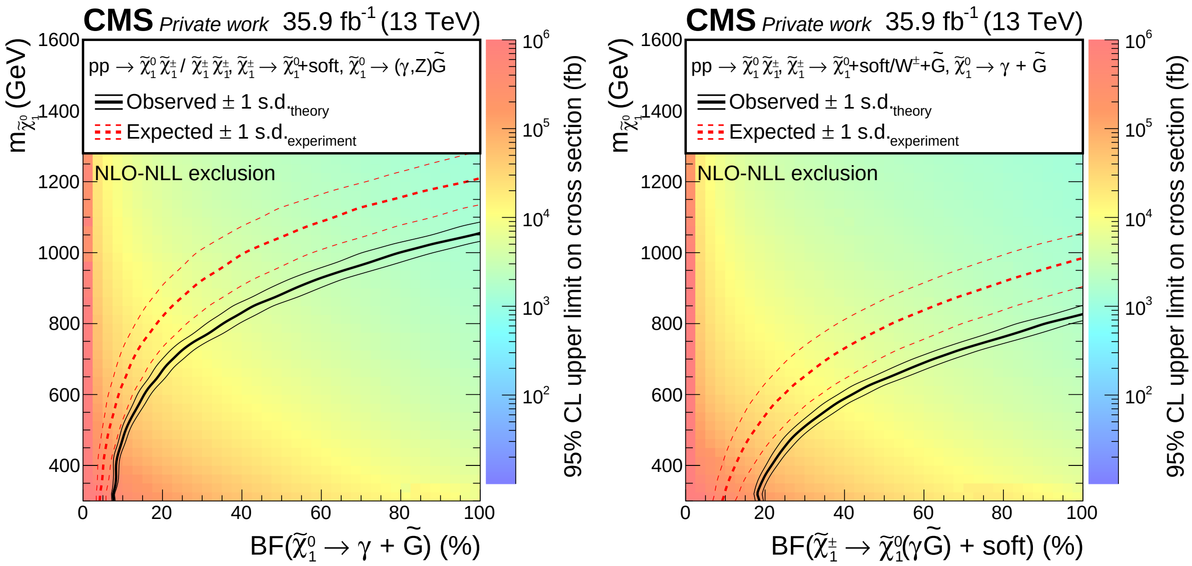

Figure 10.5: The 95% CL limits for two EWK scans with variable gaugino decay branching fractions. In the left scan, the decay of the lightest neutralino $\widetilde{\chi}_1^0$ is varied between $\gamma\widetilde{\mathrm{G}}$ and $\mathrm{Z}\widetilde{\mathrm{G}}$, while in the right scan the decay of the lightest chargino $\widetilde{\chi}_1^\pm$ varies between $\mathrm{W}^\pm\widetilde{\mathrm{G}}$ and $\widetilde{\chi}_1^0 + \mathrm{soft}$ with $\widetilde{\chi}_1^0$ further decaying to $\gamma\widetilde{\mathrm{G}}$. The y-axis in both plots is given by the mass of the lightest neutralino. The colored histograms correspond to the observed upper cross section limit for each signal point. The thick lines in black and red show the observed and expected limits, respectively. The phase space below these lines is excluded by the combination. The thin lines indicate the uncertainty bands for both limits. For the observed limits, the theory uncertainties on the signal cross section are shown, while the expected limits are connected to the experimental uncertainties.

is achieved. The Photon+H_T^γ search, in contrast, leads to a weaker exclusion contour across the whole BF range due to the additional requirement on H_T^γ. A slightly different dependency on the neutralino branching fraction can be found in case of the Diphoton analysis. Here, the expected limit almost reaches the one of the Photon+S_T^γ analysis at high BFs, while at lower BFs it falls below the Photon+H_T^γ search. The shape of this contour is caused by requiring at least two reconstructed photons. This requirement combined with the decreasing probability for diphoton events at lower BFs leads to a steeper drop of the expected limit of the Diphoton search. The lowest exclusion contour corresponds to the Photon+Lepton search, which requires an additional charged lepton. Since the only possibility for charged leptons to be produced in this scan is the neutralino decay to $Z\widetilde{G}$ with the Z decaying to e^+e^- or $\mu^+\mu^-$, only a few signal events at branching fractions significantly below 100% match this additional requirement. Thus, the Photon+Lepton search is expected to have no sensitivity at high BFs, where the $Z\widetilde{G}$ decay is suppressed. The reason why this feature is not reflected by the Photon+Lepton limit, which is almost constant towards higher branching fractions, is that in case of signal events with two photons, one of these photons can be falsely reconstructed as a charged lepton matching the requirements of the Photon+Lepton event selection.

In case of the chargino BF scan, the upper mass limits set by the four analyses (cf. Fig. 10.6) are reduced compared to the previously discussed scan, since only chargino-chargino production is taken into account. The shapes of the Photon+S_T^γ and Diphoton limits are quite similar compared to the neutralino BF scan. The main difference is given by the coincidence of these two expected limits at high branching fractions, while the Diphoton limit exceeds the Photon+S_T^γ limit at lower BFs. This difference compared to the neutralino BF scan is mainly a result of different requirements on the missing transverse momentum. Since this requirement is rather restrictive in the Photon+S_T^γ analysis, larger neutralino masses are preferred with respect to the sensitivity, while the lower requirement in the Diphoton analysis ensures a high sensitivity at lower neutralino masses. This behavior, which is similar to the one found in both GGM scenarios, is further visualized in Appx. 5. The expected limit contour of the Photon+Lepton search, in

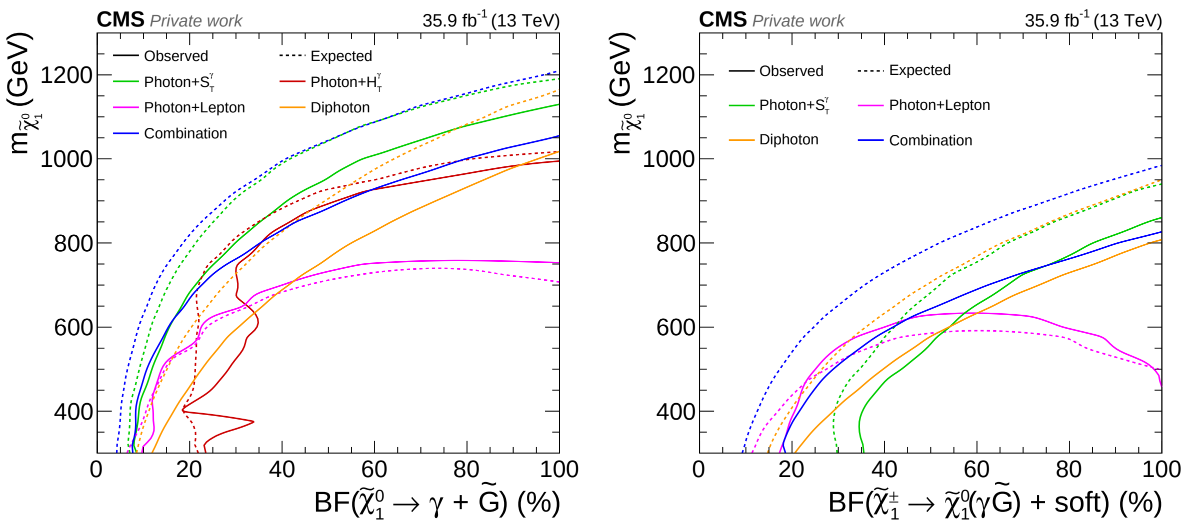

Figure 10.6: Exclusion contours at 95% CL of the individual searches and the combination for both EWK branching fraction scans. In the left scan, the decay of the lightest neutralino $\tilde{\chi}_1^0$ is varied between $\gamma\widetilde{G}$ and $Z\widetilde{G}$ while in the right scan the decay of the lightest chargino $\tilde{\chi}_1^\pm$ varies between $W^\pm\widetilde{G}$ and $\tilde{\chi}_1^0$ + soft with $\tilde{\chi}_1^0$ further decaying to $\gamma\widetilde{G}$. The y-axis in both plots is given by the mass of the lightest neutralino.

contrast, differs between the two EWK branching fraction scans. While in the previous scan charged leptons were produced following the neutralino decay to $\mathrm{Z}\widetilde{\mathrm{G}}$, here the chargino decay to $\mathrm{W}^{\pm}\widetilde{\mathrm{G}}$ can result in charged leptons. Thus, the Photon+Lepton limit shows a maximum at a BF around 50%, where the probability for a final state with one photon and one $\mathrm{W}^{\pm}$ boson is maximal, and even exceeds the other individual limits at low branching fractions. In case of the Photon+H_{T}^{γ} search, no limit contour is found for the chargino BF scan due to the reduced signal cross sections.

The sensitivity of the combination for both EWK BF scans is mainly driven by the Photon+S_{T}^{γ} and the Diphoton searches, with smaller contributions from the Photon+Lepton search in the chargino BF scan (cf. Fig 10.6). In case of the neutralino BF scan, only a small gain at low BFs with respect to the expected limit can be achieved by the combination. Due to the excess in the Diphoton signal region, this gain is not present in observed limits, where the highest limit is set by Photon+S_{T}^{γ} search. For the chargino BF scan, in contrast, the combination results in a gain on the upper neutralino mass limit up to 100 GeV across the whole BF range with respect to the expected limit. This gain originates from the coincidence of the Photon+S_{T}^{γ} and Diphoton limit contours in the chargino branching fraction scan, while in the neutralino BF scan such a coincidence is only present at the lowest BFs. The improvement of the observed limit by the combination is again strongly reduced by the excess in the Diphoton signal region and is only present at a BF between 50 and 70%, where a larger contribution from the Photon+Lepton search is found.

10.4 Limits on Gluino Pair Production

The last interpretation of the combination is performed on a simplified model, namely T5Wg, which features strong gluino pair production as well as fixed gaugino decay branching fractions (cf. Sec. 2.3.2 and 6.1). For this interpretation, the combination strategy is slightly changed such that the Diphoton search is not included in the combination. This change allows for the removal of the diphoton veto. The adaption of the combination strategy is motivated by studies of the performance of the expected limit based on the combination with and without contributions from the Diphoton search (cf. Appx. 6).

The interpretation of the combination at a 95% CL is shown in the left plot of Fig. 10.7, where the phase space is spanned by the gluino mass and the mass of the neutralino, which is degenerate with the chargino mass. Gluino masses up to 2100 GeV close to the mass diagonal and up to 1700 GeV at low neutralino masses can be excluded with respect to the expected limit. The observed limit only excludes gluino masses up to 1950 GeV near the mass diagonal while the upper mass limit decreases down to 1550 GeV at low neutralino masses. Similarly to the interpretations discussed before, the observed limit lies below the expected limit, but with respect to the corresponding uncertainties, a better agreement between the two contours is found.
There are two different reasons for the increased agreement between observed and expected limits in the T5Wg scenario compared to the previous interpretations. For the T5Wg scenario, the only production channel taken into account corresponds to strong gluino pair production. Since in case of strong SUSY scenarios the signal cross section uncertainty is significantly larger compared to EWK scenarios due to larger PDF uncertainties [73–81], the observed limit features broader uncertainty bands. In addition, the Diphoton signal region, which is the primary origin of the discrepancies between observed and expected limits in the GGM scenarios and BF scans, is not included for the T5Wg interpretation.

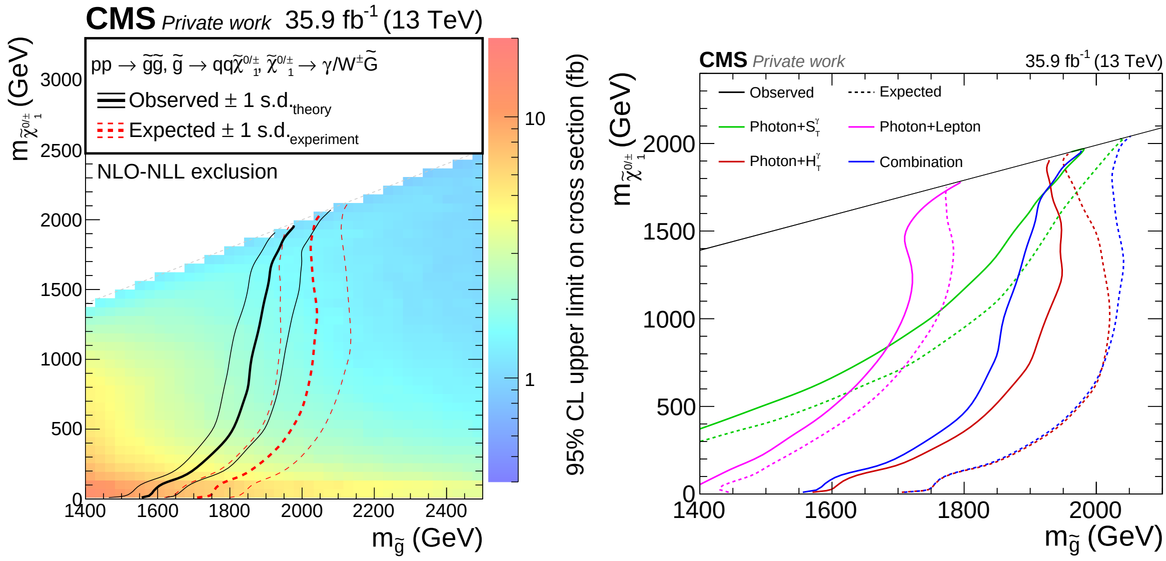

Figure 10.7: The 95% CL limits for the strong T5Wg scenario for the combination (left) and all individual searches as well as the combination (right). The phase space is spanned by the gluino mass and the mass of the neutralino. Left plot: The thick lines in black and red show the observed and expected limits, respectively. The phase space between these lines and the mass diagonal is excluded. The colored histogram corresponds to the observed upper cross section limit for each signal point. The thin lines indicate the uncertainty bands for both limits. For the observed limit, the theory uncertainties on the signal cross section are shown, while the expected limit is connected to the experimental uncertainties. Right plot: The observed (solid) and expected (dashed) limits for the individual searches and the combination are shown without uncertainties.

The contributions from the remaining three analyses to the combination in case of the T5Wg scenario are shown in the right plot of Fig. 10.7. Most parts of the phase space are dominated by the Photon+H_T^γ analysis, which is specially designed for strong SUSY scenarios. The only exception to this is found close to the mass diagonal, where the gluino and the neutralino masses are of the same order. For this part of the phase space only a small amount of hadronic activity is present in the signal events. Thus, the Photon+S_T^γ search, which has no requirements on the hadronic activity, has the strongest limit. For the Photon+Lepton analysis, in contrast, a lower sensitivity compared to the two inclusive searches across the whole phase space is found. Here, mainly the additional charged lepton requirement but also the lower requirement on the missing transverse momentum compared to the inclusive searches, which favors sensitivity to lower neutralino masses, decrease the sensitivity.

By combining the three analyses, a gain on the upper limit on the gluino mass of the order of 50 GeV at neutralino masses of 1700 GeV can be achieved with respect to the expected limit. Since, even with the Diphoton signal region removed from the combination, all three analyses feature a lower observed limit compared to the expected limit, this gain is not found in the observed limit of the combination. The observed limit of the combination is exceeded by the Photon+H_T^γ limit for most parts of the phase space, while it almost coincides with the Photon+S_T^γ limit close to the diagonal.

11 Summary and Outlook

For the first time in the CMS collaboration, multiple searches for gauge-mediated supersymmetry in events with photons have been combined. The data set used in this context was recorded by CMS in 2016 at a center-of-mass energy of 13 TeV and corresponds to an integrated luminosity of 35.9 fb^{-1}. For the combination, the results of two inclusive searches, Photon+S_{T}^{γ} and Photon+H_{T}^{γ}, and two more specific searches, Photon+Lepton and Diphoton, were combined. While all four searches are based on final states with at least one photon and a significant amount of missing transverse momentum, additional requirements used by the individual searches allowed for a high sensitivity of the combination across multiple SUSY scenarios.

To ensure a reliable combination of the searches, the overlap between the four signal regions was studied and removed by additional vetoes. These vetoes were applied based on an optimized combination strategy resulting in a good performance of the combination with respect to EWK as well as strong SUSY scenarios. In this optimized strategy, the two specific searches remained unchanged, while a lepton veto and a diphoton veto were applied to the event selection of the two inclusive searches. To remove the overlap between the inclusive searches, only the high-H_{T}^{γ} search bins of the Photon+H_{T}^{γ} were used, while a high-H_{T}^{γ} veto was applied to the Photon+S_{T}^{γ} event selection. Thus, a total of 49 exclusive search bins were available for the combination. To study possible changes in the background prediction caused by the additional vetoes, the background validations of the inclusive searches were repeated based on the modified event selections. Good agreement between background prediction and the observed data in the corresponding validation regions was found.
To account for possible correlations between background prediction uncertainties assigned by the individual analyses, the overlap between multiple control regions used in the prediction methods as well as similarities in the methods were studied. Several background prediction uncertainties were assumed to be fully correlated between the analyses. To ensure a consistent description of the signal prediction, which is based on identical signal simulations for all four searches, a set of signal uncertainties was defined and assumed to be fully correlated across all search bins.

For most of the 49 search bins used in the combination, good agreement between the background prediction and the observed data was found. Only three bins in the Photon+Lepton signal region and one bin each in the Photon+H_{T}^{γ} and Diphoton analyses showed an excess. These excesses were found to be features of the individual analyses instead of being caused by the additional vetoes applied in the combination.
The interpretation of the results was performed using several SUSY scenarios. In this context, two new GGM scenarios, which feature electroweak production of gaugino pairs, were produced along with the combination. This production as well as the mass spectra, sparticle decays, and signal cross sections of the two GGM scenarios were studied in detail to understand the resulting limit contours of the combination as well as the individual searches. The observed (expected) limit of the combination excludes chargino masses up to 850 (1050) GeV in the M1M2 scenario and neutralino masses up to 475 (650) GeV in the M1M3 scenario. The expected mass exclusions of the combination are about 100 GeV higher compared to the expected limits of the individual searches. Due to an excess in the Diphoton bin with the highest sensitivity only small improvements in case of the observed limit were achieved by the combination.
To study the results of the combination with respect to different branching fractions for neutralino and chargino decays, multiple EWK simplified models were merged and then used as additional interpretations. Here, a high sensitivity of the combination across a wide range of branching fractions, which exceeds the sensitivity of the individual searches in case of the expected limits, as well as good separation between the contributing searches were found. In addi-

tion to the EWK scenarios, the results of the combination were also interpreted with respect to gluino pair production. Here, the expected limit of the combination was found to coincide with the envelope of the two published expected limits of the Photon+S_{T}^{γ} and Photon+H_{T}^{γ} analyses and to exceed these two limits in a particular phase space region by about 50 GeV with respect to the gluino mass. This resulted in an upper gluino mass exclusion of 1950 (2100) GeV set by the observed (expected) limit of the combination.
Summarizing the different interpretations, the combination sets the first limits on the two new GGM scenarios as well as on the EWK branching fraction scans. The combination improves the expected upper mass limits across a wide phase space for these two types of scenarios as well as for the gluino pair production. In case of the observed limit, this improvement is reduced due to excesses found in the individual search bins. Nevertheless, the different interpretations motivate the general concept of combining individual analyses not only to cover larger phase spaces but also to improve exclusion limits.

Along with this thesis, a detailed description [97] of the combination was developed within a small team of the CMS collaboration and the analysis is planned to be published as a paper [98]. With the start of the second long shutdown of the LHC by the end of this year, the complete data set of Run 2 taken between 2016 and 2018 will become available. This will allow for a detailed analysis of the complete Run 2 data set, which exceeds an integrated luminosity of 140 fb^{-1} [99], during the upcoming shutdown, where no additional data is taken. Due to the increased data statistics available in this data set, the current exclusion limits could be further increased by a new iteration of the four individual analyses as well as the combination. A new iteration of combination would, in addition, also lead to a consistent result for searches for gauge-mediated supersymmetry in events with photons at CMS based on the complete Run 2 data set.

Appendix 1: CMS Data Sets

All four analyses contributing to the combination are based on the data recorded by CMS in 2016. This data was taken at a center-of-mass energy of 13 TeV and corresponds to an integrated luminosity of 35.9 fb^{-1} [11]. The composition of the data is shown in Tab. A1.1. The data is divided into different primary data sets (PD), which are based on trigger paths that require similar high-level objects. The two inclusive searches use the SinglePhoton PD, while the Diphoton search is based on the DoubleEG PD, which is also used by the Photon+Lepton search combined with the MuonEG PD. In addition to the separation into different PDs, the data is divided into exclusive run eras, which are denoted by capital letters.

Table A1.1: Paths for the data sets used by the four analyses. PD has to be replaced by the corresponding name of the primary data set. MINIAOD denotes the format of the data sets.

Data Sets
/PD/Run2016B-03Feb2017_ver2-v2/MINIAOD
/PD/Run2016C-03Feb2017-v1/MINIAOD
/PD/Run2016D-03Feb2017-v1/MINIAOD
/PD/Run2016E-03Feb2017-v1/MINIAOD
/PD/Run2016F-03Feb2017-v1/MINIAOD
/PD/Run2016G-03Feb2017-v1/MINIAOD
/PD/Run2016H-03Feb2017_ver2-v1/MINIAOD
/PD/Run2016H-03Feb2017_ver3-v1/MINIAOD

Appendix 2: Prospino Extension

To perform the cross section calculation following the PDF4LHC recommendations [87], an extension is implemented to the PROSPINO 2.1 framework [85]. This extension allows for the use of the LHAPDF file format [91], which is needed to follow the recommendations. To verify the extension the NLO cross section calculation for one arbitrary signal point of the M1M2 scenario is performed in two different ways using only one instead of 100 iterations. On the one hand, the build-in PDF class for CTEQ6.6 [100] is used, which result in the following PROSPINO output:

```
nn  1  5     0.0    0.0    1.0  374.7  374.8  0.000 0.865E-01 0.755E-03 0.102     0.645E-03 1.1745 0.920E-01 0.108
nn  1  7     0.0    0.0    1.0  374.7  374.8  0.000 0.386E-01 0.777E-03 0.455E-01 0.663E-03 1.1775 0.410E-01 0.483E-01
nn  5  7     0.0    0.0    1.0  374.8  374.8  0.000 0.603E-01 0.759E-03 0.725E-01 0.638E-03 1.2008 0.641E-01 0.770E-01

    i1 i2  dummy0 dummy1 scafac  m1    m2      angle LO[pb]   rel_error NLO[pb]   rel_error   K    LO_ms[pb] NLO_ms[pb]
```

On the other hand, the same PDF is used in the LHAPDF format via the implemented extension leading to the following output:

```
nn  1  5     0.0    0.0    1.0  374.7  374.8  0.000 0.865E-01 0.755E-03 0.102     0.645E-03 1.1745 0.920E-01 0.108
nn  1  7     0.0    0.0    1.0  374.7  374.8  0.000 0.386E-01 0.777E-03 0.455E-01 0.662E-03 1.1775 0.410E-01 0.483E-01
nn  5  7     0.0    0.0    1.0  374.8  374.8  0.000 0.604E-01 0.758E-03 0.725E-01 0.632E-03 1.2009 0.641E-01 0.770E-01

    i1 i2  dummy0 dummy1 scafac  m1    m2      angle LO[pb]   rel_error NLO[pb]   rel_error   K    LO_ms[pb] NLO_ms[pb]
```

Only the accessible production channels are taken into account. The results of the cross section calculation in LO and NLO can be seen in the last two columns of the output. Since these values are equal within both methods, the extension to the framework is validated and can be used for cross section calculation within the two GGM scenarios.

Appendix 3: Cross Section Uncertainties

The individual cross section uncertainties for both GGM scenarios can be seen in Fig. A3.1 and A3.2. The uncertainties are separated into contributions from PDF, α_s, and scale variations. The scale uncertainties are further divided into results from upward and downward shifting of the renormalization and factorization scales by a factor of two. For both scenarios, the cross section uncertainties are dominated by the PDF variations. Uncertainties up to 7.5% and 19% are found for the M1M2 and M1M3 scenarios, respectively. The only part of the phase space, where another uncertainty besides the PDF uncertainty is significantly contributing, is found at low M_2 values in the M1M2 scenario. Here, the uncertainty is dominated by the scale variations, which are of the order of 5%.

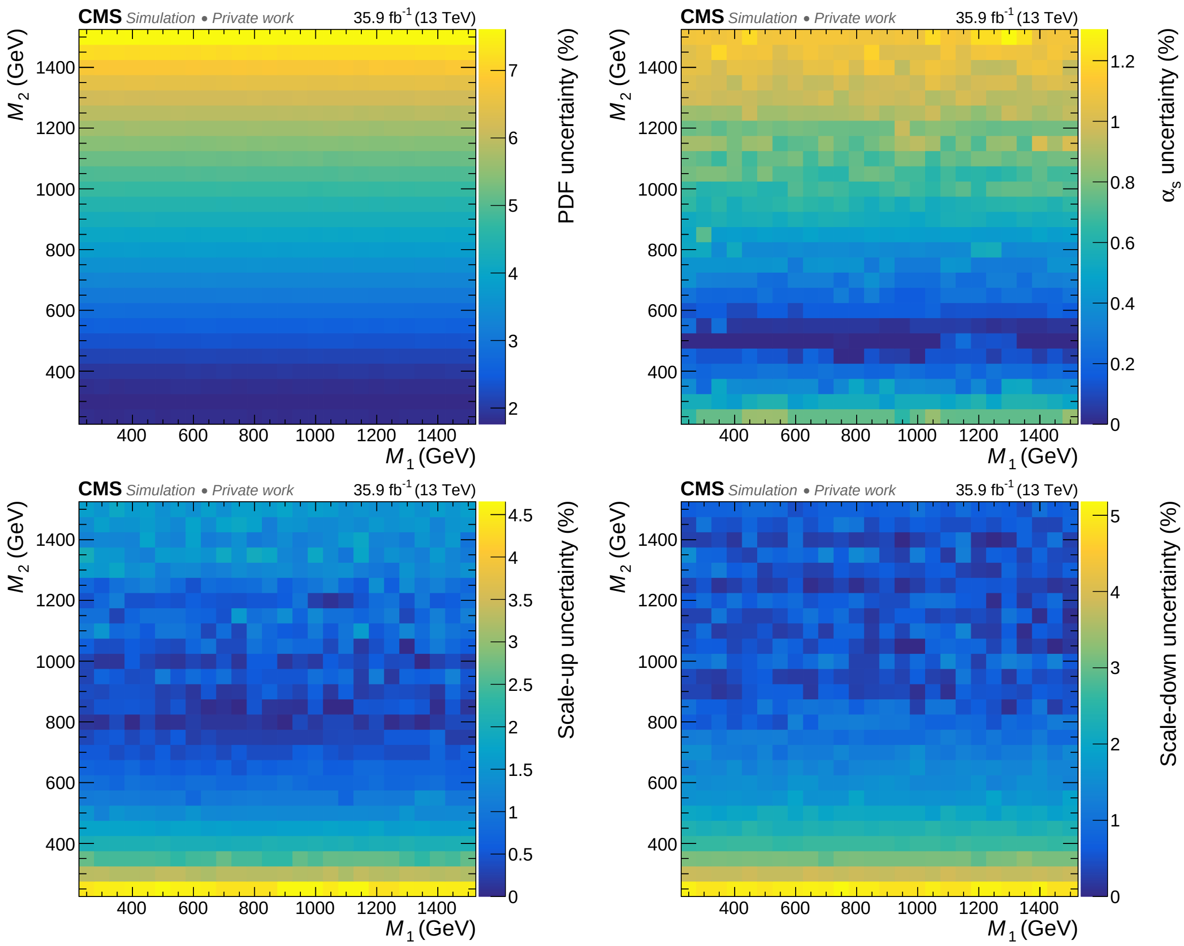

Figure A3.1: Individual cross section uncertainties for the M1M2 scenario divided into PDF uncertainty (upper left), α_s uncertainty (upper right), and scale-up (lower left) as well as scale-down uncertainty (lower right). In each of the four plots, the relative uncertainty is shown.

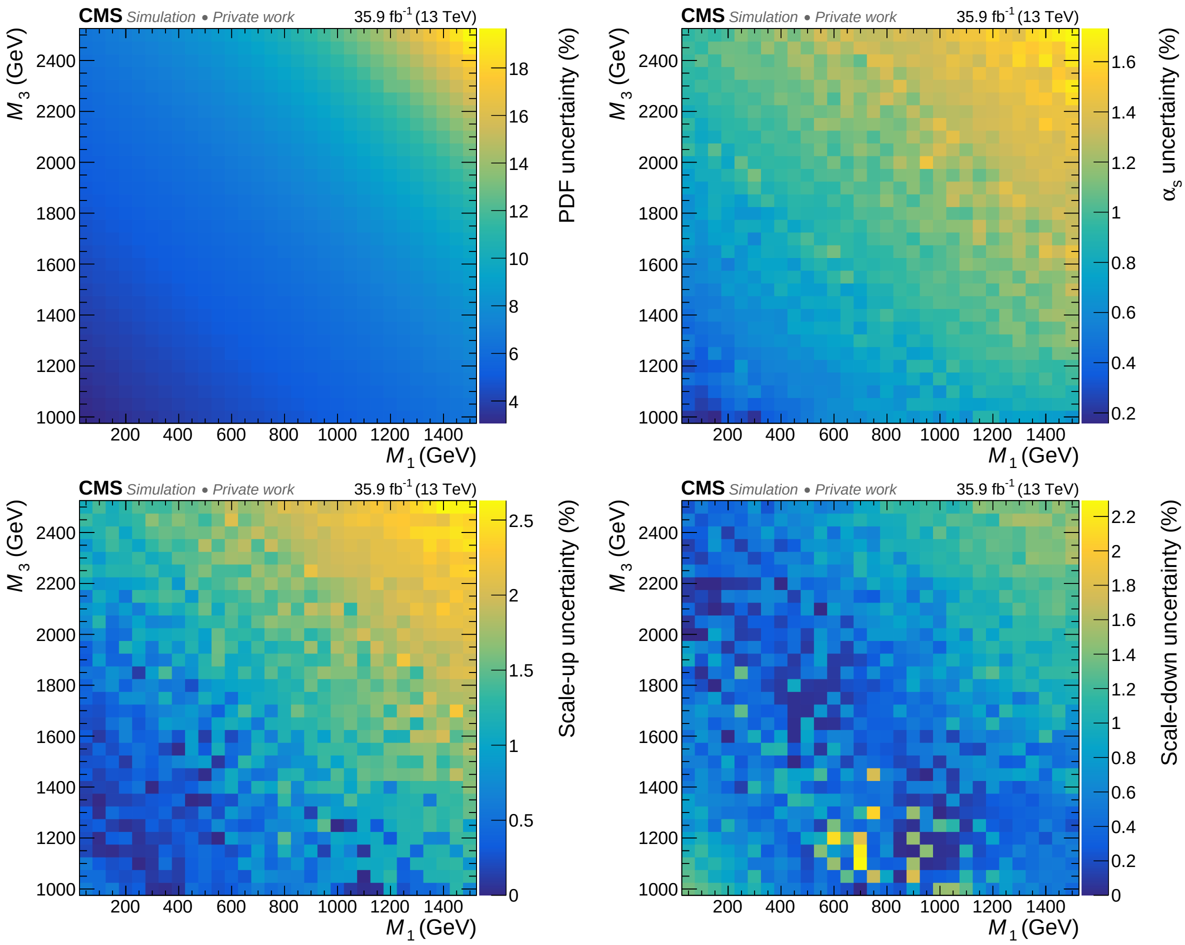

Figure A3.2: Individual cross section uncertainties for the M1M3 scenario divided into PDF uncertainty (upper left), α_s uncertainty (upper right), and scale-up (lower left) as well as scale-down uncertainty (lower right). In each of the four plots, the relative uncertainty is shown.

Appendix 4: Additional Background Validations

In the studies of the different combination strategies with respect to the performance of the expected limit[13], different vetoes are added to event selections of both inclusive searches. These vetoes change the composition of the signal regions and affect the background predictions as well. To ensure a reliable background prediction for both inclusive searches in each of the three combination strategies, the main background validations are performed with respect to the additional vetoes.

Strategy 1
The first strategy is designed to assign the overlap to the signal region of the Photon+S_{T}^{γ} analysis. Thus, this analysis remains unchanged while an S_{T}^{γ} veto is added to the selection of the Photon+H_{T}^{γ} search. The background validation based on this changed selection is shown in Fig. A4.1 for the low-H_{T}^{γ} and high-H_{T}^{γ} region. Both plots show good agreement between the observed data and the background prediction in the validation regions.

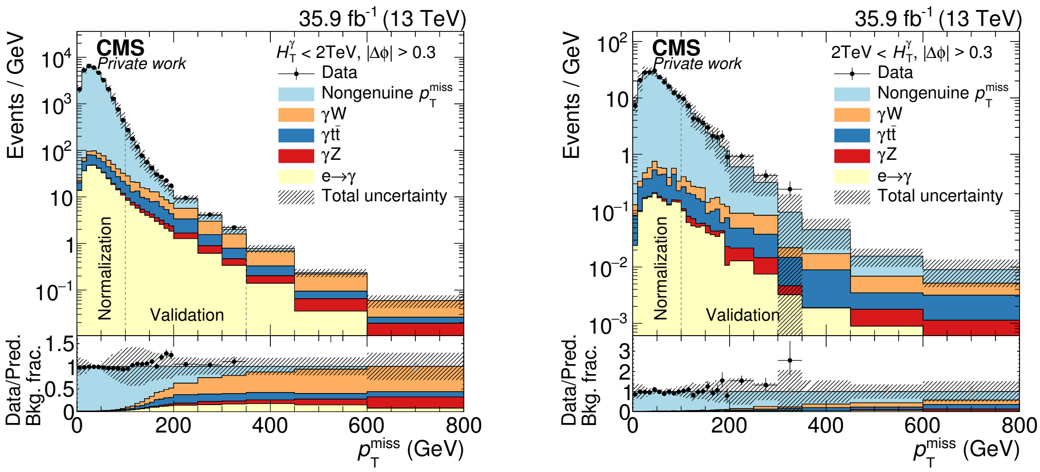

Figure A4.1: Background validation for the event selection of the Photon+H_{T}^{γ} analysis, with additional S_{T}^{γ} veto. The distribution of the missing transverse energy separated into normalization and validation region for the low-H_{T}^{γ} (left) and high-H_{T}^{γ} (right) region is shown. Since the validation of the background prediction is the primary goal, the data in the last three bins, which in both plots correspond to the signal region, is not shown.

Strategy 2
The second strategy is designed to assign the overlap to the signal region of the Photon+H_{T}^{γ} analysis. While this search remains unchanged, the additional full-H_{T}^{γ} veto is applied to the Photon+S_{T}^{γ} event selection. The corresponding background validation for this modified event selection is shown in Fig. A4.2. Good agreement between the observed data and the background prediction in the validation region is found.

[13] As mentioned in the discussion of these studies, the two specific searches are not included. Thus, the following background validations do not contain the lepton veto nor the diphoton veto. The background validations with respect to the final combination including these vetoes is discussed in Sec. 8.3.

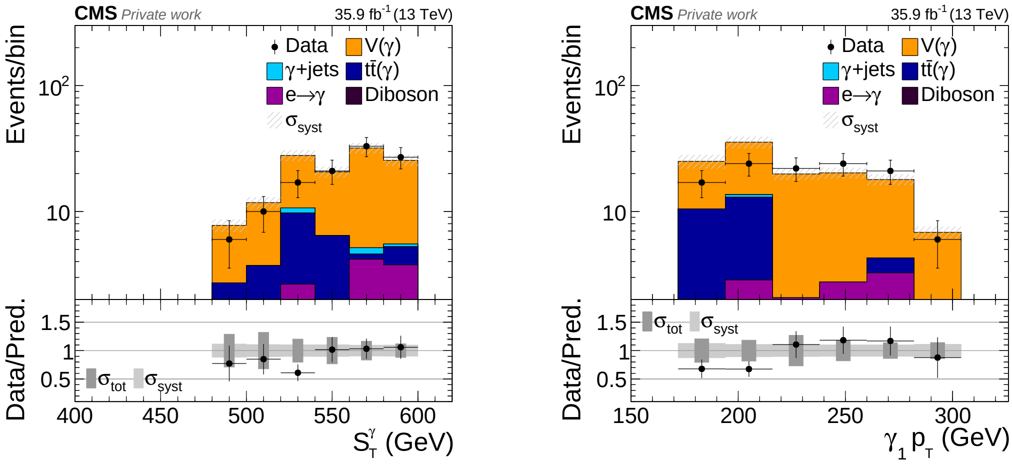

Figure A4.2: Validation of the background prediction in the validation region ($S_{\mathrm{T}}^{\gamma} < 600$ GeV) with the full-H_{T}^{γ} veto applied. The left plot corresponds to the S_{T}^{γ} spectrum while in the right plot the p_{T} distribution of the leading photon is shown. The systematic uncertainty on the background prediction (σ_{syst}) is shown in both parts of the plots while the total background uncertainty (σ_{tot}) can be seen in the ratio parts.

Strategy 3

The third strategy is designed to split the overlap between the two inclusive searches. In case of the Photon+H_{T}^{γ} search, only the three high-H_{T}^{γ} bins with $H_{\mathrm{T}}^{\gamma} > 2$ TeV are used in the combination, while an additional high-H_{T}^{γ} veto is added to the Photon+S_{T}^{γ} event selection. Thus, the background prediction of the Photon+H_{T}^{γ} analysis remains unchanged. The background validation for the Photon+S_{T}^{γ} search including the high-H_{T}^{γ} veto is shown in Fig. A4.3. Good agreement between the observed data and the background prediction in the validation region is found.

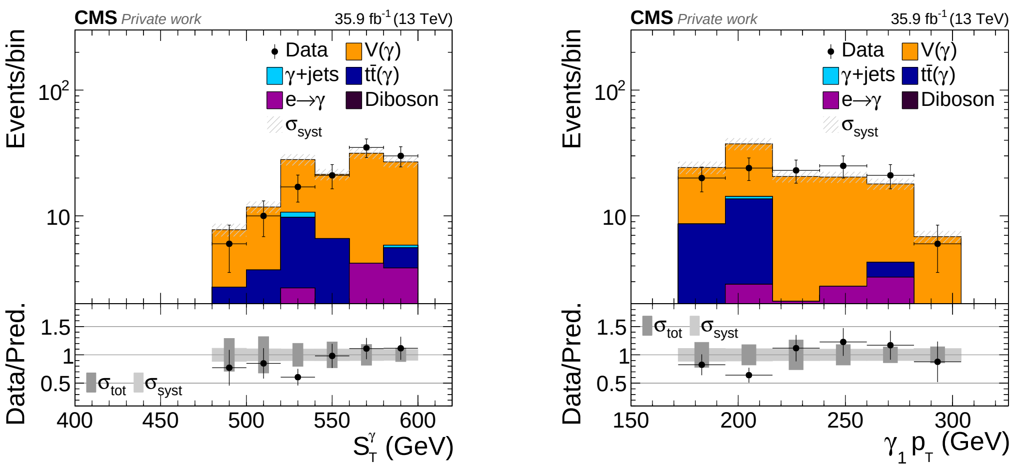

Figure A4.3: Validation of the background prediction in the validation region ($S_{\mathrm{T}}^{\gamma} < 600$ GeV) with the high-H_{T}^{γ} veto applied. The left plot corresponds to the S_{T}^{γ} spectrum while in the right plot the p_{T} distribution of the leading photon is shown. The systematic uncertainty on the background prediction (σ_{syst}) is shown in both parts of the plots while the total background uncertainty (σ_{tot}) can be seen in the ratio parts.

Appendix 5: Sensitivity Comparisons

For further studies on the sensitivity of the individual analyses, each signal point in the different scenarios is tested with respect to the most sensitive analysis. These studies are based on the expected limits, which are not affected by fluctuations in the data.

In case of both full GGM scenarios, the phase space is mainly dominated by the two specific searches (cf. Fig. A5.1). The lower sensitivity of both inclusive searches is caused by the lower neutralino masses, which cannot account for the high $p_{\mathrm{T}}^{\mathrm{miss}}$ requirements used in the event selections of the Photon+S_{T}^{γ} search and Photon+H_{T}^{γ} search. The only exception to this can be found at high M_1 values, which correspond to the largest neutralino masses. In these areas, the inclusive searches can achieve the highest sensitivity for a few signal points. This behavior is expected to continue if the phase space would be extended to higher bino masses. The remaining signal points are split between the Photon+Lepton and Diphoton searches. This splitting is mainly based on the different neutralino branching fractions to $\gamma\widetilde{\mathrm{G}}$ and $\mathrm{Z}\widetilde{\mathrm{G}}$ (cf. Sec. 6.2.2).

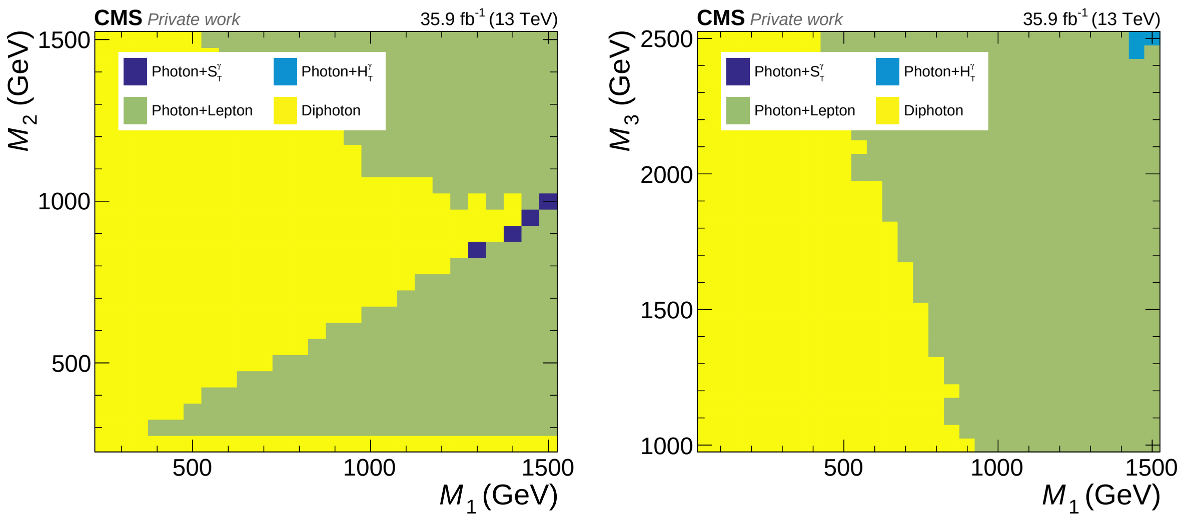

Figure A5.1: The analysis with the best expected exclusion limit for each signal point in the M1M2 (left) and M1M3 (right) GGM scenario.

In case of the two EWK scans, which feature a variable gaugino branching fraction, the composition of the phase space with respect to the most sensitive analysis changes (cf. Fig. A5.2). Due to the additional H_{T}^{γ} requirement in the event selection of the Photon+H_{T}^{γ} analysis no contributions from this analysis are found. The Photon+S_{T}^{γ} search, in contrast, mainly dominates the phase space at high neutralino masses, while the Diphoton search leads to the strongest expected limits at high branching fractions, which correspond to a high probability for final states with two photons. Significant contributions from the Photon+Lepton search can only be found in the chargino BF scan. Here, the area at low branching fractions, which correspond to a large probability for $\mathrm{W}^{\pm}$ bosons in the final state, is covered by the Photon+Lepton search. This does not hold in case of the neutralino BF scan. The only origin of charged leptons in this scan is given by the Z boson from the neutralino decay, which is enhanced at low BFs but features a lower branching fraction to charged leptons compared to the $\mathrm{W}^{\pm}$ boson. Here, only a few points at the smallest neutralino masses and smallest BFs are dominated by the Photon+Lepton search.

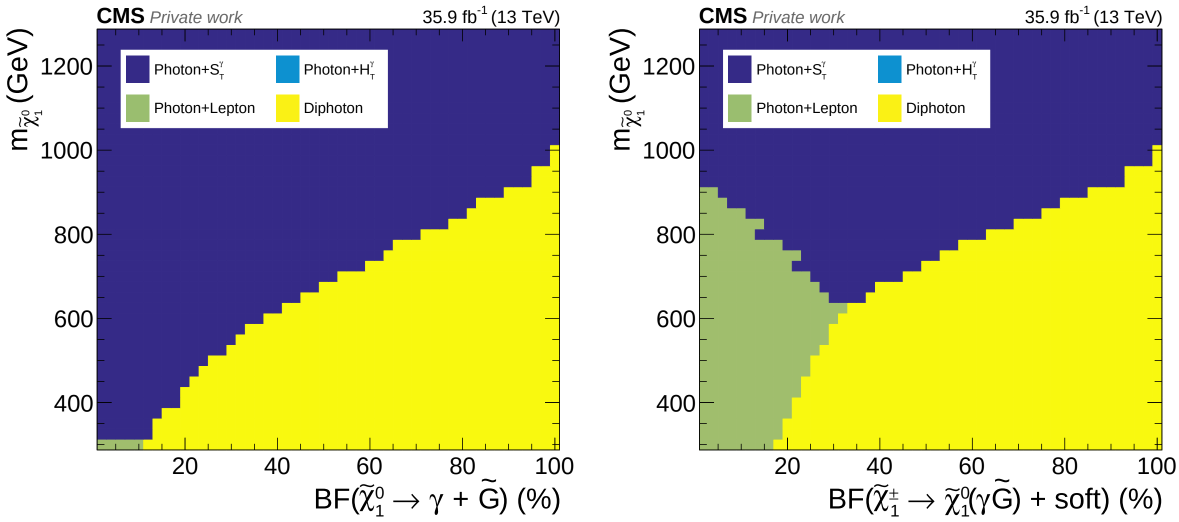

Figure A5.2: The analysis with the best expected exclusion limit for each signal point in the neutralino BF scan (left) and chargino BF scan (right).

In case of the strong gluino pair production, the phase space is dominated by the two inclusive searches (cf. Fig. A5.3). This is on the one hand caused by the larger neutralino masses compared to the scenarios discussed before, which typically results in a higher momentum of the undetected gravitino and thus to larger p_T^{miss} in the signal events. On the other hand, at lower neutralino masses, the neutralino can be highly boosted due to the large mass difference between gluino and neutralino also leading to large p_T^{miss} in the events. The separation between the two inclusive searches in this scenario is based on the H_T^γ requirement used in the event selection of the Photon+H_T^γ search. While close to the mass diagonal the quarks, which originate from the gluinos decaying to an EWK gaugino, can only have a small momentum, in the remaining parts of the phase space high momentum quarks can be produced leading to large H_T^γ in the signal events.

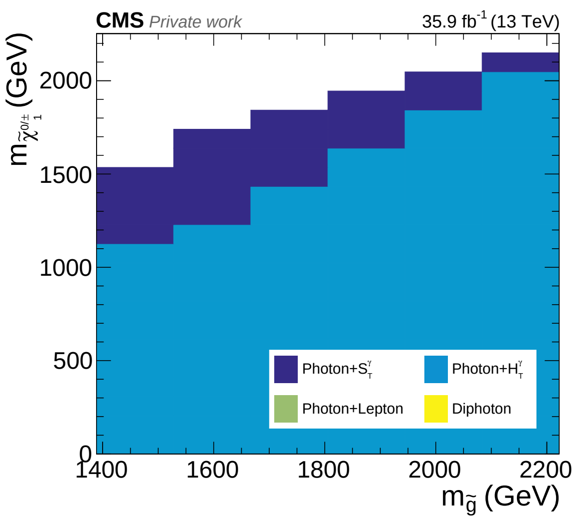

Figure A5.3: The analysis with the best expected exclusion limit for each signal point in the scenario, which features strong gluino pair production.

Appendix 6: Modified Combination Strategy

For the interpretation based on the scenario with strong gluino pair production, the combination strategy is slightly changed. This change is motivated by the performance of the expected limit calculated based on a combination with and without including the Diphoton analysis (cf. Fig. A6.1). Towards higher neutralino masses the combination without a Diphoton contribution exceeds the nominal combination by up to 30 GeV with respect to the expected upper limit on the gluino mass. This difference is caused by the additional diphoton veto, which is applied to the event selection of the inclusive searches in case of the nominal combination. While this veto only affects a total of two events in data (cf. Sec. 8.1), in case of the signal events a larger number of events can be affected and removed from the signal region of the inclusive searches. While this can be absorbed in case of the other scenarios due to the high sensitivity of the Diphoton analysis, this does not hold for the gluino pair production scenario (cf. Appx. 5). Thus, removing the Diphoton analysis from the combination results in an increased expected limit for this scenario.

This adaption of the combination strategy could lead to a slightly different background prediction in case of the two inclusive searches. Since only one data event in each of the two signal regions is affected by the Diphoton veto, the background prediction for the modified combination is expected to still be in line compared to the nominal combination.

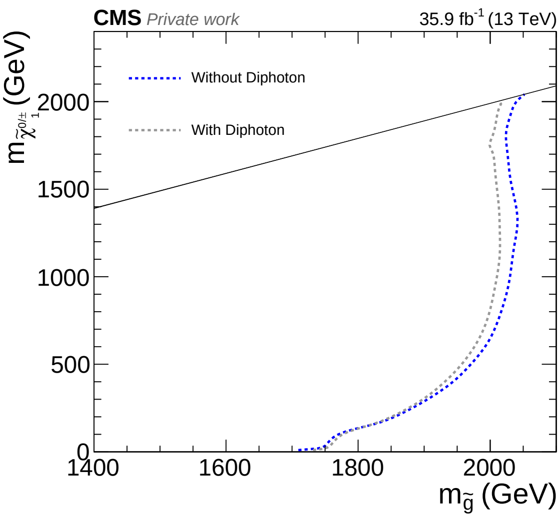

Figure A6.1: The 95% CL expected limits for the strong T5Wg scenario for the nominal combination (grey) and the modified combination, without contributions from the Diphoton analysis (blue). The phase space is spanned by the gluino mass and neutralino mass.

References

[1] J. J. Thomson, "XL. Cathode Rays", *The London, Edinburgh, and Dublin Philosophical Magazine and Journal of Science* **44** (1897), doi:10.1080/14786449708621070.

[2] E. Rutherford, "The scattering of alpha and beta particles by matter and the structure of the atom", *Phil. Mag. Ser.6* **21** (1911), doi:10.1080/14786440508637080.

[3] G. Pancheri and L. Bonolis, "The path to high-energy electron-positron colliders: from Wideroe's betatron to Touschek's AdA and to LEP", 2017. arXiv:1710.09003.

[4] W. Venus, "A LEP summary", *PoS* **HEP2001** (2001), doi:10.22323/1.007.0284.

[5] P. D. Grannis and M. J. Shochet, "The Tevatron Collider Physics Legacy", *Ann. Rev. Nucl. Part. Sci.* **63** (2013), doi:10.1146/annurev-nucl-102212-170621.

[6] G. Bertone, D. Hooper, and J. Silk, "Particle dark matter: Evidence, candidates and constraints", *Phys. Rept.* **405** (2005), doi:10.1016/j.physrep.2004.08.031, arXiv:hep-ph/0404175.

[7] S. P. Martin, "A Supersymmetry primer", *Adv. Ser. Direct. High Energy Phys. 21* (2010), doi:10.1142/9789814307505_0001, arXiv:hep-ph/9709356.

[8] L. Evans and P. Bryant, "LHC Machine", *JINST* **3** (2008), doi:10.1088/1748-0221/3/08/S08001.

[9] ATLAS Collaboration, "The ATLAS Experiment at the CERN Large Hadron Collider", *JINST* **3** (2008), doi:10.1088/1748-0221/3/08/S08003.

[10] CMS Collaboration, "The CMS experiment at the CERN LHC", *JINST* **3** (2008), doi:10.1088/1748-0221/3/08/S08004.

[11] CMS Collaboration, "Public CMS Data Quality Information". https://twiki.cern.ch/twiki/bin/view/CMSPublic/DataQuality#Dataset_For_Morion17_Conference. Accessed 27.08.2018.

[12] CMS Collaboration, "Search for gauge-mediated supersymmetry in events with at least one photon and missing transverse momentum in pp collisions at $\sqrt{s} = 13$ TeV", *Phys. Lett. B* **780** (2018), doi:10.1016/j.physletb.2018.02.045, arXiv:1711.08008.

[13] CMS Collaboration, "Search for supersymmetry in events with at least one photon, missing transverse momentum, and large transverse event activity in proton-proton collisions at $\sqrt{s} = 13$ TeV", *JHEP* **12** (2017), doi:10.1007/JHEP12(2017)142, arXiv:1707.06193.

[14] CMS Collaboration, "Search for supersymmetry using events with a photon, a lepton, and missing transverse momentum in pp collisions at $\sqrt{s} = 13$ TeV", CMS-PAS-SUS-17-012, CERN (2018).

[15] CMS Collaboration (2017). CMS-SUS-17-011, Paper to be published.

[16] CMS Collaboration, "Observation of a new boson at a mass of 125 GeV with the CMS experiment at the LHC", *Phys. Lett. B* **716** (2012), doi:10.1016/j.physletb.2012.08.021, arXiv:1207.7235.

[17] ATLAS Collaboration, "Observation of a new particle in the search for the Standard Model Higgs boson with the ATLAS detector at the LHC", *Phys. Lett. B* **716** (2012), doi:10.1016/j.physletb.2012.08.020, arXiv:1207.7214.

[18] W. Hollik, "Quantum field theory and the Standard Model", in *High-energy physics. Proceedings, 17th European School, ESHEP 2009, Bautzen, Germany.* arXiv:1012.3883.

[19] S. L. Glashow, "Partial Symmetries of Weak Interactions", *Nucl. Phys.* **22** (1961), doi:10.1016/0029-5582(61)90469-2.

[20] A. Salam and J. Ward, "Electromagnetic and weak interactions", *Physics Letters* **13** (1964), doi:10.1016/0031-9163(64)90711-5.

[21] S. Weinberg, "A Model of Leptons", *Phys. Rev. Lett.* **19** (1967), doi:10.1103/PhysRevLett.19.1264.

[22] H. Fritzsch and M. Gell-Mann, "Current algebra: Quarks and what else?", *eConf* **C720906V2** (1972), arXiv:hep-ph/0208010.

[23] Wikipedia contributors, "Standard Model — Wikipedia, The Free Encyclopedia". https://en.wikipedia.org/w/index.php?title=Standard_Model&oldid=853080396. Accessed 15.08.2018.

[24] P. W. Higgs, "Broken Symmetries and the Masses of Gauge Bosons", *Phys. Rev. Lett.* **13** (1964), doi:10.1103/PhysRevLett.13.508.

[25] UA1 Collaboration, "Experimental Observation of Isolated Large Transverse Energy Electrons with Associated Missing Energy at $\sqrt{s} = 540$ GeV", *Phys. Lett. B* **122** (1983), doi:10.1016/0370-2693(83)91177-2.

[26] UA2 Collaboration, "Observation of Single Isolated Electrons of High Transverse Momentum in Events with Missing Transverse Energy at the CERN anti-p p Collider", *Phys. Lett. B* **122** (1983), doi:10.1016/0370-2693(83)91605-2.

[27] UA1 Collaboration, "Experimental Observation of Lepton Pairs of Invariant Mass Around 95 GeV/c^2 at the CERN SPS Collider", *Phys. Lett. B* **126** (1983), doi:10.1016/0370-2693(83)90188-0.

[28] UA2 Collaboration, "Evidence for Z0 —> e+ e- at the CERN anti-p p Collider", *Phys. Lett. B* **129** (1983), doi:10.1016/0370-2693(83)90744-X.

[29] J. H. Christenson et al., "Observation of massive muon pairs in hadron collisions", *Phys. Rev. Lett.* **25** (1970), doi:10.1103/PhysRevLett.25.1523.

[30] LHCb Collaboration, "Observation of $J/\psi p$ Resonances Consistent with Pentaquark States in $\Lambda_b^0 \to J/\psi K^- p$ Decays", *Phys. Rev. Lett.* **115** (2015), doi:10.1103/PhysRevLett.115.072001, arXiv:1507.03414.

[31] R. Alkofer and J. Greensite, "Quark Confinement: The Hard Problem of Hadron Physics", *J. Phys. G* **34** (2007), arXiv:hep-ph/0610365.

[32] D0 Collaboration, "Search for high mass top quark production in $p\bar{p}$ collisions at $\sqrt{s} = 1.8$ TeV", *Phys. Rev. Lett.* **74** (1995), doi:10.1103/PhysRevLett.74.2422, arXiv:hep-ex/9411001.

[33] CDF Collaboration, "Observation of top quark production in $\bar{p}p$ collisions", *Phys. Rev. Lett.* **74** (1995), doi:10.1103/PhysRevLett.74.2626, arXiv:hep-ex/9503002.

[34] Particle Data Group Collaboration, "Review of Particle Physics", *Chin. Phys. C* **40** (2016), doi:10.1088/1674-1137/40/10/100001.

[35] G. F. Giudice and R. Rattazzi, "Theories with gauge mediated supersymmetry breaking", *Phys. Rept.* **322** (1999), doi:10.1016/S0370-1573(99)00042-3, arXiv:hep-ph/9801271.

[36] P. Meade, N. Seiberg, and D. Shih, "General Gauge Mediation", *Prog. Theor. Phys. Suppl.* **177** (2009), doi:10.1143/PTPS.177.143, arXiv:0801.3278.

[37] M. Buican, P. Meade, N. Seiberg, and D. Shih, "Exploring General Gauge Mediation", *JHEP* **03** (2009), doi:10.1088/1126-6708/2009/03/016, arXiv:0812.3668.

[38] S. Knapen, D. Redigolo, and D. Shih, "General Gauge Mediation at the Weak Scale", *JHEP* **03** (2016), doi:10.1007/JHEP03(2016)046, arXiv:1507.04364.

[39] S. Knapen and D. Redigolo, "Gauge mediation at the LHC: status and prospects", *JHEP* **01** (2017), doi:10.1007/JHEP01(2017)135, arXiv:1606.07501.

[40] J. Alwall, P. Schuster, and N. Toro, "Simplified Models for a First Characterization of New Physics at the LHC", *Phys. Rev. D* **79** (2009), doi:10.1103/PhysRevD.79.075020, arXiv:0810.3921.

[41] A. L. Read, "Modified frequentist analysis of search results (The CL(s) method)", in *Workshop on confidence limits, CERN, Geneva, Switzerland, 17-18 Jan 2000: Proceedings*.

[42] A. L. Read, "Presentation of search results: The CL(s) technique", *J. Phys. G* **28** (2002), doi:10.1088/0954-3899/28/10/313.

[43] The ATLAS, The CMS, and The LHC Higgs Combination Group Collaboration, "Procedure for the LHC Higgs boson search combination in Summer 2011", CMS-NOTE-2011-005. ATL-PHYS-PUB-2011-11, CERN (2011).

[44] J. Neyman and E. S. Pearson, "IX. On the problem of the most efficient tests of statistical hypotheses", *Philosophical Transactions of the Royal Society of London A: Mathematical, Physical and Engineering Sciences* **231** (1933), doi:10.1098/rsta.1933.0009.

[45] G. Cowan, K. Cranmer, E. Gross, and O. Vitells, "Asymptotic formulae for likelihood-based tests of new physics", *Eur. Phys. J. C* **71** (2011), doi:10.1140/epjc/s10052-011-1554-0, arXiv:1007.1727. [Erratum: Eur. Phys. J.C73,2501(2013)].

[46] S. Myers, "The LEP collider, from design to approval and commissioning", 1991. doi:10.5170/CERN-1991-008.

[47] LHCb Collaboration, "The LHCb Detector at the LHC", *JINST* **3** (2008), doi:10.1088/1748-0221/3/08/S08005.

[48] ALICE Collaboration, "The ALICE experiment at the CERN LHC", *JINST* **3** (2008), doi:10.1088/1748-0221/3/08/S08002.

[49] W. Herr and B. Muratori, "Concept of luminosity", doi:10.5170/CERN-2006-002.361.

[50] Wikipedia contributors, "Large Hadron Collider — Wikipedia, The Free Encyclopedia". https://en.wikipedia.org/w/index.php?title=Large_Hadron_Collider. Accessed 15.08.2018.

[51] CMS Document Database, "Interactive Slice of the CMS detector". https://cms-docdb.cern.ch/cgi-bin/PublicDocDB/RetrieveFile?docid=4172. Accessed 08.06.2016.

[52] V. D. Elvira, "Measurement of the Pion Energy Response and Resolution in the CMS HCAL Test Beam 2002 Experiment", CMS-NOTE-2004-020, CERN (2004).

[53] CMS Collaboration, "The CMS trigger system", *JINST* **12** (2017), doi:10.1088/1748-0221/12/01/P01020, arXiv:1609.02366.

[54] CMS Collaboration, "The CMS trigger in Run 2", *PoS* **EPS-HEP2017** (2017), doi:10.22323/1.314.0523.

[55] J. Alwall et al., "The automated computation of tree-level and next-to-leading order differential cross sections, and their matching to parton shower simulations", *JHEP* **07** (2014), doi:10.1007/JHEP07(2014)079, arXiv:1405.0301.

[56] J. Alwall et al., "Comparative study of various algorithms for the merging of parton showers and matrix elements in hadronic collisions", *Eur. Phys. J. C* **53** (2008), doi:10.1140/epjc/s10052-007-0490-5, arXiv:0706.2569.

[57] R. Frederix and S. Frixione, "Merging meets matching in MC@NLO", *JHEP* **12** (2012), doi:10.1007/JHEP12(2012)061, arXiv:1209.6215.

[58] P. Nason, "A New method for combining NLO QCD with shower Monte Carlo algorithms", *JHEP* **11** (2004), doi:10.1088/1126-6708/2004/11/040, arXiv:hep-ph/0409146.

[59] S. Frixione, P. Nason, and C. Oleari, "Matching NLO QCD computations with Parton Shower simulations: the POWHEG method", *JHEP* **11** (2007), doi:10.1088/1126-6708/2007/11/070, arXiv:0709.2092.

[60] S. Alioli, P. Nason, C. Oleari, and E. Re, "A general framework for implementing NLO calculations in shower Monte Carlo programs: the POWHEG BOX", *JHEP* **06** (2010), doi:10.1007/JHEP06(2010)043, arXiv:1002.2581.

[61] T. Melia, P. Nason, R. Rontsch, and G. Zanderighi, "WW, WZ and ZZ production in the POWHEG BOX", *JHEP* **11** (2011), doi:10.1007/JHEP11(2011)078, arXiv:1107.5051.

[62] P. Nason and G. Zanderighi, "W^+W^- , WZ and ZZ production in the POWHEG-BOX-V2", *Eur. Phys. J. C* **74** (2014), doi:10.1140/epjc/s10052-013-2702-5, arXiv:1311.1365.

[63] T. Sjostrand, S. Mrenna, and P. Z. Skands, "PYTHIA 6.4 Physics and Manual", *JHEP* **05** (2006), doi:10.1088/1126-6708/2006/05/026, arXiv:hep-ph/0603175.

[64] GEANT4 Collaboration, "GEANT4: A Simulation toolkit", *Nucl. Instrum. Meth. A* **506** (2003), doi:10.1016/S0168-9002(03)01368-8.

[65] CMS Collaboration, "Particle-flow reconstruction and global event description with the CMS detector", *JINST* **12** (2017), doi:10.1088/1748-0221/12/10/P10003, arXiv:1706.04965.

[66] W. Adam, R. Frühwirth, A. Strandlie, and T. Todorov, "Reconstruction of electrons with the Gaussian-sum filter in the CMS tracker at the LHC", *Journal of Physics G: Nuclear and Particle Physics* **31** (2005).

[67] CMS Collaboration, "Cut Based Photon ID for Run 2". `https://twiki.cern.ch/twiki/bin/view/CMS/CutBasedPhotonIdentificationRun2`. Accessed 27.08.2018.

[68] CMS Collaboration, "Cut Based Electron ID for Run 2". `https://twiki.cern.ch/twiki/bin/view/CMS/CutBasedElectronIdentificationRun2`. Accessed 27.08.2018.

[69] K. Rehermann and B. Tweedie, "Efficient Identification of Boosted Semileptonic Top Quarks at the LHC", *JHEP* **03** (2011), `doi:10.1007/JHEP03(2011)059`, `arXiv:1007.2221`.

[70] CMS Collaboration, "Baseline muon selections for Run-II". `https://twiki.cern.ch/twiki/bin/viewauth/CMS/SWGuideMuonIdRun2`. Accessed 27.08.2018.

[71] M. Cacciari, G. P. Salam, and G. Soyez, "The anti-k_t jet clustering algorithm", *JHEP* **04** (2008), `doi:10.1088/1126-6708/2008/04/063`, `arXiv:0802.1189`.

[72] R. Rahmat, R. Kroeger, and A. Giammanco, "The fast simulation of the CMS experiment", *J. Phys. Conf. Ser.* **396** (2012), `doi:10.1088/1742-6596/396/6/062016`.

[73] W. Beenakker, R. Hopker, M. Spira, and P. M. Zerwas, "Squark and gluino production at hadron colliders", *Nucl. Phys. B* **492** (1997), `doi:10.1016/S0550-3213(97)80027-2`, `arXiv:hep-ph/9610490`.

[74] A. Kulesza and L. Motyka, "Threshold resummation for squark-antisquark and gluino-pair production at the LHC", *Phys. Rev. Lett.* **102** (2009), `doi:10.1103/PhysRevLett.102.111802`, `arXiv:0807.2405`.

[75] A. Kulesza and L. Motyka, "Soft gluon resummation for the production of gluino-gluino and squark-antisquark pairs at the LHC", *Phys. Rev. D* **80** (2009), `doi:10.1103/PhysRevD.80.095004`, `arXiv:0905.4749`.

[76] W. Beenakker et al., "Soft-gluon resummation for squark and gluino hadroproduction", *JHEP* **12** (2009), `doi:10.1088/1126-6708/2009/12/041`, `arXiv:0909.4418`.

[77] W. Beenakker et al., "Squark and Gluino Hadroproduction", *Int. J. Mod. Phys. A* **26** (2011), `doi:10.1142/S0217751X11053560`, `arXiv:1105.1110`.

[78] C. Borschensky et al., "Squark and gluino production cross sections in pp collisions at $\sqrt{s} = 13$, 14, 33 and 100 TeV", *Eur. Phys. J. C* **74** (2014), `doi:10.1140/epjc/s10052-014-3174-y`, `arXiv:1407.5066`.

[79] W. Beenakker et al., "Production of Charginos, Neutralinos, and Sleptons at Hadron Colliders", *Phys. Rev. Lett.* **83** (1999), `doi:10.1103/PhysRevLett.83.3780`, `arXiv:hep-ph/9906298`.

[80] B. Fuks, M. Klasen, D. R. Lamprea, and M. Rothering, "Gaugino production in proton-proton collisions at a center-of-mass energy of 8 TeV", *JHEP* **10** (2012), `doi:10.1007/JHEP10(2012)081`, `arXiv:1207.2159`.

[81] B. Fuks, M. Klasen, D. R. Lamprea, and M. Rothering, "Precision predictions for electroweak superpartner production at hadron colliders with Resummino", *Eur. Phys. J. C* **73** (2013), doi:10.1140/epjc/s10052-013-2480-0, arXiv:1304.0790.

[82] A. Djouadi, M. M. Muhlleitner, and M. Spira, "Decays of supersymmetric particles: The Program SUSY-HIT (SUspect-SdecaY-Hdecay-InTerface)", *Acta Phys. Polon. B* **38** (2007), arXiv:hep-ph/0609292.

[83] M. Muhlleitner, A. Djouadi, and Y. Mambrini, "SDECAY: A Fortran code for the decays of the supersymmetric particles in the MSSM", *Comput. Phys. Commun.* **168** (2005), doi:10.1016/j.cpc.2005.01.012, arXiv:hep-ph/0311167.

[84] A. Djouadi, J. Kalinowski, and M. Spira, "HDECAY: A Program for Higgs boson decays in the standard model and its supersymmetric extension", *Comput. Phys. Commun.* **108** (1998), doi:10.1016/S0010-4655(97)00123-9, arXiv:hep-ph/9704448.

[85] W. Beenakker, R. Hopker, and M. Spira, "PROSPINO: A Program for the production of supersymmetric particles in next-to-leading order QCD", arXiv:hep-ph/9611232.

[86] W. Beenakker et al., "The Production of charginos / neutralinos and sleptons at hadron colliders", *Phys. Rev. Lett.* **83** (1999), doi:10.1103/PhysRevLett.100.029901, arXiv:hep-ph/9906298. [Erratum: Phys. Rev. Lett.100,029901(2008)].

[87] J. Butterworth et al., "PDF4LHC recommendations for LHC Run II", *J. Phys. G* **43** (2016), doi:10.1088/0954-3899/43/2/023001, arXiv:1510.03865.

[88] S. Dulat et al., "New parton distribution functions from a global analysis of quantum chromodynamics", *Phys. Rev. D* **93** (2016), doi:10.1103/PhysRevD.93.033006, arXiv:1506.07443.

[89] L. A. Harland-Lang, A. D. Martin, P. Motylinski, and R. S. Thorne, "Charm and beauty quark masses in the MMHT2014 global PDF analysis", *Eur. Phys. J. C* **76** (2016), doi:10.1140/epjc/s10052-015-3843-5, arXiv:1510.02332.

[90] R. D. Ball et al., "Impact of Heavy Quark Masses on Parton Distributions and LHC Phenomenology", *Nucl. Phys. B* **849** (2011), doi:10.1016/j.nuclphysb.2011.03.021, arXiv:1101.1300.

[91] A. Buckley et al., "LHAPDF6: parton density access in the LHC precision era", *Eur. Phys. J. C* **75** (2015), doi:10.1140/epjc/s10052-015-3318-8, arXiv:1412.7420.

[92] CMS Collaboration, "Measurement of the Inclusive W and Z Production Cross Sections in pp Collisions at $\sqrt{s} = 7$ TeV", *JHEP* **10** (2011), doi:10.1007/JHEP10(2011)132, arXiv:1107.4789.

[93] M. Sun and M. Paulini, "Search for supersymmetry using events with a photon plus lepton and missing transverse momentum in proton-proton collisions at $\sqrt{s} = 13$ TeV with the CMS detector". CERN-THESIS-2018-186, 2018.

[94] CMS Collaboration, "Search for top-squark pair production in the single-lepton final state in pp collisions at $\sqrt{s} = 8$ TeV", *Eur. Phys. J. C* **73** (2013), doi:10.1140/epjc/s10052-013-2677-2, arXiv:1308.1586.

[95] CMS Collaboration, "Jet energy scale and resolution in the CMS experiment in pp collisions at 8 TeV", *JINST* **12** (2017), doi:10.1088/1748-0221/12/02/P02014, arXiv:1607.03663.

[96] CMS Collaboration Collaboration, "CMS Luminosity Measurements for the 2016 Data Taking Period", CMS-PAS-LUM-17-001, CERN (2017).

[97] D. Meuser et al., "Combined search for supersymmetry with general gauge mediation in events with photons in pp collisions at 13 TeV", *CMS Analysis Note* (2017). CMS-AN-17-287, For CMS internal use only.

[98] CMS Collaboration (2017). CMS-SUS-18-005, Paper to be published.

[99] CMS Collaboration, "Public CMS Luminosity Information". `https://twiki.cern.ch/twiki/bin/view/CMSPublic/LumiPublicResults`. Accessed 16.10.2018.

[100] P. M. Nadolsky et al., "Implications of CTEQ global analysis for collider observables", *Phys. Rev. D* **78** (2008), `doi:10.1103/PhysRevD.78.013004`, `arXiv:0802.0007`.

Zentrales Prüfungsamt/Central Examination Office

RWTH AACHEN UNIVERSITY

Eidesstattliche Versicherung

Statutory Declaration in Lieu of an Oath

Meuser, Danilo

Name, Vorname/Last Name, First Name

331295

Matrikelnummer (freiwillige Angabe)
Matriculation No. (optional)

Ich versichere hiermit an Eides Statt, dass ich die ~~vorliegende Arbeit/Bachelorarbeit/~~ Masterarbeit* mit dem Titel
I hereby declare in lieu of an oath that I have completed the present paper/Bachelor thesis/Master thesis* entitled

Combination of Searches for gauge-mediated Supersymmetry in Events with Photons at CMS

selbstständig und ohne unzulässige fremde Hilfe (insbes. akademisches Ghostwriting) erbracht habe. Ich habe keine anderen als die angegebenen Quellen und Hilfsmittel benutzt. Für den Fall, dass die Arbeit zusätzlich auf einem Datenträger eingereicht wird, erkläre ich, dass die schriftliche und die elektronische Form vollständig übereinstimmen. Die Arbeit hat in gleicher oder ähnlicher Form noch keiner Prüfungsbehörde vorgelegen.
independently and without illegitimate assistance from third parties (such as academic ghostwriters). I have used no other than the specified sources and aids. In case that the thesis is additionally submitted in an electronic format, I declare that the written and electronic versions are fully identical. The thesis has not been submitted to any examination body in this, or similar, form.

Aachen, 28.10.2018

Ort, Datum/City, Date

Unterschrift/Signature

*Nichtzutreffendes bitte streichen

*Please delete as appropriate

Belehrung:
Official Notification:

§ 156 StGB: Falsche Versicherung an Eides Statt
Wer vor einer zur Abnahme einer Versicherung an Eides Statt zuständigen Behörde eine solche Versicherung falsch abgibt oder unter Berufung auf eine solche Versicherung falsch aussagt, wird mit Freiheitsstrafe bis zu drei Jahren oder mit Geldstrafe bestraft.
Para. 156 StGB (German Criminal Code): False Statutory Declarations
Whoever before a public authority competent to administer statutory declarations falsely makes such a declaration or falsely testifies while referring to such a declaration shall be liable to imprisonment not exceeding three years or a fine.
§ 161 StGB: Fahrlässiger Falscheid; fahrlässige falsche Versicherung an Eides Statt
(1) Wenn eine der in den §§ 154 bis 156 bezeichneten Handlungen aus Fahrlässigkeit begangen worden ist, so tritt Freiheitsstrafe bis zu einem Jahr oder Geldstrafe ein.
(2) Straflosigkeit tritt ein, wenn der Täter die falsche Angabe rechtzeitig berichtigt. Die Vorschriften des § 158 Abs. 2 und 3 gelten entsprechend.
Para. 161 StGB (German Criminal Code): False Statutory Declarations Due to Negligence
(1) If a person commits one of the offences listed in sections 154 through 156 negligently the penalty shall be imprisonment not exceeding one year or a fine.
(2) The offender shall be exempt from liability if he or she corrects their false testimony in time. The provisions of section 158 (2) and (3) shall apply accordingly.

Die vorstehende Belehrung habe ich zur Kenntnis genommen:
I have read and understood the above official notification:

Aachen, 28.10.2018

Ort, Datum/City, Date

Unterschrift/Signature